Alma Mater Studiorum – Università di Bologna

DOTTORATO DI RICERCA IN

INGEGNERIA CIVILE, CHIMICA, AMBIENTALE E DEI MATERIALI

Ciclo XXXIII

Settore Concorsuale: 03/B2 – FONDAMENTI CHIMICI DELLE TECNOLOGIE

Settore Scientifico Disciplinare: CHIM/07 – FONDAMENTI CHIMICI DELLE TECNOLOGIE

PREPARATION AND CHARACTERIZATION OF MULTIFUNCTIONAL BIO-BASED POLYMERS EXHIBITING ENHANCED PROPERTIES

Presentata da: Greta Giacobazzi

Coordinatore Dottorato

Prof. Luca Vittuari

Supervisore

Prof.ssa Annamaria Celli

Co-Supervisore

Dott. Claudio Gioia

Esame finale anno 2021

Abstract

Driven by environmental reasons and the expected depletion of crude oil, bio-based polymers are currently undergoing a renaissance in the attempt to replace fossil-based ones. The present work aims at contributing in the development of the steps that start from biomass and move to new polymeric multifunctional materials.

The study focuses on two bio-based building blocks (**itaconic and vanillic acids**) characterized by exploitable functionalities, i.e. a lateral double bond and a substituted aromatic ring respectively, able to confer interesting properties to the final polymers.

The lateral double bond of dimethyl itaconate was functionalized *via* thia-Michael addition reaction obtaining a **thermo-stable** building block that can undergo polycondensation under classical conditions of reaction. The addition of a long lateral chain allows the polymer to express **antimicrobial activity** against *Staphylococcus aureus* making it attractive for packaging and targeting antimicrobial applications. Moreover, the architecture of the homopolymer was modified by means of copolymerization with dimethyl 2,5-furandicarboxylate thus improving the **rigidity** and obtaining a thermo-processable material. Potential applications as thermoset or thermoplastic material have been discussed.

As concerns vanillic acid, the presence of aromatic rings on the polymer backbone imparts **high thermal stability**, but brittle behaviour in the homopolymer. Therefore, the architecture of the polyester was successfully tuned by means of copolymerization with a **flexible** bio-based comonomer, i.e. ω-pentadecalactone, providing processable random copolymers. An in depth investigation of water transport mechanism has been undertaken on the synthesized polyesters. Since the copolymers present a succession of aromatic and aliphatic units, as a consequence of the chemical structure **water vapor permeability** interposes between polyethylene and poly(ethylene terephthalate) proving that the copolyesters are suitable for packaging applications.

Moving towards a sustainable model of development, **novel sustainable synthetic pathways for the eco-design of new bio-based polymeric structures with high value functionalities and different potential applications** have been successfully developed.

Table of contents

CHAPTER 1: INTRODUCTION

1.1 Plastics and circular economy

The commonly used word "plastics" indicates an extremely large family of organic materials generally deriving from fossil sources. Plastics are defined as materials made up of pure organic polymers or blended with additives that can be easily moulded into different shapes and products for a large variety of uses. Invented only 110 years ago[1], synthetic plastics have replaced metals, ceramics and glass-made materials in many usages, becoming the most widely used man-made substances. Indeed, thanks to the availability of feedstock materials, easy processing, tuneable properties, lightness and low cost, plastic materials are used in a wide range of applications since decades: from clothing to agriculture application, from aerospace to medical and cosmetics uses.

Because of the continuous growth of human population and industrialization, worldwide plastic production is on the scale of million metric tons for year and its demand is increasing fast. Its production ramped up from 1.5 to 322 million tons since 1950 to 2015 (65 years).[2] In 2019 the global plastic production reached 368 Mt (Figure 1. 1).

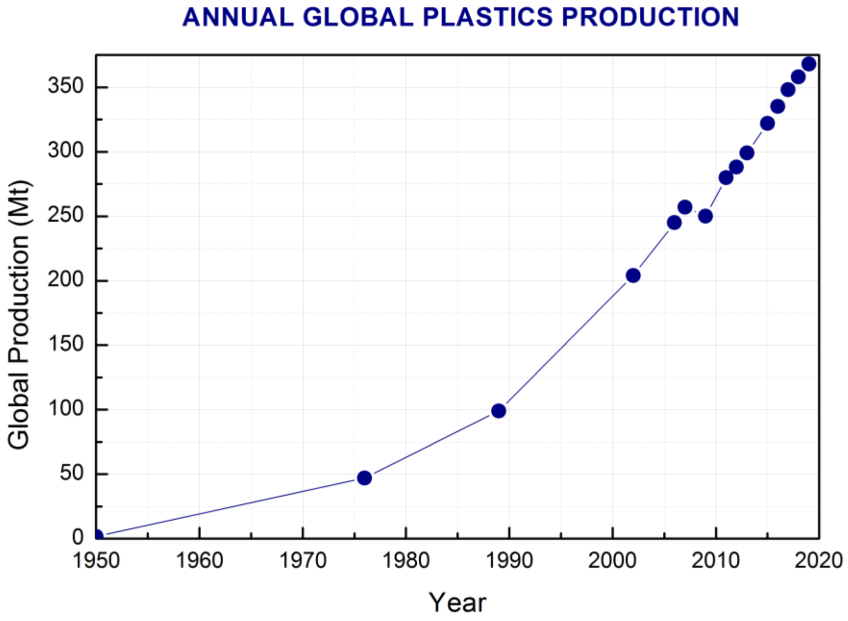

Figure 1. 1: Plastic worldwide production in million metric tons per year (Mt year^{-1}) from 1950 since nowadays. Data compiled from reference 2.

Such market demand increase results in intensive exploitation of fossil sources and in environmental pollution due to a mismanagement of plastics litter. The vast majority of plastic is not designed to be re-used during its life cycle since approximately half of plastic worldwide produced is used for single-use packaging application and other disposable (cups for beverage, food containers, cotton bud sticks, straws etc.).[3] This leads to a steady increase in plastic waste generation and the leakage of plastic waste into the environment given the fact that 40% of plastic waste is not accounted for in managed landfills and recycling facilities and consumers are not educated to do not disperse plastics in the environment.

In such a framework, industrial and academic research is committed daily to point out strategies tackling plastic waste accumulation into the environment, in particular into the marine environment.[4] Waste strategies taken in different regions in the word are similar and are based on the prevention and recycling of waste.

In response to the waste accumulation and mismanagement, the European Parliament and the Council have adopted a certain number of Directives to ensure that waste is recovered or disposed of without impairing the environment and human health. Indeed, in the context of a Circular Economy Action Plan laid down in the Communication of the European Commission of 2 December 2015 entitled '*Closing the loop – An EU action plan for the Circular Economy*' [5], and confirmed in its Communication of 16 January 2018 entitled '*A European Strategy for Plastics in a Circular Economy*' [3], the European Commission concluded that the steady increase in plastic waste generation must be tackled in order to achieve a circular life cycle for plastics.

The last directive (2019/904) of the European Parliament and of the Council of 5 June 2019 [6] reveals that the objective in the "*European Strategy for Plastics*" is to ensure that by 2030 all plastic packaging placed on the market is re-usable or easily recycled: *"The "European Strategy for Plastics" is a step towards establishing a circular economy in which the design and production of plastics and plastic products fully respect re-use, repair and recycling needs and in which more sustainable materials are developed and promoted."*

Therefore, management of plastics and plastic waste should include prevention of waste and, re-use, recycling and other forms of recovering plastics waste besides the development of more sustainable materials.[7]

Prevention means the reduction of the quantity of plastic and plastic waste at production process level and at marketing, distribution and utilization stages, by developing "clean" production and technologies.

Re-use means any operation by which plastic, after its life cycle, is refilled or used for the same purpose for which it was conceived, with or without the support of the auxiliary products enabling the plastic to be refilled.

Recovery includes operations that allow the use of plastic waste to generate value, e.g. use as a fuel to generate energy.

Recycling is defined as the reprocessing in a production process of the waste materials for the original purpose or for other purposes including organic recycling. There are several options for how this can be done: mechanical recycling, chemical recycling and organic recycling.[8] **Organic recycling** refers to biodegradability which is the natural-occurring breakdown process of a polymeric material by microorganism to carbon dioxide, water, mineral salts and new biomass in the presence of oxygen, or to carbon dioxide, methane, mineral salts and new biomass in the absence of oxygen.[9] Several biodegradable polymers have been identified such as poly(lactic acid) (PLA), polyhydroxyalkanoates (PHAs), poly(buthylene adipate-*co*-terephthalate) (PBAT), polycaprolactone (PCL) coming from fossil and natural sources.

In a sustainable model of development, biodegradable plastics are eco-friendly materials and together with bio-based plastics comprise bio-plastics.

1.2 Bioplastics and market data

Bioplastics comprise a whole family of materials environmentally friendly which are either bio-based, biodegradable or features both properties. The term ‘bio-based’ means that the plastic material or product is derived fully or partly from renewable feedstock referred as biomass. Biomass includes wood or forest residues, waste from food crops and food processing etc.[10] On the other hand, as stated in the previous paragraph, the term biodegradable means the property of a polymeric material to degrade under natural-occurring conditions.[9] The process of biodegradation depends on the surrounding environmental conditions (e.g. microorganism, location, temperature), and on polymer chemical and morphological structure (e.g. functional groups, molecular weight, crystallinity) and it is not related to the source basis of the material. Therefore, according to Figure 1. 2, a biopolymer can be bio-based and/or biodegradable. It’s worth nothing that bio-based polymers can be biodegradable such as poly(lactic acid) (PLA) and poly(buthylene succinate) (PBS), or non-biodegradable like bio-poly(ethylene terephthalate) (bio-PET). Moreover, not all biodegradable polymers are bio-based as for example poly(buthylene adipate-*co*-terephthalate) (PBAT) and polycaprolactone (PCL) which are indeed produced from crude oil.

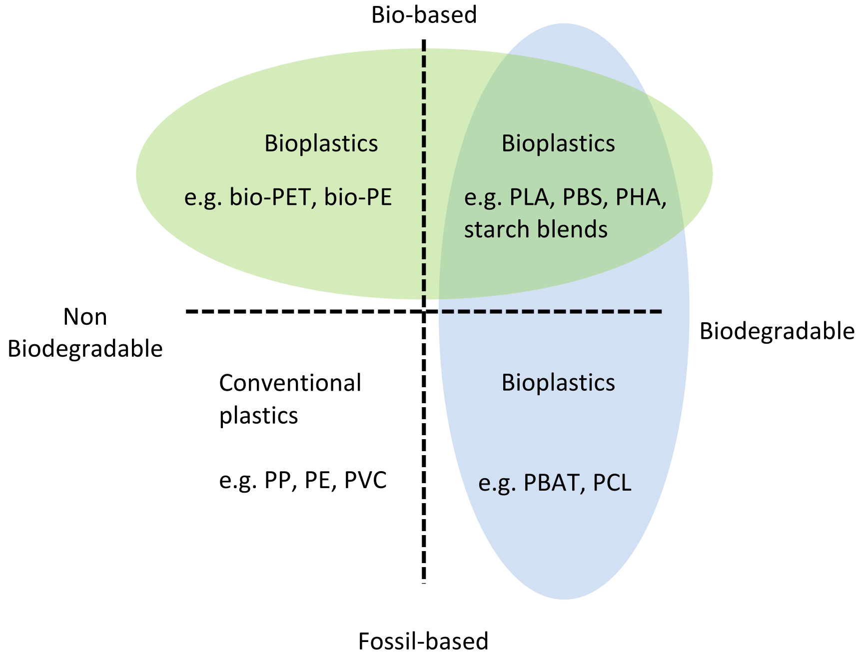

Figure 1. 2: Classification of bioplastics distinguishing bio-based and biodegradable plastics. Data compiled from reference 11.

Currently, mostly due to their high price level and low performances in comparison with conventional petrochemical counterparts, bioplastics production is negligible representing less than one percent of the about 370 Mt of plastics produced annually: 2.11 Mt in 2020. (Figure 1. 3).

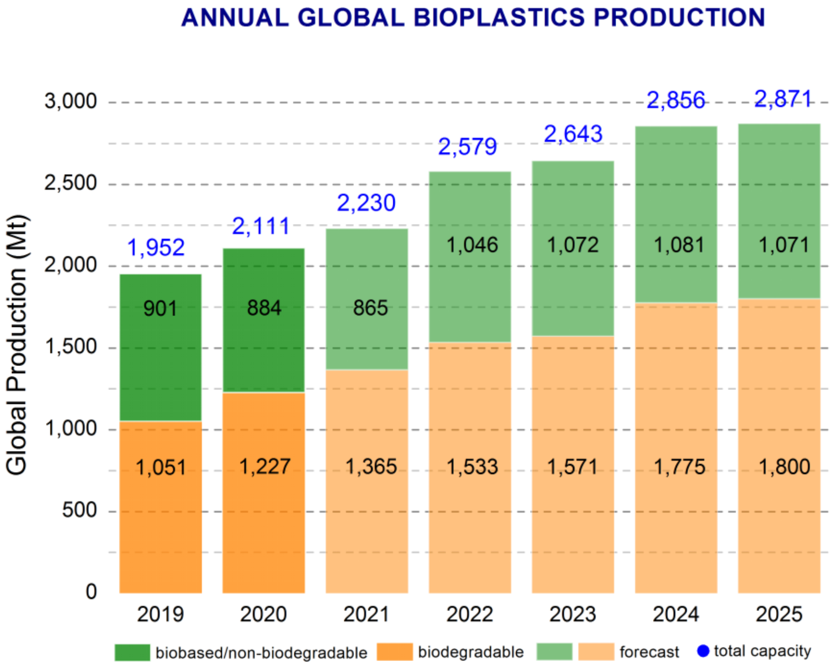

Figure 1. 3: Global production capacity of bioplastics. Data compiled from reference 11.

As shown in Figure 1. 4, biodegradable plastics production, both bio-based and fossil-based, accounts for over 58.1% (about 1.2 million tonnes) of the global bioplastic production and it is expected to increase to 1.8 million in 2025 (Figure 1. 3) especially due to PHA's significant growth rates.[11] The polyhydroxyalkanoates (PHAs) are a family of aliphatic polyesters, which are both biodegradable and bio-derived since they are accumulated as a carbon/energy source by bacteria.[12] Their production capacities are estimated to more than triple in the next five years.[11] Bio-based, non-biodegradable plastics, including for example bio-based polyethylene (bio-PE) and bio-based poly(ethylene terephthalate) (bio-PET), currently make up for over 41.9% of the global bioplastics production capacity. The production of bio-based PE and PP (polypropylene) is predicted to continue to grow due to the wide range of applications in which there are involved. On the other hand, intentions to increase production capacities for bio-based PET, however, have not been realised at the rate predicted in previous years. Instead, the focus has shifted to the development of poly(ethylene furandicarboxylate) (PEF), a new polymer that is expected to enter the market in 2023.[11] PEF is 100 % bio-based PET-like polymer.[13]

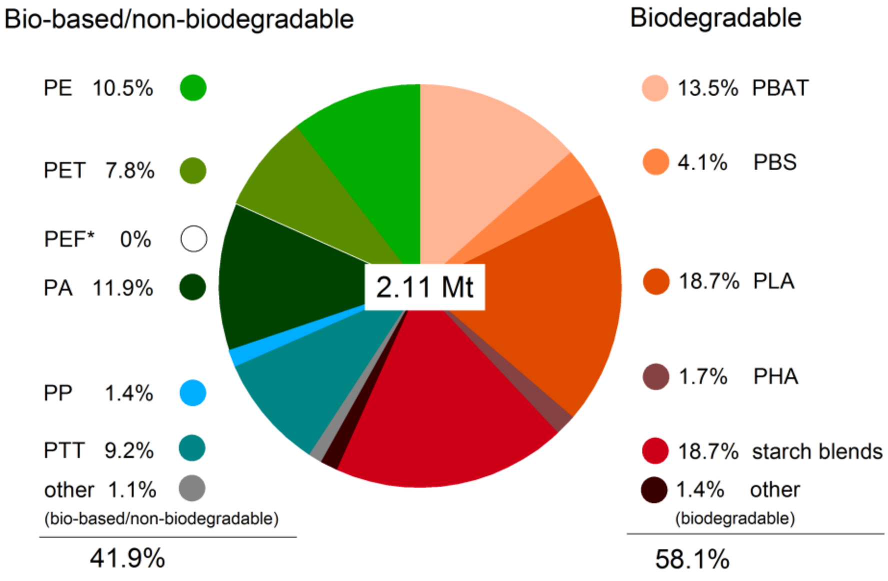

*PEF is currently in development and predicted to enter the maret in 2023

Figure 1. 4: Global production capacities of bioplastics in 2020 (by material). Data compiled from reference 11.

According to the latest market data and predictions compiled by European Bioplastics in cooperation with the research institute nova-Institute[14], global bioplastic production is set to increase from around 2.11 million tonnes in 2020 to approximately 2.87 million tonnes in 2025 (Figure 1. 3), driven by the interest in replace crude oil as feedstock and environmental reasons.

In this work, the terms bioplastic and biopolymers refers to materials from natural resource independently of the fact that they are biodegradable or not, unless noted otherwise.

1.3 Environmental advantages of bio-based plastics

Bio-based plastics established plastics emergence 160 years ago. Key mile-stones include the invention of cellulose nitrate (celluloid) in the 1860s, cellulose-hydrate films (cellophane) in 1912, casein protein (milk fibres) and soy-based plastics in the 1930s.[15,16] These materials lost their importance with the rise of the petrochemical industry in the 1950s which started to fabricate materials from crude oil. Nowadays, concerns over crude oil supply and climate change have been driving the renaissance of bio-based materials.[17]

The reasons of such trend are presented in the present paragraph.

Although exhaustion of fossil sources wasn't imminent, their exploitation at a rapid rate made known that it was inevitable as back as 1955.[18] At that time, few people paid attention to such issues but it's well established by now: fossil global reserves, created in millions of years from dead plants fossilized in anaerobic conditions, are exploited intensively and depletion is imminent given their long period of renewal. Worldwide, 98 million of barrels of crude oil are consumed daily (35 bb/year); at this rate, since the proven global crude oil reserves stand at ~ 1.5 trillion barrels, it can be estimated that total reserves will be depleted by 2060.[19,20] Since the world's reserves are predicted to deplete, crude oil price is recording record highs and in such a framework, it plays an occasional role as a political weapon. Moreover, a significant environmental damage occurs when extraction, transportation and processing of oil take place.

Concerning environmental issues, oil consumption is cause of CO_2 release in the atmosphere otherwise stored in fossil deposits. It leads to the greenhouse effect in which the gradually increasing concentrations of carbon dioxide (CO_2) methane (CH_4), and nitrous oxide (NO_2) are responsible to trap an excessive amount of solar radiation reflected from the earth causing in turn global warming.[18] Therefore, industrial and academic studies are focusing strong efforts to replace fossil sources with biomass for the production of chemicals and materials, referred as bio-based.

Biomass is a renewable, sustainable and environmentally benign source. Biomass resources include wood and wood wastes, agricultural crops and their waste by-products, municipal solid wastes, animal wastes, wastes from food processing and aquatic plants and algae. They can be divided into three general categories:

1. wastes including agricultural processing wastes, urban organic wastes, urban and mill wood wastes etc.;
2. standing forest e.g. trees and shrubs residues, sawdust from forest cleaning including also algae and water weed;
3. energy crops e.g. grasses, starch crops (corn, wheat, and barley), sugar crops (cane and beet), oilseed crops (soybean, sunflower).

To produce chemicals, biomasses can be subjected to fluid extraction, microorganism digestion, alcoholic fermentation and other biological processes.[21]

Replacing crude oil with biomass has environmental benefits. Indeed, if grown and utilized on a sustainable basis, biomass is carbon dioxide neutral. The sustainability is connected to the balance of carbon emission and removal associated to materials derived from biomass.

Plants fix carbon by converting carbon dioxide (CO_2) to organic compounds *via* photosynthesis. Each year, terrestrial plants fix 175×10^9 tons of CO_2 (about 20 tons per person).[22] Carbohydrate, represented by the building block CH_2O, is the primary organic compound. Over millions of year ($>10^6$ years), dead plants fossilized in anaerobic conditions forming crude oil. Crude oil is therefore a store of carbon underground. When oil is transformed in petrochemical products, stored carbon is released in the atmosphere in a short time (1-10 years) making a net contribution to greenhouse gases. There’s an imbalance between the rate of CO_2 conversion to oil and CO_2 release.

Considering biomass as a source of chemicals and materials, CO_2 is taken up by new plants growth at the same rate that it is released by using the harvested biomass (1-10 years). Therefore the substitution of crude oil with biomass will result in a net reduction in greenhouse gas emission and the replacement of a non-renewable source.[18]

Despite several environmental advantages, there are also some constraints regarding the use of biomasses. There is a concern that a widespread use of natural forest causes deforestation and localized fuelwood scarcity. However, it is widely accepted that deforestation is mainly caused by conversion of forestland into urban areas and agricultural lands. In addition, there is a potential conflict over the use of agricultural land and water resource for biomass production rather than food supply. In view of such considerations, biomass processes need to maximize wastes exploitation to preserve standing forests and agricultural lands but at the same time valorise huge amounts of agricultural and wood wastes as well as urban organic wastes.[23] Moreover, some biomass applications are not fully economically competitive at this stage. Fuel-based applications are high efficient and optimized whereas biomass processes need improvements. However the economics of biomass applications are improving and industrial and academic research is working to optimize biomass processes by giving them a competitive edge.[21]

It's worth noting that biomass can be exploited for chemicals and materials production as well as energy. Indeed, biomass is one of the possible renewable sources along with solar, wind, hydroelectric, and geothermal powers able to replace fossil fuels in energy production and its conversion may be conducted through direct combustion process, thermochemical processes as well fermentation processes.[21]

In this work, biomasses are considered as sources for chemicals and materials.

1.4 Bio-based polymers: definition and classification

Bio-based polymers can be classified in three different categories:

1. natural polymers;
2. polymers obtained through biomass fermentation by microorganisms;
3. polymers obtained through synthetic polymerization of monomers from biomass.

1.4.1 Natural polymers

Natural polymers mean naturally occurring polymers that can be separate from biomass. They have plant origin such as cellulose, hemicellulose, starch, lignin or animal origin as chitin and chitosan.

Cellulose is the most abundant polymer on earth and it is an essential structural component of the primary cell wall of plants and algae. It is classified as polysaccharide with the formula $(C_6H_{10}O_5)_n$ consisting of a linear chain of repeating β-D-glucose units. The D-glucose units are covalently linked through acetal functions between the equatorial OH groups of C1 and C4 carbon atoms (β-1, 4) as shown in Figure 1. 5.

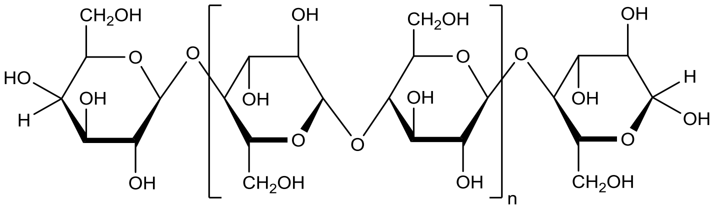

Figure 1. 5: Cellulose chemical structure: linear chain of repeating β-D-glucose units.

The multiple hydroxyl groups form intramolecular hydrogen bonds, holding the linear chains firmly together and forming ordered microfibrils leading to a highly crystalline material.[24] For a perfect crystal of cellulose, the theoretically predicted elastic modulus and tensile strength is 150 and 10 GPa respectively [25], which are comparable to Kevlar fibers.

Cellulosic materials have several advantages. Cellulose is an abundant, inexpensive and biodegradable resource. Moreover, it has high strength-to-weight ratio (low density, high specific strength and modulus) and a relatively reactive surface, which can be used for surface modification. Therefore, cellulosic materials cover several applications: from textile to building, from packaging to pharmaceutical. Some interest is growing in the field of cellulose-reinforced thermoplastics in which highly crystalline cellulose fibres improve composite material stiffness. As well, nanocomposites based on cellulose nanocrystals are currently investigated.[26]

Starch is another vegetal polymer produced by green plants as energy storage. It is a polysaccharide consisting of repeating D-glucose units. Depending on the linkage, glucose units form two macromolecular structures which characterize starch. These are: the linear amylose structure consisting of α-1,4-linked D-glucose units and the branched amylopectin structure consisting in a sequence of α-(1,4)-D-glucose units branched every 24 to 30 units *via* a glicosidic α-(1,6) bond. (Figure 1. 6)

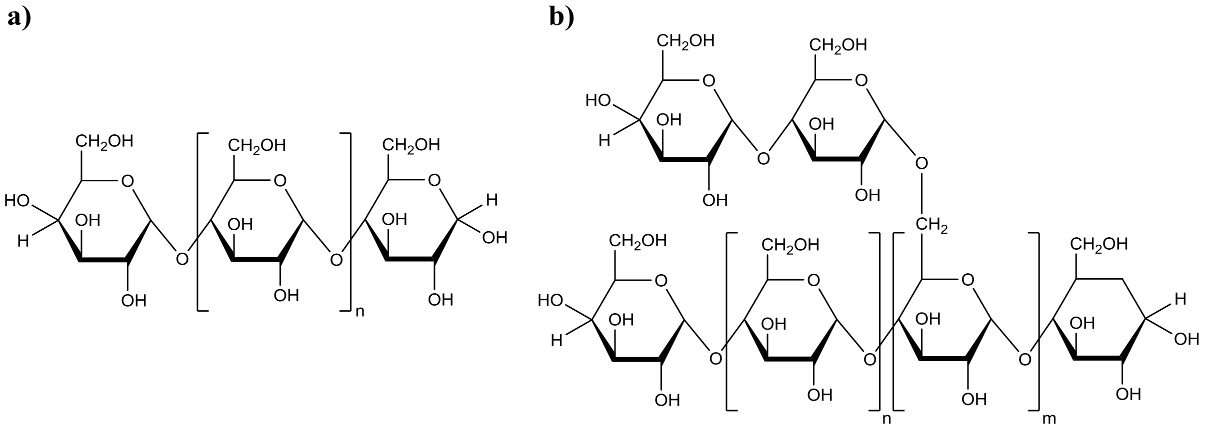

Figure 1. 6: Starch chemical structure consisting of **a)** amylose (linear) and **b)** amylopectin (branched) macromolecular structures.

Native starch granules are used as fillers in synthetic polymers to enhance final plastics biodegradability.[27] This is because the starch portion is consumable by microorganisms and the remaining synthetic polymers skeleton is more prone to degradation by natural elements attack such as thermal oxidation and ultraviolet photo-degradation. Therefore, starch has gained great attention to be blend with synthetic polymers because of its ability to accelerate biodegradation and availability in abundance at cheap prices.[28]

Moreover, native starch can be processed in the presence of plasticizers such as water or low molecular weight polyols able to disrupt its highly organized granules. Indeed, starch films can be obtained from the native starch by two main techniques: water solution casting and subsequent drying (wet method) and thermoplastic processing (dry method).[29] According to the wet method, starch films can be formed from a film-forming dispersion, or an emulsion, which contains a high percentage of water.[30] However, this process is too time-consuming and is not suitable for large-scale production.[31] The dry method involves the addition of a plasticizer such as glycerol into starch to improve its processability and obtain a thermoplastic starch.[32] The dry film-forming process is much more efficient and more suitable for large-scale production.[33]

Lignin comprises a complex family of aromatic polymers that are present mainly in secondary thickened plant cell walls. Industrially, it is obtained as a by-product in the productive process of cellulose-rich pulp fibres. The structure of lignin is complex and changes according to biomass source: it is constituted by phenylpropane monomers as repeating units known collectively as "monolignols": p-coumaryl, coniferyl, and sinapyl alcohol (Figure 1. 7).[34] The phenylpropane building blocks are randomly connected through carbon-carbon and carbon-oxygen bonds.

Lignin applications include the use in hydrogels [35], composite and nano-composite polymeric systems [36], carbon fibers [37], epoxy resins [36], and thermoplastics [38].

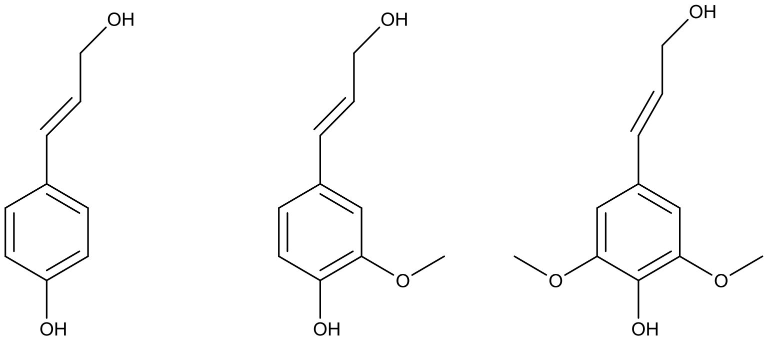

Figure 1. 7: Monolignols chemical structures: to the left coumaryl, coniferyl and sinapyl alchol.

Chitin is the second most abundant natural polymer on earth. Chitin occurs in nature as structural component in the exoskeleton of arthropods and in the cell walls of fungi and yeast. The main commercial sources exploited are crustacean, shrimp and crab shells. Chitin consists of a linear chain of β-(1,4)-N-acetyl-D-glucosamine units and form crystalline microfibrils as well as cellulose as shown in Figure 1. 8.

Chitosan is produced from chitin by fully or partially deacetylation under alkaline conditions or by enzymatic hydrolysis.[39] Thanks to its ready solubility in dilute acids, chitosan is more easily accessible for utilization and chemical reactions.

Chitin and chitosan have been shown to be useful as a wound dressing materials, drug delivery vehicles and interesting candidates for tissue engineering.[40]

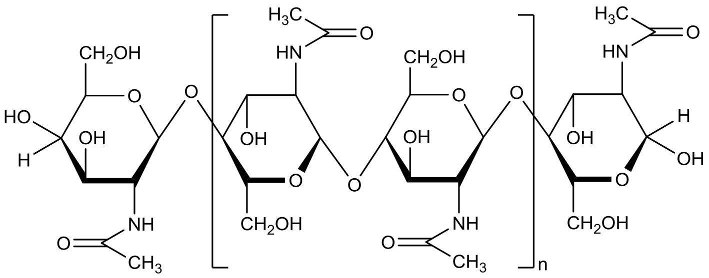

Figure 1. 8: Chitin chemical structure: linear chain of β-(1,4)-N-acetyl-D-glucosamine units.

1.4.2 Polymers obtained through biomass fermentation by microorganism

Polyhydroxyalkanoates (PHAs) are a family of aliphatic polyesters which are synthesized by bacteria as energy reserve when an excess of carbon source is present and nutrients such as nitrogen and phosphorus are available in limiting conditions. These compounds are stored in granules localised in the cell cytoplasm and degraded and used once the limiting nutrient is provided to the cell.[41] The general structural formula is shown in Figure 1. 9. Depending on the number of carbon atoms in the chain PHAs can be divided into three groups: short-chain length (SCL), which consist of 3-5 carbon atoms, medium-chain length (MCL), which consist of 6-14 carbon atoms and long-chain length (LCL) which count more than 15 carbon atoms. This family of bacterially synthesized polyesters is completely biodegradable, biocompatible and thermoprocessable. Because of these peculiarities, PHAs have found applications in the form of packaging materials, including films, boxes, coatings, fibers and foam materials, medical implants and drug delivery carriers. In spite of their numerous advantages, PHAs have yet not been able to replace conventional plastics on a large scale because of high cost coupled with difficulties of extraction and impact of the purification procedures.[42]

Poly(3-hydroxybutyrate) (PHB) was the first discovered member of the PHA family and it is also the most widely studied and characterized. It has properties very similar to conventional plastics, such as polypropylene (PP): high melting temperature and relative high tensile strength. However, although PHB can be extruded, moulded, made into films, it is highly brittle with poor elastic properties. For this reason PHB is commonly blended or copolymerized with longer side chain PHAs.[41]

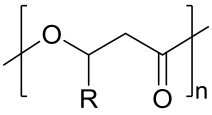

$R = H$	Poly(3-hydroxypropionate)
$R = CH_3$	Poly(3-hydroxybutyrate)
$R = CH_2CH_3$	Poly(3-hydroxyvalerate)
$R = (CH_2)_2CH_3$	Poly(3-hydroxyhexanoate)
$R = (CH_2)_4CH_3$	Poly(3-hydroxyoctanoate)

Figure 1. 9: General structural formula of polyhydroxyalkanoates (PHAs).

1.4.3 Polymers obtained through synthetic polymerization of monomers from biomass

Polymers obtained through polymerization of bio-derived monomers are classified as bio-based polymers even if the process is synthetic. These polymers are entirely (100 w/w%) bio-based if all their monomers derive from renewable sources, otherwise they are partially bio-based if both bio- and fossil- derived monomers are used in the polymerization. These polymers can be classified in two classes depending on the type of monomers:

I. bio-derived monomers chemically identical to fossil-derived monomers that generate polymers having the same features as the petrochemical counterparts;
II. bio-derived monomers able to generate polymers having different features compared to the well-known petrochemical polymers.

The first class includes commodity plastics as polyethylene, polypropylene, poly(vinyl chloride) and poly(ethylene terephthalate) that differ from the fossil-derived plastics only for the bio- derivation. The second class includes polymers such as poly(lactic acid), poly(butylene succinate) and poly(ethylene furandicarboxyate).

Bio-based polyethylene (bio-PE): Polyethylene (chemical structure in Figure 1. 10a) is an aliphatic polyolefin that represent more than 30% of the global plastics market. The monomer ethylene or ethene ($CH_2=CH_2$) is produced by the petrochemical industry from hydrocarbons (ethane, propane, or naphtha) subjected to a catalytic thermal cracking with steam at high temperatures. Currently, with the aim of exploiting renewable raw materials, ethylene can be produced from the catalytic dehydration of bioethanol. Starting from bioethylene, bio-polyethylene (bio-PE) is produced. Bio-PE retains the same features of PE: it is a non-biodegradable plastic which differ from the petrochemical product only for the derivation.[43]

Bioethanol obtained by the fermentation of sugarcane and molasses and also by hydrolysed starch from corn grains is classified as first generation (1G) bioethanol. Braskem, a Brazilian company created in 2002, is the leading producer worldwide of bioPE based on 1G ethanol from the sugar cane accounting for 200 ktons/year.[44] Second generation (2G) bioethanol is produced from lignocellulosic biomass (agricultural wastes, wood, and grasses) and has a huge potential because lignocellulosic biomass is the most abundant carbohydrates source in the world and does not compete with food production.[43] Currently, 2G bioethanol production accounts less than 1% of the total bioethanol production (200-350 million litres in 2017).[45] It’s worth noting that the current research and technology focus on the third generation (3G) bioethanol produced from algal biomass. Algal biomass has no competition with agricultural food and feed production and, if compared to lignocellulosic biomass, has increased fermentation efficiency. Owing the low content of hemicellulose and about zero content of lignin, algal biomass is considered more suitable to substitute conventional crops because of its high level of carbohydrates.[46]

Bio-based polypropylene (bio-PP): Polypropylene (PP), which belongs to the polyolefin group, is the second most produced commodity plastic with the main market in the automotive (chemical structure in Figure 1. 10Bb). Bio-based polypropylene can be manufactured using a variety of raw materials and production processes. Indeed, the monomeric unit propylene can be produced from biomass *via* various processes [47]:

- Dimerization of ethylene into 1-butene, followed by isomerization into 2-butene. Metathesis of ethylene and 2-butene yielding propylene. In this process, the propylene is entirely derived from ethanol.
- Dehydration of n-butanol into 1-butene, followed by isomerization into 2-butene. Metathesis of ethylene and 2-butene yielding propylene.
- Acetone-butanol-ethanol (ABE) fermentation of sugars to acetone. Reduction of acetone to isopropanol, followed by dehydration to propylene.
- Fermentation of sugars into isopropanol, followed by dehydration into propylene.
- Dehydrogenation of propane from glycerol, a by-product of diesel production from natural oils and fats.

Even if the processes from ethanol or ethanol and n-butanol are the most likely possibilities, currently it is unclear which process is the most favourable to produce bio-based propylene. At the moment there is no technology that can compete with the cost-effective production of synthetic polypropylene and this is the reason why companies are hesitant to enter the market. This threatens to result in limited commercial production of bio-based polypropylene. The global bio-based polypropylene market was evaluated at $32.0 million in 2017.[48]

Bio-based poly(vinyl chloride) (bio-PVC): Poly(vinyl chloride) (chemical structure in Figure 1. 10c) is a polyolefin and represents the third most produced commodity plastic: it is widely utilized in the construction sector as well as for pipes and electric cables. Most PVC products contain plasticizers in order to make pure polymer softer and more flexible. In addition, because of its application sector, it requires the incorporation of other additives such as heat stabilizers, UV stabilizers, flame retardant, blowing agents, smoke suppressor and so on. As for polyethylene and polypropylene, strong efforts have been done to replace synthetic

PVC material with bio-based poly(vinyl chloride). Vinyl chloride can be obtained by conversion of ethylene (from ethanol by dehydration) with chlorine into 1,2-dichloroethane, followed by dehydrochlorination. In 2019, INOVYN launched its production of bio-PVC under the brand name BIOVYN™, becoming the world's first commercial producer of bio-attributed PVC using bio-ethylene.[49] Efforts to replace traditional plasticizers are also under study. For example, several companies have created bio-based plasticizers to replace phthalates, reportedly with no reduction in PVC flexibility or other properties.[50]

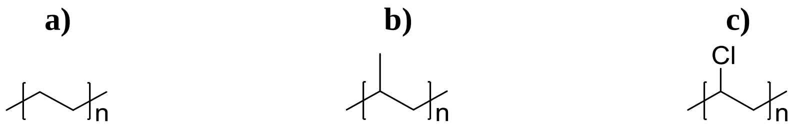

Figure 1. 10: Chemical structure of **a)** polyethylene (PE), **b)** polypropylene (PP), **c)** poly(vinyl chloride) (PVC).

Bio-based poly(ethylene terephthalate) (bio-PET): Poly(ethylene terephthalate) is a semi-aromatic polyester (chemical structure in Figure 1. 11) used as thermoplastic material e.g. for water and soft drink bottles, for clothing fibres, tyre cords and for glass-reinforced resins. PET faces some of the strongest public pressure to be 100% sourced from renewable feedstocks. This pressure has been augmented by the aggressive awareness campaign of US-based beverage giants Coca-Cola and Pepsi. PET is produced from ethylene glycol and terephthalic acid or dimethyl terephthalate which react to produce the monomer bis(2-hydroxyethyl) terephthalate.

Currently, partially (30 w/w%) bio-derived PET using ethylene glycol is widely used commercially. Consequently, the synthesis of bio-based terephtalic acid (TPA) is a required step for producing 100% bio-based PET. In 2011, Coca-Cola entered into agreement with Gevo and Virent to bring 100% PlantBottle technology to commercial scale through two different bio-based routes to para-xylene, which is a precursor for TPA.[51] Gevo developed an integrated method to convert forest residues to isobutanol [52] which can in turn be processed into p-xylene.[53] Virent devised the BioForming™ process technology which can convert biomass-derived sugars to fuels and chemicals, including aromatics.[54] The process consists of three key steps: 1. catalytic hydrogenolysis of an aqueous carbohydrate steam to produce low molecular weight oxygenates; 2. aqueous phase reforming to reduce the oxygen content of the feed; 3. conversion of the monooxygenates and hydrocarbons steam into aromatics: benzene, toluene and xylenes.[55,56,57] In 2015, Virent announced the use of its bio-based p-xylene (bio-PX) for the world's first demonstration-scale production of a PET plastic bottle made entirely from plant-based materials which was presented at World Expo hosted in Milan.[58]

Besides, a significant effort has focused on the development of synthetic pathways for bio-based TPA production without the formation of p-xylene as an intermediate.[59] Most of the approaches reported in the literature are based on the Diels-Alder reaction: TPA can be produced from muconic acid and ethylene [60] or from isoprene and acrylic acid passing through p-toluic acid.[61] Alternatively, TPA can be obtained from terpene, terpenoid, or combination thereof, extracted from a biological source such as lemon, thyme, camphor.[62]

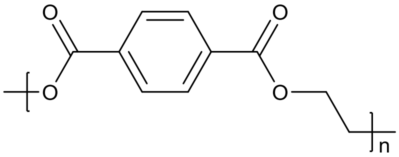

Figure 1. 11: Chemical structure of poly(ethylene terephthalate) (PET).

Poly(butylene succinate) (PBS): Poly(butylene succinate) (Figure 1. 12) is an aliphatic polyester which finds several applications as biodegradable material, e.g. mulching films, compostable bags, nonwoven sheets and textiles and foams. It is manufactured *via* polycondensation of monomers succinic acid and 1,4-butanediol, which are commonly obtained from fossil resources and are readily available on the market. PBS is commercially available since 1993: it is produced under the tradename Bionolle™ by Showa-Denko[63] and by Mitsubishi Chemical Corporation under the tradename GSPla™.[64] Interestingly, both monomers can be obtained not only from oil feedstock but trough fermentation of renewable feedstocks by microorganism as well. The bacterial production strains that are capable of producing succinic acid from glucose sources are recombinant *Escherichia coli*, *Mannheimia succiniciproducens*, and *Anaerobiospirillum succiniciproducens*.[65,66] Various companies such as Succinity® (a joint venture between BASF and Corbion), Roquette, BioAmber and Myriant are studying in the production of bio-succinic acid at industrial scale starting from different substrate: starch, sugar beet, wheat and lignocellulose. The so-obtained succinic acid can be converted into 1,4-butanediol through hydrogenation.[67] This would lead to a complete bio-based PBS.

PBS is commonly synthesized by polycondensation in two steps: in the first one, esterification with removal of water occurs while in the second, the removal of the excess of BD allows obtain high molecular weight PBS.[68] The catalyst most common used is titanium (IV) butoxide (TBT); nevertheless, the use of enzymatic catalysis has been explored as well. Lipase from *Candida antarctica* has been tested on the direct polycondensation of dimethyl succinate and ring opening polymerization of cyclic oligomers (firstly obtained by lipase catalysed condensation of DMS and BD).[69,70] Even if in both cases the ester –dimethyl succinate– has been employed, the positive results achieved have demonstrated the availability of a greener route to the PBS synthesis. However, in the interest of fairness, mention should also be made of the issues related to enzyme leaching and inactivation and the use of solvents to avoid polymer precipitation. These constraints hamper the diffusion of enzymatic catalysis to produce PBS on an industrial scale.

PBS is a thermoplastic material suitable in melt processing to obtain consumer goods. It is a semicrystalline material with a melting temperature value between 110-130 °C and a glass transition temperature below room temperature between -34 and -15 °C.[71] Despite its good flexibility (elongation at break ca. 560%), PBS exhibits brittle behaviour with a Young's modulus (E) of about 300-500 MPa and a tensile strength of about 20 MPa. This behaviour can be mitigated through different strategies such as copolymerization, polymer blending and fiber reiforncement.[66,72,73,74,75]

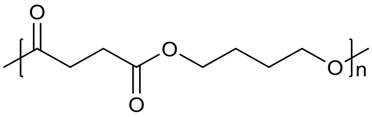

Figure 1. 12: Chemical structure of poly(butylene succinate) (PBS).

Poly(lactic acid) (PLA): Poly(lactic acid) is an aliphatic polyester obtained from 2-hydroxy propionic acid also called lactic acid monomer. Lactic acid is a chiral molecule, consisting of two optical isomers as shown in Figure 1. 13: L-(+)-lactic acid and D-(−)-lactic acid that can be produced by chemical synthesis or bacterial fermentation. Chemical synthesis of lactic acid is mainly based on the hydrolysis of lactonitrile, a derivative of petrochemicals, by strong acids, which provides only the racemic mixture of D-and L-lactic acid. On the contrary, bacterial fermentation allows obtaining high product stereospecificity as fermentation-derived lactic acid typically consists of 99.5% L-isomer and 0.5% D-isomer. The optical purity of lactic acid is a crucial parameter in PLA synthesis and final properties since it affects crystallization. Besides specificity, significant advantage of biotechnological production of lactic acid is that can use cheap raw materials such as molasses, starchy waste, cellulosic and other carbohydrate rich materials.[76,77]

L-(+)-lactic acid
(S)-2-hydroxypropanoic acid

D-(-)-lactic acid
(R)-2-hydroxypropanoic acid

Figure 1. 13: Lactic acid optical isomers: L-(+) and D-(-)-lactic acid.

Poly(lactic acid) which is produced by a synthetic pathway is a biodegradable and thermoformable polyester well suited for disposable applications.[78] It can be produced by direct polycondensation of lactic acid or ring-opening polymerization through lactide intermediate (Figure 1. 14). Lactide is the cyclic intermediate dimer that results from depolymerisation of PLA oligomers formed by removing water under mild conditions and without solvent. Polymerization through lactide formation is being industrially accomplished for high molecular weight PLA production.

NatureWorks LLC is the major producer of PLA under the tradename of Ingeo, with a capacity of 150000 metric ton per year in its US manufacturing facility (in Blair, Nebraska).[79]

PLA has a glass transition temperature above room temperature at around 55 °C and a melting temperature value between 170 - 180 °C.[80] PLA exhibits a Young modulus of around 3 GPa, a tensile strength between 50 and 70 MPa with an elongation at break of ca. 4%, and an impact strength close to 2.5 kJ m^{-2}.[81] Despite its brittleness, properties like good appearance, high mechanical strength, low toxicity and acceptable barrier properties have broadened its applications especially in food packaging which represent 70% of the PLA market.[82]

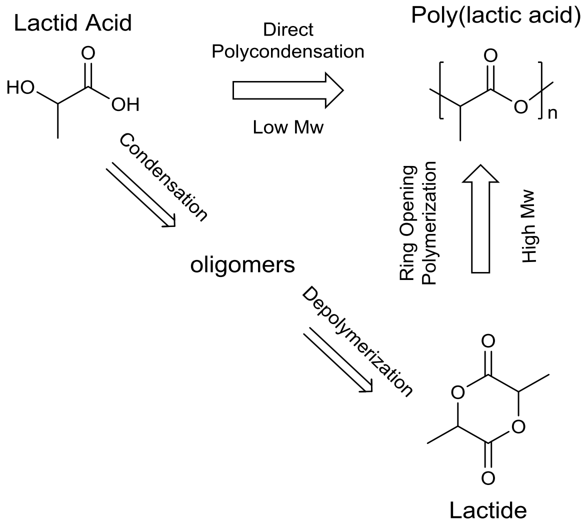

Figure 1. 14: Synthetic pathways for poly(lactic acid) production from lactic acid.

Poly(ethylene 2,5-furandicarboxylate) (PEF): Poly(ethylene 2,5-furandicarboxylate) (Figure 1. 15) is the most spotlighted member of the furandicarboxylic acid polyesters family since it is the furan counterpart of the engineered polyester poly(ethylene terephthalate) (PET).[13] PEF is 100% bio-derived: the monomers ethylene and FDCA come from renewable sources. Therefore, PEF is a completely bio-derived alternative to PET that can replace this last as for example in the packaging of soft drinks, water and alcoholic beverages.[83]

FDCA is obtained from the oxidation of 5-hydroxymethylfurfural (HMF) that is in turn produced by acidic dehydration of hexoses e.g. glucose. HMF production is known since the 19th century but the search for efficient and large-scale production was implemented in recent decades in view of a sustainable production of chemicals. The conversion of HMF into FDCA is an oxidative process that has been addressed using distinct types of catalysts, e.g. Pt/C nanoparticles [84], and oxidation conditions.[85,86] Very recently, Kang *et al.*[87] described an alternative route to the HMF pathway, based on the conversion of lignocellulosic biomass into 5-chloromethylfurfural, followed by its conversion into 5-acetoxymethylfurfural that allowed obtaining the latter in >99.9% purity. The interest in this route relies on the high stability of 5-acetoxymethylfurfural, the simplicity of its purification and ultimately its simple conversion into FDCA. However, at the moment, purified FDCA is produced on the multi-ton scale only by Avantium whose process is based on the air oxidation of a HMF derivative. Indeed, in the Avantium process 5-(methoxymethyl)-2-furfural is converted into FDCA in a single step using a catalytic system based on Co/Mo/Br.[88]

PEF is produced by a 2-stage melt polymerization approach: (i) a first stage esterification reaction of FDCA with EG carried out under nitrogen and heating up to 215 °C followed by (ii) a second stage transesterification reaction with increasing temperature up to 245 °C in order to increase the polyester degree of polymerization.[89] PEF is a semicrystalline material displaying a glass transition of around 80 - 85 °C and a melting endotherm at 210 - 215 °C.[13] The stress-strain curve analyses show that PEF has a Young's modulus of 2070 - 2450 MPa, a maximum stress of around 35 - 67 MPa and an elongation at break of only 3 - 4%.[90,91] PEF exhibits excellent barrier properties against oxygen, carbon dioxide and water. This peculiarity will be discussed deeper in the next paragraph. In view to replace commercial PET, some studies [92,93] evaluated the economic cost of PEF production and pointed out an optimistic view predicting FDCA price below TPA and competitive prices for PEF when produced on a large scale [93] and when proper prices for by-products (e.g. furfuryl ethyl ether) are applied. Great effort is now devoted to the rapid industrial development and marketing of FDCA. In this vein, Avantium established partnerships with Swire Pacific, the Coca-Cola Company, Danone and Alpla, among others, in a unique consortium and a financing close to € 36 million aimed at turning PEF into a business reality.

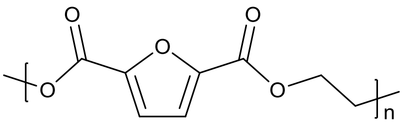

Figure 1. 15: Chemical structure of poly(ethylene 2,5-furandicarboxylate) (PEF).

1.5 Properties of novel bio-based polymers

The efforts made to replace fossil sources with renewable ones have shed light on novel organic compounds deriving from biomass that can be used as building blocks in polymer science to produce new materials that often present valuable properties. Most relevant polymers obtained from novel bio-derived monomers have been listed in the previous paragraph, i.e. poly(buyhylene succinate), poly(ethylene furandicarboxilate), poly(lactic acid), but a great variety of new polymers belonging to this class, e.g. poly(ricinoleic acid), are object of research and under development. Pursuant to a sustainability model of development, research similarly found out the PHAs polymers that are directly produced from biomass fermentation. It's worth noting that besides the sustainable derivation, the interest in these new polymers also derives from their peculiar properties related to the unique chemical structures coming from nature.

Because of their natural structure, PHAs can be biodegraded in both aerobic and anaerobic conditions in many different ecosystems including sea water.[94,95] PHA-degrading bacteria have been isolated from soil (*Pseudomonas lemoignei*, *Comamonas sp.*, *Acidovorax facilis, Aspergillus fumigatus and Variovorax paradoxus*), activated sludge (*Alcaligenes faecalis, Pseudomonas fluorescens)* and anaerobic sludge (*Ilyobacter delafieldii*), sea water (*Comamonas testosterone*) and lake water (*Pseudomonas stutzeri*). The effect of different environments on the degradation rate has been studied and, for example, it was reported that the copolymer poly(3-hydroxybutyrate-*co*-3-hydroxyvalerate) was completely degraded after 6, 75, and 350 weeks in anaerobic sewage, soil, and sea water, respectively.[94,96,97,98] The ability to degrade in many different ecosystems is a unique peculiarity of the PHAs family which match perfectly well environmental purposes.

Another key example is represented from the furandicarboxylic acid (FDCA) polyesters family which have received recent attention due to excellent barrier properties coupled with their renewable sourcing. As previously mentioned, poly(ethylene 2,5-furandicarboxylate) is the furan counterpart of polyester poly(ethylene terephthalate) (PET) and while FDCA is strictly similar to therephtalic acid (TPA) differences in ring size, polarity, and linearity result in significantly different performances. TPA is a phenyl ring (aromatic ring with 6 carbon atoms) while FDCA is a furan ring (five-membered aromatic ring with four carbon atoms and one oxygen) as shown in Figure 1. 16. Moreover, the linear *p*-phenyl connection in TPA results in an angle of 180° between carboxylic acid carbons while the nonlinear structure of FDCA yields an angle of 129.4°. Investigation of subambient mechanical relaxation behaviour of PEF and PET by dynamic mechanical analysis (DMA) revealed that below Tg, both phenyl ring-flipping and carbonyl motions contribute to the relaxation behaviour of PET while the ring-flipping in PEF is strongly hindered such that only the carbonyl motions are believed to contribute to the subambient relaxation behaviour of PEF. Furan ring-flipping in PEF is frustrated by the non-linear axis of rotation coupled with ring polarity.[99] As a result, even if PEF is characterized by higher free volume than PET, it shows improved barrier properties since its rigidity results in reduced penetrants diffusion coefficients and hence permeability. PEF exhibits a reduction in oxygen permeability of a factor of ~10× compared to PET, i.e. 0.011 *vs* 0.114,[100] and a reduction in carbon dioxide permeability of a factor of ~19×, $P_{CO_2} = 0.026$ for PEF and 0.49 for PET.[101]

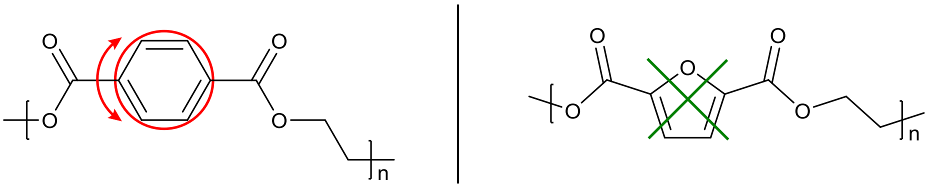

Figure 1. 16: Chemical structures of poly(ethylene terephthalate) PET, and poly(ethylene 2,5-furandicarboxylate) PEF.

PEF represents a key example of the advantage of developing new polymers from novel bio-sourced building blocks with the aim of replacing commercially used polymers in specific applications. It's worth noting that the difference between PEF and bio-based PET is not the bio-derivation since both can be obtained from biomasses but regards the final performances of the two materials which depend on their chemical structures: bio-PET retains the same features of PET while PEF paves the way for innovative applications.

Another example of this approach is ricinoleic acid and its homopolymer poly(ricinoleic acid). Ricinoleic acid is the main constituent of the natural plant oil *castor oil* and it is an unsaturated fatty acid containing a secondary –OH group and a lateral aliphatic chain, with a notable steric hindrance. Poly(ricinoleic acid) (Figure 1. 17) is an amorphous polymer, with a glass transition temperature of about -75 °C, i.e. significantly low, indicating a very flexible chain that induces poor mechanical performances. Despite it hinders chain packing and hence crystallization, the presence of the aliphatic sidechains on the polymeric structure allows the material to express a strong biocidal activity towards microorganisms such as *Staphylococcus aureus* (mortality rate% = 100).[102] *S. aureus* is a Gram-positive bacterium and the long lateral aliphatic chain can penetrate its cell wall causing damage of the membrane and consequently cell death. The polymer exhibits lower antimicrobial activity (mortality rate% = 45.0 ± 3.2) on Gram-negative bacteria such as *Escherichia coli*. This is not surprising given the structure of Gram-negative bacteria that count an extra outer lipopolysaccharide membrane on the cell wall, acting as a permeability barrier so that uptake into the cell is reduced.

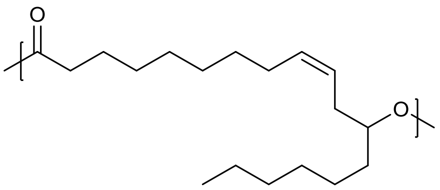

Figure 1. 17: Chemical structure of poly(ricinoleic acid) (PRA).

1.6 Bio-based building blocks

In order to move from a non-sustainable fossil-based model of development to a sustainable one, a number of organic compounds that can be obtained from biomass have been highlighted as platform chemicals in a key study conducted by the U.S. Department of Energy Efficiency and Renewable Energy. The study analysed both sugars [103] and lignin [104] as renewable sources.

Focused on sugars, the study identified twelve building block chemicals that can be produced *via* biological and chemical conversion. It deeply revised the routes for their production and subsequent conversion into value-added chemicals or materials. Building block chemicals, as considered for this analysis, are molecules with multiple functional groups that possess the potential to be transformed into new families of useful molecules. The twelve sugar-based building blocks shown in Figure 1. 18 are 1,4-diacids (succinic, fumaric and malic), 2,5-furan dicarboxylic acid, 3-hydroxy propionic acid, aspartic acid, glucaric acid, glutamic acid, itaconic acid, levulinic acid, 3-hydroxybutyrolactone, glycerol, sorbitol, and xylitol/arabinitol.

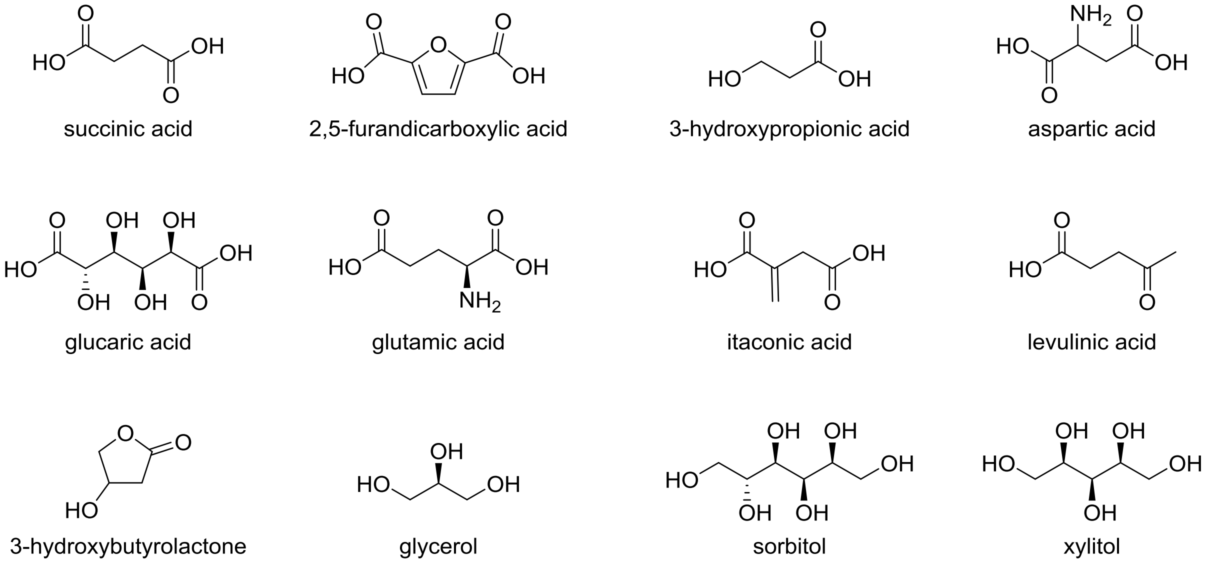

Figure 1. 18: Top twelve building block chemicals that can be obtained from sugars according to the study of the U.S. Department of Energy Efficiency and Renewable Energy.

The study also investigated the conversion of lignin to discrete building block molecules. Lignin is the only renewable source of an important class of organic compounds: the aromatics. Hence, the study promoted to break up lignin's macromolecular structure but maintain the aromatic nature of the building block molecules. Non-selective depolymerization of lignin could lead to benzene, toluene, xylene (BTX) and respective phenols whose can directly enter the conventional petrochemical processes. On the other hand, a very selective depolymerization could yield a high-value portfolio of complex aromatics that are difficult to produce *via* conventional petrochemical routes. These compounds are closely related to the basic building blocks of lignin and may be highly desirable if they can be produced in reasonable commercial quantity. Figure 1. 19 and Figure 1. 20 suggest possible structures that could be derived from the guaiacyl and syringyl units present in lignin. Two barriers would need to be overcome, however. First, technology allowing highly selective bond-scission need to be developed in order to capture the monomeric lignin building block structures. Development of this technology will be more difficult than the more aggressive processes that would yield BTX or phenols. Second, markets and applications for monomeric lignin building blocks would need to be investigated.

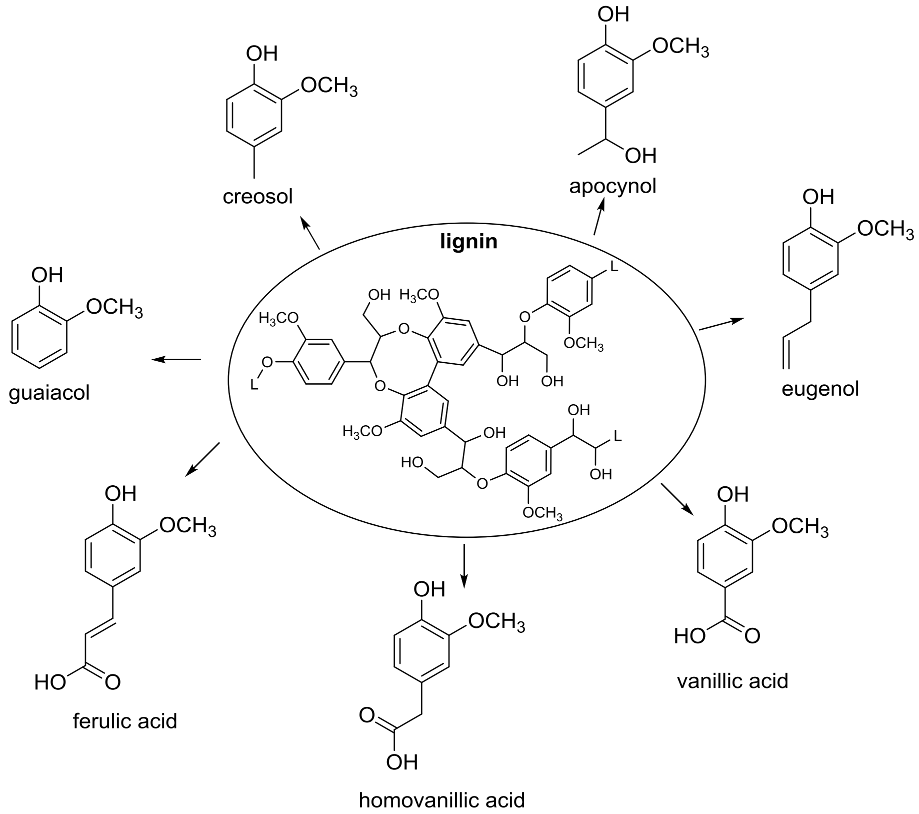

Figure 1. 19: Building block chemicals that can be obtained from guaiacyl unit of lignin.

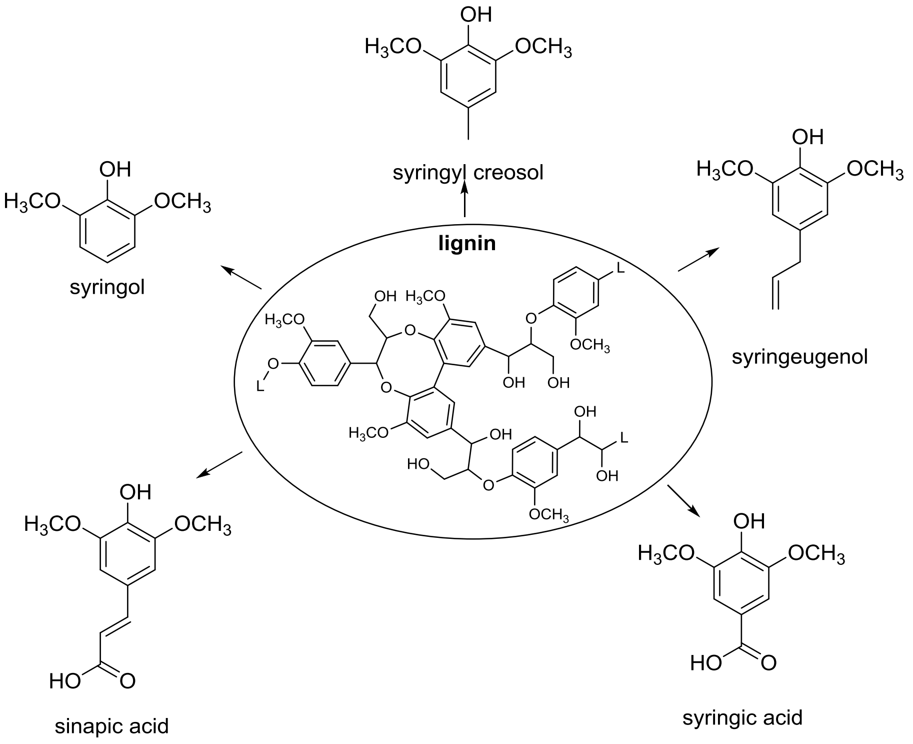

Figure 1. 20: Building block chemicals that can be obtained from syringyl unit of lignin.

Besides the building blocks coming from sugars and lignin highlighted from the study of the U.S. Department of Energy Efficiency and Renewable Energy, a healthy ferment of activities worldwide involving both academic and industrial sectors focus also on other valuable building blocks coming from renewable resources.[105,106,107] Among them it's worth mentioning lactic acid, isosorbide, mannitol, the family of terpenes and terpenoids, vegetable oils, tartaric acid and citric acid as reported in Figure 1. 21.

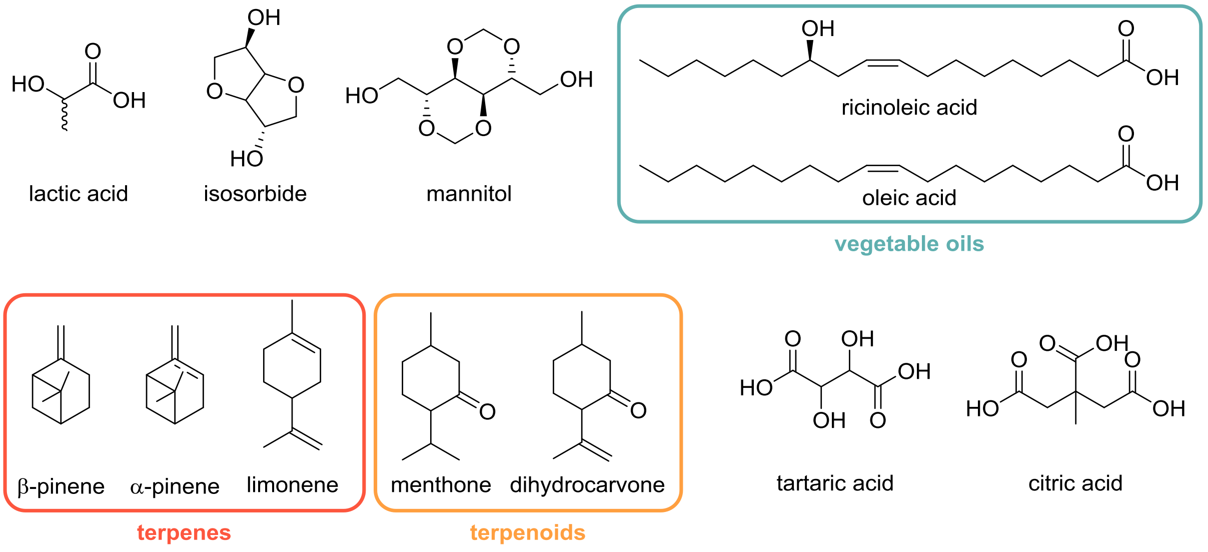

Figure 1. 21: Building block chemicals coming from different type of renewable resource.

Lactic acid, isosorbide and mannitol derive from biological or chemical conversion of sugars. Coming from plant oils, fatty acids as ricinoleic acid and oleic acid can be exploited as building block in polymer science or as precursors for the synthesis of bio-based monomers. Terpenes are predominantly derived from turpentine, the volatile fraction of resins exuded from conifers. The major constitutes are β-pinene, α-pinene and limonene. It is important to emphasize that R-limonene is also a by-product of the citrus industry. Terpenoids are natural products occurring in essentials oils bearing some structural resemblance to terpenes, but with functional groups like OH or carbonyl moieties as shown by menthone and dihydrocarvone. Citric acid and tartaric acid are the main by-product of the citrus and winery industry respectively.

CHAPTER 2: AIM OF THE WORK

Biomass, which includes crops, forestry, agricultural wastes and agro-industrial by-products, is not only a renewable and sustainable resource of energy, but also a source of value-added chemicals. In polymer science, the unique chemical structure of these compounds coming from their natural origin, as for example the presence of lateral double bonds, aromatic rings, polar rings, long flexible chains etc., is often conceived as an advantage for providing peculiar properties to the final polymers. The extraction/conversion and valorisation of these bio-based compounds as green building blocks for bio-based plastics is a great challenge that requires notable efforts to develop a fully sustainable value chain (Figure 2. 1). Indeed, from a chemical perspective, all processes must be safe, efficient in terms of yield and purity, covering all three pillars of sustainability: economic, social and environmental.

Figure 2. 1: Scheme of a value chain that start from biomass to obtain new polymers and applications.

In this context, the research work here presented aims at contributing to **develop the steps that start from high value compounds and move to polymeric materials of the value chains of two bio-based building blocks: itaconic and vanillic acids.** As shown in Figure 2. 2 the value chain of itaconic acid already finds in literature interesting developments while the exploitation of vanillic acid is a relatively new opportunity.

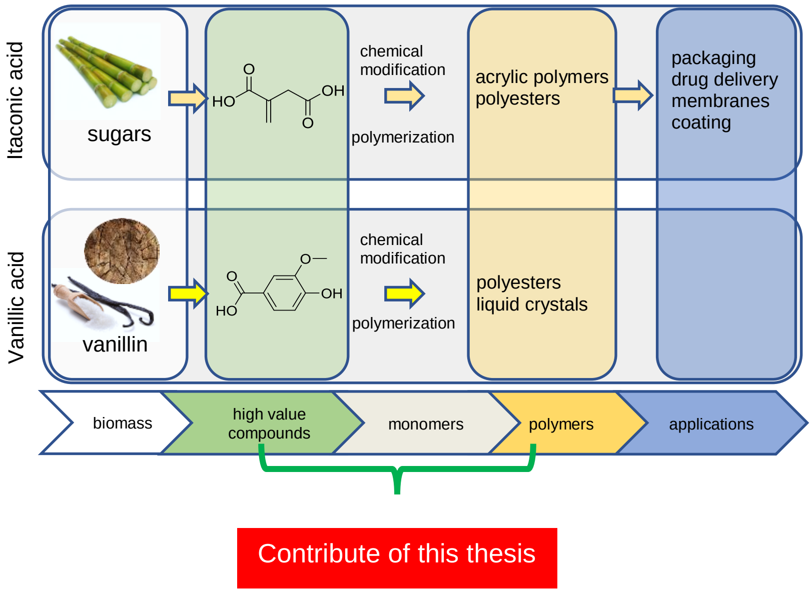

Figure 2. 2: Scheme of the two value chains with respect to the literature data.

Itaconic acid and **vanillic acid** have been chosen as key compounds because of their chemical peculiarities. Itaconic acid is a diacid with a short aliphatic chain and containing a double bond. Vanillic acid is a hydroxy acid with a *para*-substituted aromatic ring presenting a lateral methoxy group.

These chemical peculiarities can be exploited to obtain multifunctional building blocks suitable for polycondensation reactions to produce polyesters and copolyesters, using other bio-based comonomers (dimethyl 2,5-furandicarboxylate and ω-pentadecalactone). It is noteworthy that the new polymeric products have been designed to have some novel functionalities, such as antibacterial and antioxidant properties, tuneable segmental chains mobility, water vapor barrier properties, hydrophobicity, according to the specific potential applications, as reported in Figure 2. 3.

Therefore, this research work aims at studying and developing **novel sustainable synthetic pathways for the eco-design of new bio-based polymeric structures with high value functionalities and new potential applications** as thermosets or thermoplastic materials, for example in the fields of medical goods and smart food packaging.

In this way the thesis work tries to significantly contribute to the concepts of Bio-based Economy and Green Chemistry.

bio-based building block	peculiarity	chemical modification	polymerization	polyester functionalities	comonomer	added copolyester functionalities	possible applications
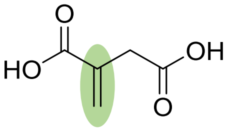 **itaconic acid**	double bond	functionalization with thiols HS-R 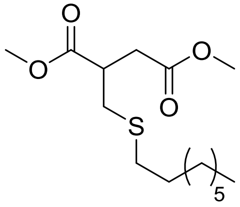	• 1,4-butanediol • CHDM • CHD • isosorbide ↓ transesterification ↓ polyesters	• high thermal stability • flexibility • antimicrobial activity • antioxidant	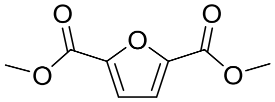 dimenthyl 2,5-furandicarboxylate	• rigidity	**• thermosets** **• antimicrobial products** **• flexible food packaging**
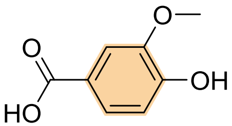 **vanillic acid**	aromatic ring methoxy group	etherification with EC 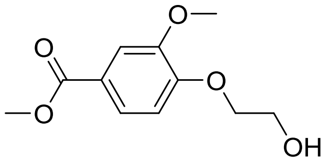	transesterification ↓ polyesters	• high thermal stability • rigidity • brittleness	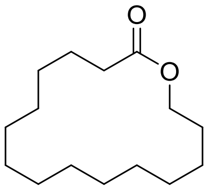 ω-pentadecalactone	• flexibility • hydrophobicity • water vapor barrier	**• flexible food packaging**

(EC = ethylene carbonate; CHDM = 1,4-cyclohexanedimethanol; CHD = 1,4-cyclohexanediol).

Figure 2. 3: Schematic representation of the two chains of research

CHAPTER 3: RESULTS AND DISCUSSION

3.1 Thia-Michael reaction for a thermostable itaconic-based monomer and the synthesis of functionalized bio-polyesters

3.1.1 Introduction

Itaconic acid (IA), declared as one of the top twelve chemicals from biomasses by the U.S. Department of Energy Efficiency and Renewable Energy [103], has recently received large attention. The biological synthesis of itaconic acid has been known since the mid-forties of the last century when IA was isolated from the growth medium of fungus *Aspergillus itaconicus*.[108] Currently, it is produced on an industrial scale (80000 tons/year) *via* fermentation of carbohydrate sources (glucose, starch and glycerol) deriving from agricultural wastes [109] using *Aspergillus terreus* and its production capacity is expected to grow 5.5% every year in the next 5 years.[110] Because of its multiple functionalities and the exponential growth of its biological production, IA and its derivatives such as dimethyl itaconate (DMI) are arousing interest as new building blocks in the field of bio-based polymeric materials. In fact, as shown in Figure 3.1. 1, by exploiting the double bond, it is possible to develop a radical polymerization; on the other hand, the double carboxylic groups could be subjected to polycondensation with diols to yield unsaturated polyesters.

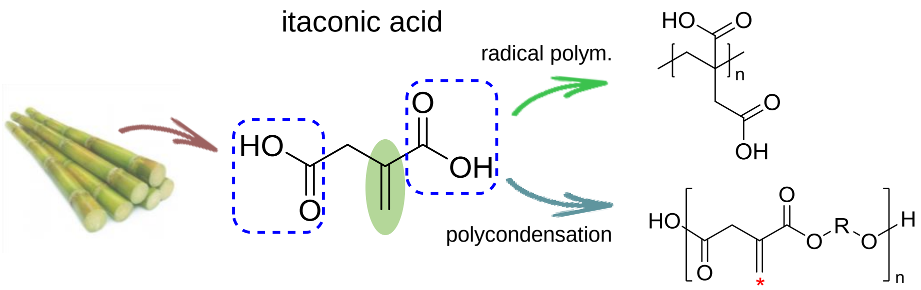

Figure 3.1. 1: Schematic representation of the exploitation of itaconic acid as building block in polymer science.

Thanks to these characteristics, IA has been extensively investigated as an alternative monomer or co-monomer to prepare acrylic polymers thanks to its similarity to acrylic acid. The first studies regarding the polymerization of itaconic acid were carried out by Marvel and Shepherd back in 1959.[111] They reported the homopolymerization of itaconic acid and its copolymerization with acrylic acid in aqueous solution using potassium persulfate as radical initiator.

Despite its promising role as building block for polyesters, IA presents some issues to be taken into account. Under typical polycondensation conditions, in fact, the double bond tends to isomerize and to promote crosslinking reactions. Moreover, the presence of the double bond weakens the electrophilicity of the adjacent COOH group thus affecting its reactivity.[112] To temper such effects, IA is often co-polymerized in a small amount with other saturated diacids or diesters thus reducing the density of the cross-linkable moiety. Barrett *et al.*[113] and Brännström *et al.*[114] synthesized different polyesters by thermal polycondensation of itaconic acid and a second dicarboxylic acid (adipic acid or succinic acid). They obtained oligomers suitable for coatings applications. Higher molecular weight polyesters including itaconic acid were synthesized by Guo *et al.*[115] and Wei and co-workers.[116] Guo combined IA with sebacic acid (10% molar ratio of IA) in the presence of a radical inhibitor and Ti (IV) butoxide as the condensation catalyst while Wei, in similar reaction conditions, combined succinic acid, sebacic acid and 5 - 15% molar ratio of itaconic acid. However, it is worth noting that crosslinking reactions have been limited by the rather low ratio of itaconic acid and the presence of inhibitors. The direct polycondensation of itaconic acid with different diols was reported by Dai *et al.*[117] but they stated to obtain only very low molecular weights itaconic-based oligomers in order to avoid crosslinking reactions. Enzymatic polymerization has been used to ensure mild reaction conditions for the direct polycondensation of IA. For example, this approach was followed by Barrett *et al.*[113] who demonstrated the successful polycondensation of dimethyl itaconate with different diols catalyzed by lipase B from *Candida antarctica* (CaLB). They were able to obtain oligomers with molecular weights of 2000 - 6650 g/mol. In this context, Gardossi and co-workers [112,118] developed a new type of enzymatic catalyst by covalently immobilize CaLB on an epoxy-functionalized methacrylic resin. In this way, they were able to polymerize DMI overcoming the problems of protein contamination and enzyme recyclability; however, also in this case, low molecular weight oligomers were obtained.

To the best of our knowledge, the current most successful direct polycondensation of itaconic acid was recently reported by Winkler and co-workers.[119] They polymerized dimethyl itaconate with different diols in the presence of 4-methoxyphenol as radical inhibitor and tin (II) ethylhexanoate as catalyst. The reactions were conducted at 130 °C yielding unsaturated poly(butylene itaconate) oligomers with molecular weights of about 9900 - 11500 g/mol. Remarkably, they investigated the possibility to exploit the unsaturation of DMI to graft functional groups by means of Michael addition reaction. In particular, thiols were successfully graphed on the unsaturated moieties of the synthesized oligomers. However, when the functionalization of dimethyl itaconate and the subsequent polymerization have been tested, a cross-linked material was obtained. Winkler ascribed this behavior to an undesired elimination of the thiol that re-forms the double bond.

The reported examples show that, despite its huge potential versatility, the exploitation of itaconic acid is still limited. It should be noted that only mild reaction conditions (relatively low temperature and presence of inhibitors) can be employed and that low molecular weights oligomers are obtained. Furthermore, the unexpected reactivity of the sulphide moiety, usually characterized by high stability, deserves more extensive studies. Indeed, a deeper understanding of the stability range and degradative processes involving IA derived structures could allow researchers to build a platform of new, stable and reliable functional monomers based on itaconic acid, suitable to yield high molecular weight thermostable polyesters. In addition, the possibility to introduce specific lateral groups, such as long aliphatic chains, could open to a new family of functional materials mimicking the natural biocidal activity expressed by ricinoleic acid.[102] Indeed, as stated by Totaro *et al.*, the presence of the aliphatic sidechains on the polymeric structure allowed poly(ricinoleic acid) to express a strong biocidal activity towards microorganisms such as *Escherichia coli* and *Staphylococcus aureus*. Moreover, the presence of sulfur onto the polymer backbone could provide oxidative resistance since polysulfides can be oxidized to polysulfones.[119]

Consequently, the objective of this work is devoted to study and develop a new method to exploit itaconic acid for the synthesis of a robust monomer that can be subjected to common polycondensation conditions of reaction to yield high molecular weighs polyesters characterized by specific lateral group that provide biocidal and antioxidant activity. Hereby, the functionalization of the unsaturated double bond of dimethyl itaconate by thia-Michael addition reaction using 1-octanethiol and the subsequent polycondensation with different diols (1,4-butanediol, 1,4-cyclohexanedimethanol, 1,4-cyclohexanediol and isosorbide) to yield a family of polyesters is presented. Additionally, the thio-functionalized monomer is subjected to copolymerization with dimethyl 2,5-furandicarboxylate in order to confer rigidity to the final copolyester and obtain a processable material. Finally, the biocidal activity ascribable to the long lateral group is investigated *via* plate counts by comparing antimicrobial properties of the new polyester presenting the inserted side chain and poly(butylene succinate) and poly(butylene 2-methylsuccinate) polyesters.

3.1.2 Thia-Michael reaction on dimethyl itaconate

The functionalization of the unsaturated double bond of dimethyl itaconate was achieved by adapting the thia-Michael addition reaction with thiols performed by Okada *et al.*[120] They reported that the itaconate-derived addition product was prepared by the addition reaction of alkyl mercaptan and dimethyl itaconate. DMI was specifically selected as substrate since itaconic acid would interfere with the alkaline environment of the reaction. The reaction between DMI and 1-octanethiol completed after 24 hours at room temperature in presence of K_2CO_3 (30 wt% to DMI) and acetone (Scheme 3.1. 1) yielding dimethyl 2-((octylthio)methyl)succinate (DOMS).

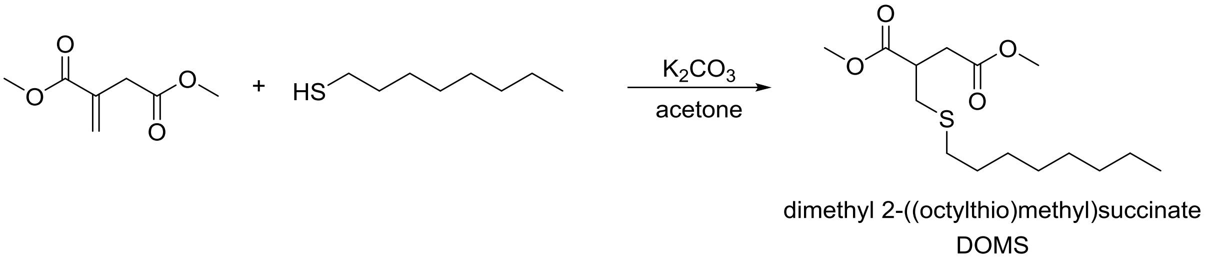

Scheme 3.1. 1: Synthesis of dimethyl 2-((octylthio)methyl)succinate (DOMS) by thia-Michael addition reaction.

The ^{1}H-NMR analysis confirms the complete functionalization of the double bond as shown by the disappearance of the signals at 6.33 and 5.72 ppm typical of the vinyl system and the appearance of the signals concerning the introduction of 1-octanethiol (Figure 3.1. 2).

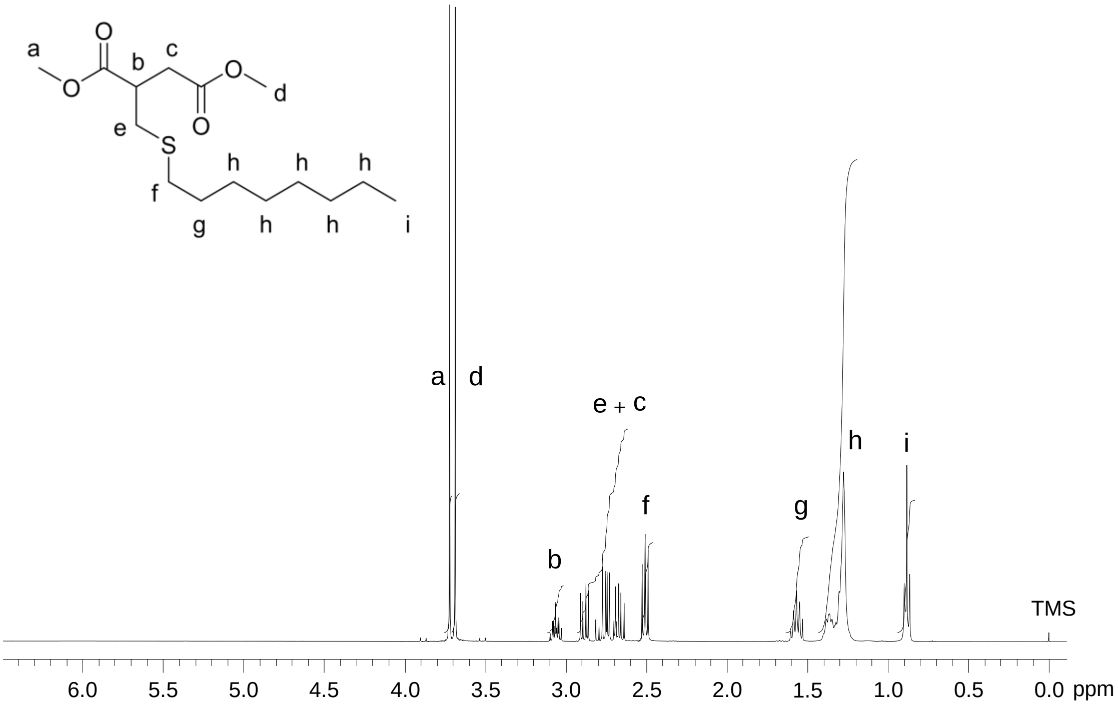

Figure 3.1. 2: ^{1}H-NMR spectrum of dimethyl 2-((octylthio)methyl)succinate.

The molecular mass and structural features of DOMS are confirmed by gas chromatography-mass spectrometry (GC-MS) shown in Figure 3.1. 3 where it appears clearly the peak at m/z 304 corresponding to the molecular mass of DOMS.

The FT-IR analysis reported in Figure 3.1. 4 demonstrates the complete absence of signals in the double bond region ($R_2C=CH_2$ stretching 1600 - 1700 cm^{-1}) as well as thiols (RS-H stretching 2500 - 2600 cm^{-1}) while the weak signal at 723 cm^{-1} is representative of the sulphide C-S stretching.

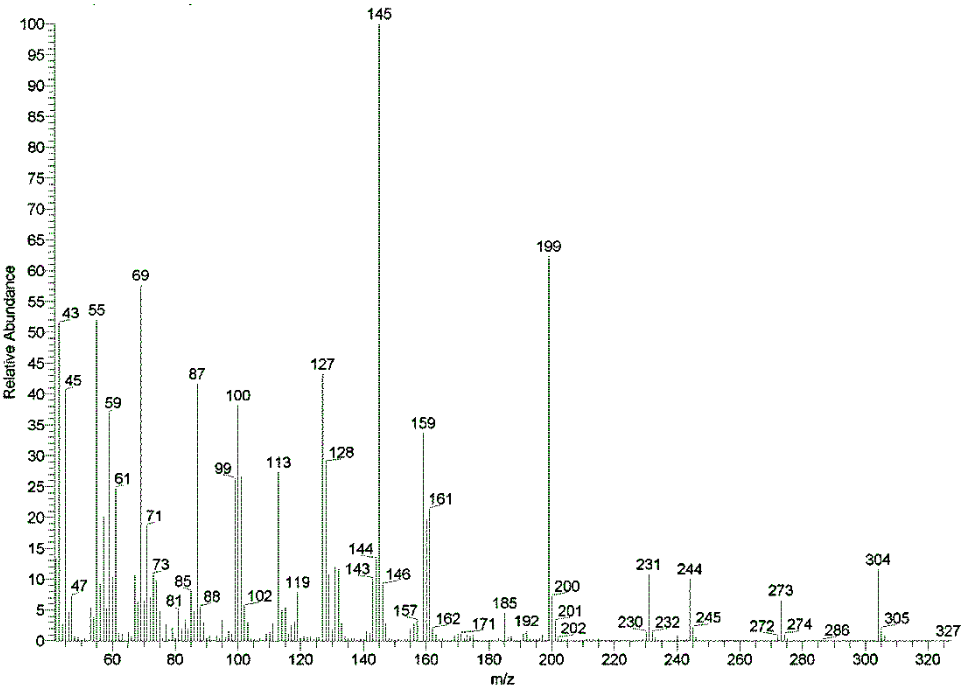

Figure 3.1. 3: Mass spectrum of dimethyl 2-((octylthio)methyl)succinate.

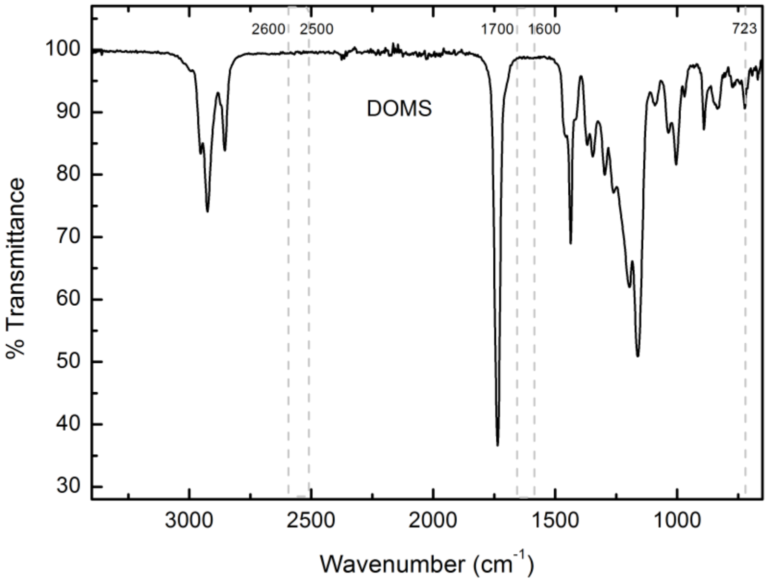

Figure 3.1. 4: FT-IR spectrum of dimethyl 2-((octylthio)methyl)succinate.

It is worth noting that the functionalization by thia-Michael shows a reaction yield of 99% and it does not require any purification step other than the filtration of potassium carbonate, thus increasing the sustainability of the entire process.

3.1.3 Stability tests for DOMS

Dimethyl 2-((octylthio)methyl)succinate (DOMS) was tested in order to assess its range of stability and determine the most suitable operative conditions for the subsequent polymerization. Thermogravimetric analysis (TGA) revealed no evident loss of weight other than after 258 °C, due to the evaporation of DOMS. Furthermore, a series of isothermal closed cup treatments were performed on DOMS in order to investigate its operative conditions. The thermal treatment test of the monomer for 5 hours at 200 °C did not evidence any undesired degradative process as confirmed by ^{1}H-NMR analysis and so did also in the presence of a glycol such as 1,4-butanediol. Additional tests were performed to evaluate DOMS stability at high temperatures in presence of a classical transesterification catalyst such as titanium (IV) butoxide (TBT) or protic acids. As reported in Figure 3.1. 5A, the monomer is stable in the presence of TBT even after 5 hours at 200 °C presenting only traces (below 1%) of dimethyl itaconate (6.33 ppm and 5.72 ppm) resulting from the elimination of 1-octanethiol. On the contrary, the presence of a protic acid such as octanoic acid (Figure 3.1. 5B), favours the elimination of the thiol with the formation of double bonds (6.33 ppm and 5.72 ppm) and oligomers (3.45 ppm and 2.31 ppm). Such effect is further enhanced in the presence of a strong acid such as p-toluenesulfonic acid (Figure 3.1. 5C). In this case, extensive degradation occurs resulting in a mixture of undesired sub-products and oligomers. The reported results demonstrate that, during the polymerization step, the presence of acid moieties must be avoided in order to prevent undesired crosslinking reactions previously reported in literature.[119]

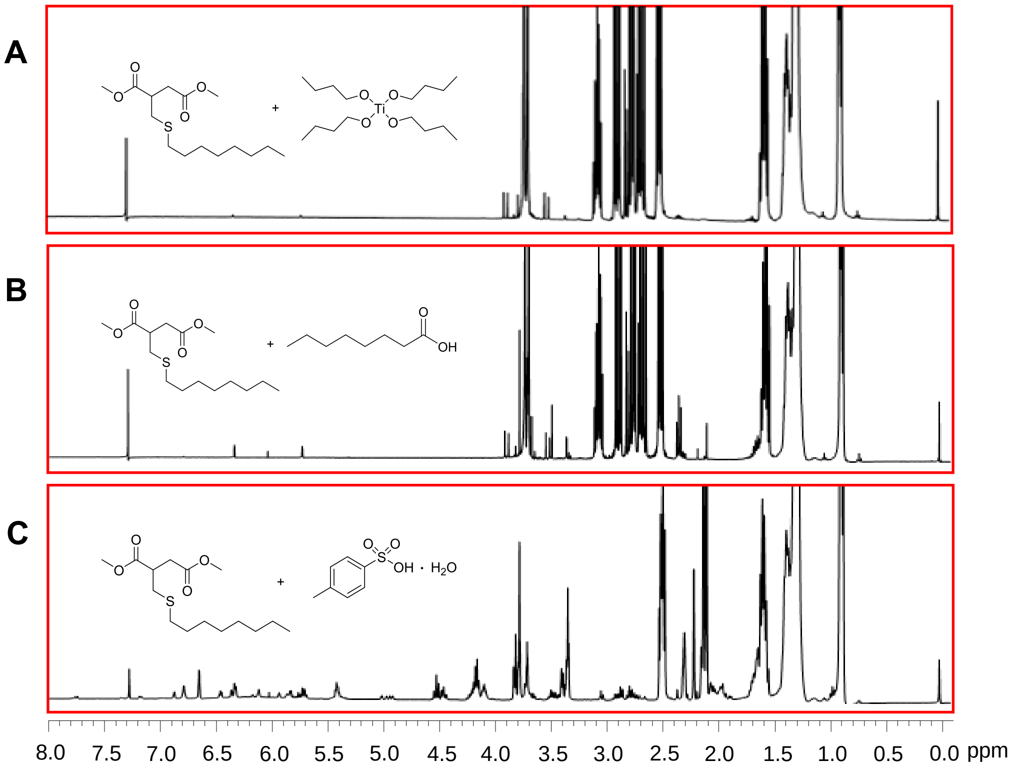

Figure 3.1. 5: ^{1}H-NMR spectrum of: **A.** DOMS in presence of TBT at 200 °C for 5 hours. **B.** DOMS in presence of octanoic acid at 200 °C for 5 hours. **C.** DOMS in presence of p-toluenesulfonic acid monohydrate at 200 °C for 5 hours.

3.1.4 Optimization of the polycondensation of DOMS with 1,4-butanediol

The polycondensation of dimethyl 2-((octylthio)methyl)succinate with 1,4-butanediol (named DOMS-BD) was studied firstly (Scheme 3.1. 2) and the reaction conditions were optimized by varying parameters such as the feed ratio (nBD/nDOMS), the catalyst type and content.

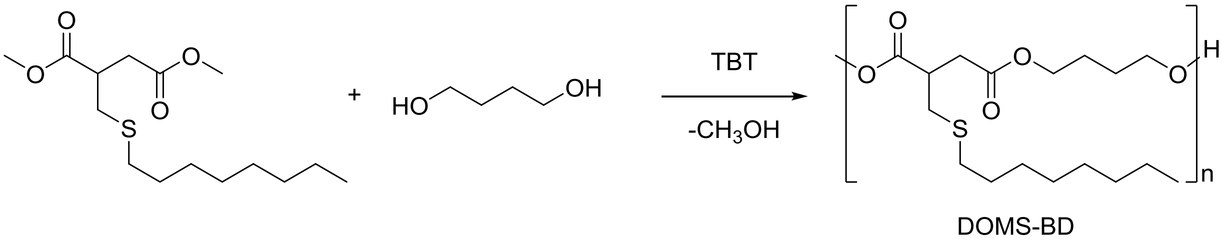

Scheme 3.1. 2: Synthesis of DOMS-BD by direct polycondensation.

On the basis of the thermostability of the monomer, the reactions were conducted at 200 °C for the first 2 hours and then gradually brought to 210 °C under reduced pressure (10^{-1} mbar) during the subsequent 3 hours. Common industrial transesterification catalysts such as titanium (IV) butoxide (TBT) and dibutyltin (IV) oxide (DBTO)[121] were tested. The synthesized polyesters resulted to be fully soluble in chloroform. Moreover, as shown by the ^{1}H-NR spectrum in Figure 3.1. 6, the appearance of the signals related to the butylene chain at

4.04 and 1.67 ppm and the disappearance of the ester terminals at around 3.67 ppm indicate the formation of high Mw polyesters. In addition, no signals related to undesired reactions like cross-linking as well as sub-products deriving from the alkylthio group scission can be detected. Such result is also confirmed by FT-IR analysis (Figure 3.1. 10). In fact, no signals related to double bonds formation appear evident while the signal at 723 cm^{-1} relative to the C-S bond is preserved. GPC analysis revealed homogeneous molecular weight distributions with low PDI. Therefore, all these experimental data indicate that polyesters without crosslinking were obtained.

The optimization of the reaction conditions was carried out by measuring the molecular weight variation and the respective Tg value of the polyesters. First of all, the influence of the feed ratio was studied, keeping constant the TBT catalyst content at 250 ppm to the final polyester weight (Table 3.1. 1, entries 1-5). By increasing the molar ratio of BD on DOMS from 1.05 to 2.00, the molecular weight of the polyester increases from 12000 to 107500 g mol^{-1}. Due to the high volatility of 1,4-butanediol (boiling point = 230 °C), the stoichiometry ratio can easily unbalance when BD is in slight excess (1.05) thus hampering the molecular weight growth (entry 1). The molecular weight of the polyesters is also influenced by the type of catalyst (entry 5 and entry 6). TBT proves to be more efficient as catalyst than DBTO in the same reaction conditions. Indeed, using DBTO as catalyst an oligomer of 8700 g mol^{-1} was obtained while high molecular weight polyester was achieved with TBT. As expected, the amount of catalyst influences the molecular weight as proven by entry 7, obtained using 175 ppm of TBT rather than 250 ppm. However, a molecular weight reduction of DOMS-BD polyesters from 107500 to 88800 g mol^{-1} can be warranted by a lower TBT catalyst utilization. Hence, from the polycondensation optimization, it resulted that the optimal conditions are a feed ratio (nBD/nDOMS) equal to 2 using TBT catalyst in an amount of 175 ppm to the final polyester weight.

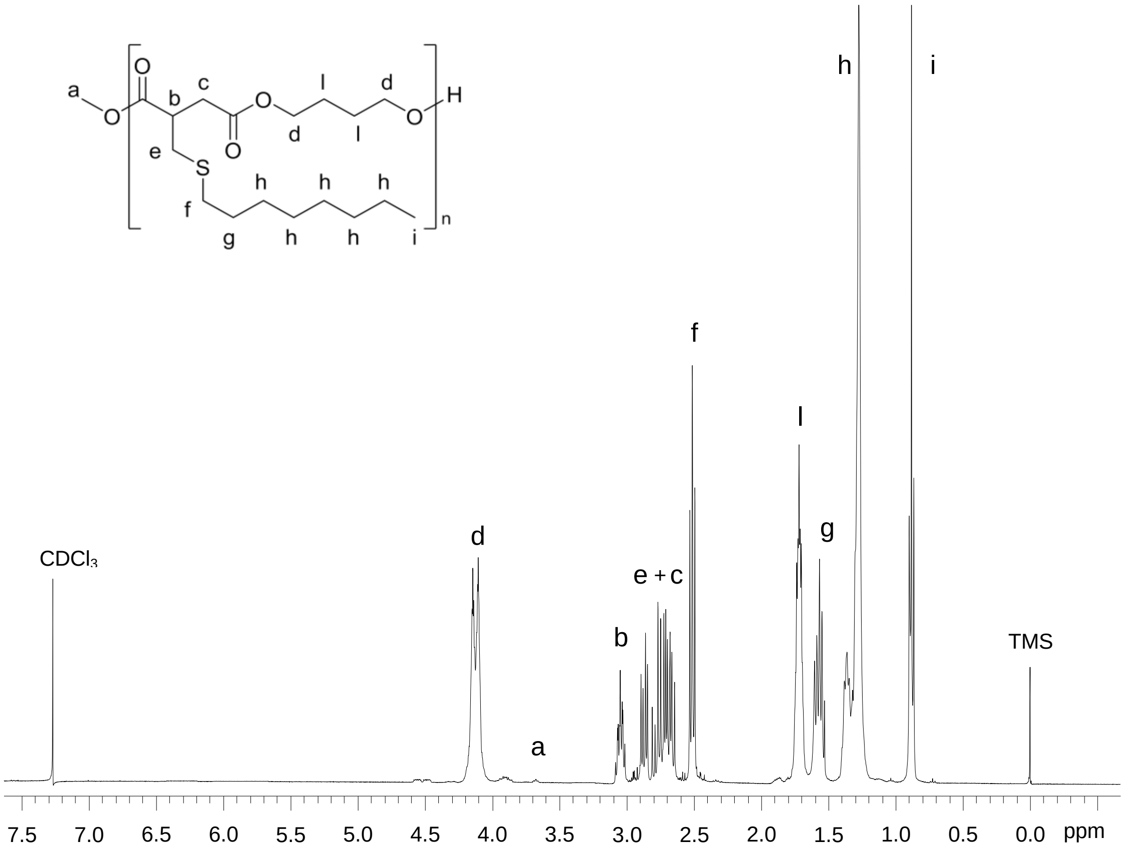

Figure 3.1. 6: ^{1}H-NMR spectrum of DOMS-BD.

The DSC thermograms showed that the polyesters are in the fully amorphous state, characterized by a low glass transition temperature (between -66 °C and -59 °C). As reported in Table 3.1. 1, DSC analyses revealed a certain correspondence between the molecular weight and the Tg value of the synthesized polyesters. Figure 3.1. 11 shows the 2nd heating DSC thermogram of optimized DOMS-BD (entry 7).

The thermal stability of DOMS-BD was analyzed by TGA and the thermogravimetric curve (Figure 3.1. 12) reveals that degradation occurs at the temperature (T_{onset}) of 364 °C.

The functionalization with thiols proves to be a powerful tool to obtain a thermo-stable system based on itaconic acid that allows the synthesis of high molecular weight polyesters. The lateral group introduced by thia-Michael addition reaction may provide antibacterial activity to DOMS-BD polyester in the attempt of mimic poly(ricinoleic acid)'s structure but, at the same time, it hinders the crystallization process interfering with the chain's organization. As a result, amorphous DOMS-BD polyesters are obtained as observed by DSC analyses. In addition, the aliphatic lateral group affects the glass transition temperature due to free volume increase; for this reason, the polyesters are characterized by glass transition temperature values similar to that of natural rubber (i.e. -67 °C)[122].

Table 3.1. 1: Polycondensation reaction conditions, weight average molecular weights, polydispersity indexes (PDI) and glass transition temperatures of DOMS-BD polyesters.

entry	nBD/nDOMS	catalyst (ppm)	Mw × 10^{-3} [a] (g mol^{-1})	PDI [b]	Tg [c] (°C)
1	1.05	250 TBT	12.0	2.4	-64
2	1.2	250 TBT	21.3	2.0	-64
3	1.5	250 TBT	80.9	2.6	-64
4	1.7	250 TBT	87.0	2.5	-63
5	2	250 TBT	107.5	2.5	-59
6	2	250 DBTO	8.7	2.2	-66
7	2	175 TBT	88.8	2.5	-63

[a] determined by GPC analysis. [b] determined as Mw/Mn. [c] determined by DSC, second heating scan at 10 °C min^{-1} after a cooling scan at 10 °C min^{-1}.

3.1.5 Synthesis of polyesters based on DOMS

The influence of the diol structure on the properties of the polyesters based on DOMS was studied using more rigid structures than 1,4-butanediol, such as 1,4-cyclohexanedimethanol 66% trans (CHDM), 1,4-cyclohexanediol 56% trans (CHD) and isosorbide (ISO), as shown in Scheme 3.1. 3. The polymers are named DOMS-CHDM, DOMS-CHD and DOMS-ISO, respectively.

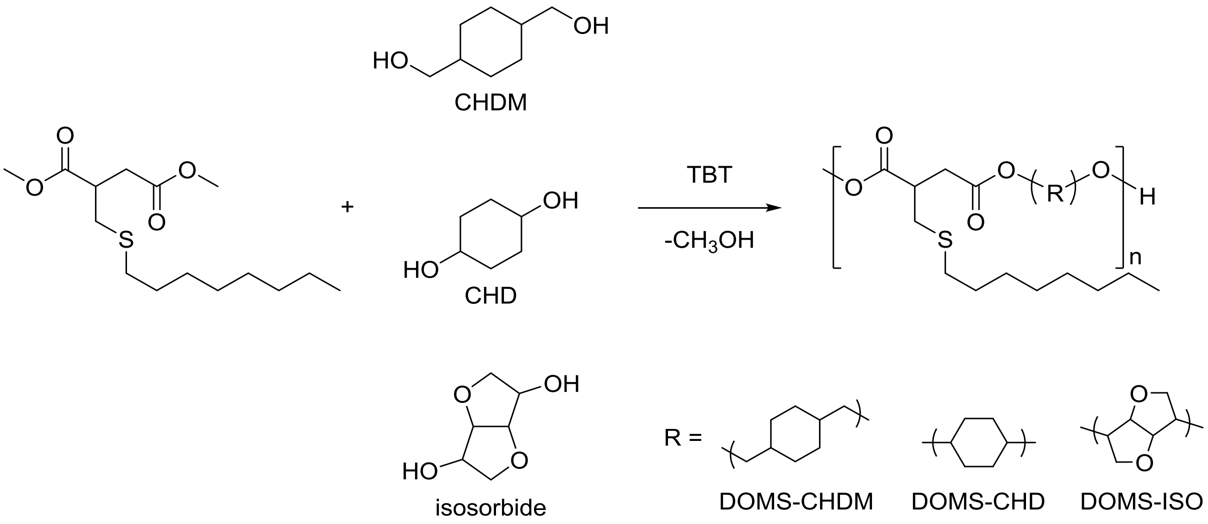

Scheme 3.1. 3: Synthesis of different itaconic-based polyesters by varying the diol type. From the top: 1,4-cyclohexanedimethanol (CHDM), 1,4-cyclohexanediol (CHD) and isosorbide.

According to the results obtained for DOMS-BD, the amount of TBT catalyst was maintained at 175 ppm for all the reactions, but parameters such as the feed ratio, the temperatures and reaction times of the two stages were tailored to monomers that have higher-boiling points and are less reactive with respect to BD. Using CHDM as diol, it was observed that the optimal molar ratio is 1.2, due to the low volatility of the diol since its boiling point is at 286 °C (see samples DOMS-CHDM 1 and DOMS-CHDM 2 in Table 3.1. 2) and on the basis of such consideration the following reactions were carried out. As proved by the sample DOMS-CHDM 3, the molecular weight of the material slightly increases (i.e. 35300 g mol^{-1}) when the temperature of the second stage is increased at 230 °C instead of 210 °C. The ^{1}H-NMR spectrum of DOMS-CHDM polyester is reported in Figure 3.1. 7.

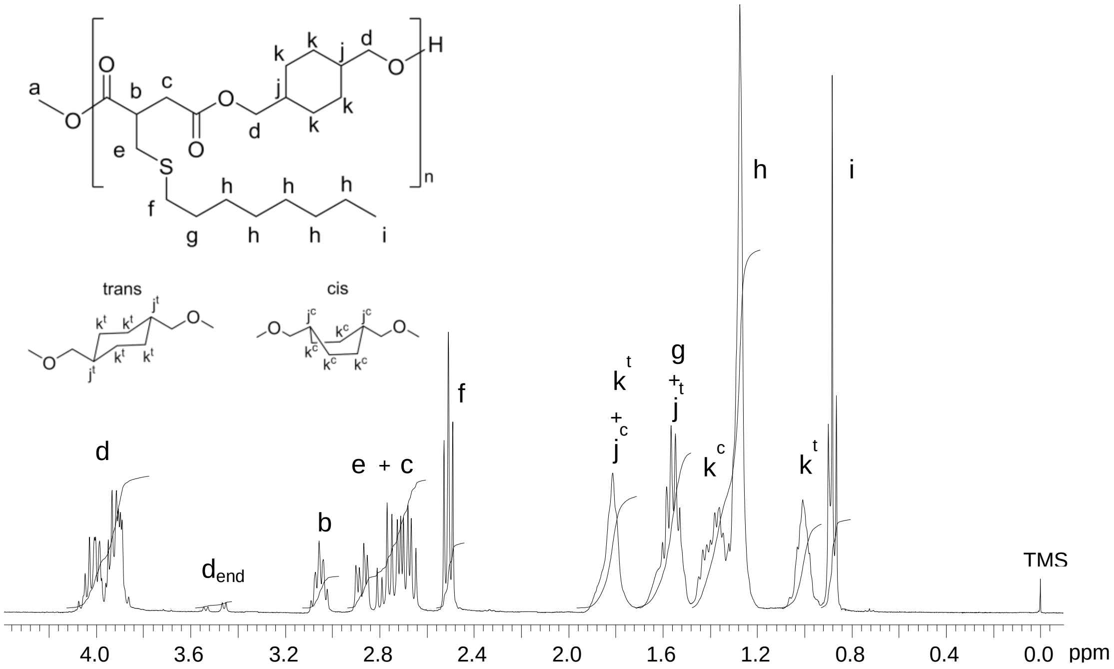

Figure 3.1. 7: ^{1}H-NMR spectrum of the polyester DOMS-CHDM obtained by polycondensation of dimethyl 2-((octylthio)methyl)succinate and 1,4-cyclohexanedimethanol.

Table 3.1. 2: Polycondensation reaction conditions, weight average molecular weights, polydispersity indexes and glass transition temperatures of polyesters of dimethyl 2-((octylthio)methyl)succinate with different diols.

sample	diol type	ndiol/nDOMS	T 1st stage (°C)	T 2nd stage (°C)	Mw × 10^{-3} [a] (g mol^{-1})	PDI [b]	Tg [c] (°C)
DOMS-CHDM 1	CHDM	2	200	210	17.3	2.6	-40
DOMS-CHDM 2	CHDM	1.2	200	210	31.8	2.0	-38
DOMS-CHDM 3	CHDM	1.2	200	230	35.3	2.2	-37
DOMS-CHD 1	CHD	1.2	200	210	21.1	2.2	-29
DOMS-CHD 2	CHD	1.2	200	230	31.1	2.4	-23
DOMS-ISO	isosorbide	1.2	200*	230*	28.7	2.4	8

[a] determined by GPC analysis. [b] determined as Mw/Mn. [c] determined by DSC, second heating scan at 10 °C min^{-1} after a cooling from the melt at 10 °C min^{-1}. *conducted by varying the stage time.

A more pronounced effect of the temperature of the second polymerization stage on the molecular weight was detected using CHD as diol. Table 3.1. 2 shows that in samples DOMS-CHD 1 and DOMS-CHD 2 the increment of the second stage temperature produces a growth of the molecular weight from 21100 to 31100 g mol^{-1}. The ^{1}H-NMR spectrum of the obtained polyester using CHD as diol is reported in Figure 3.1. 8.

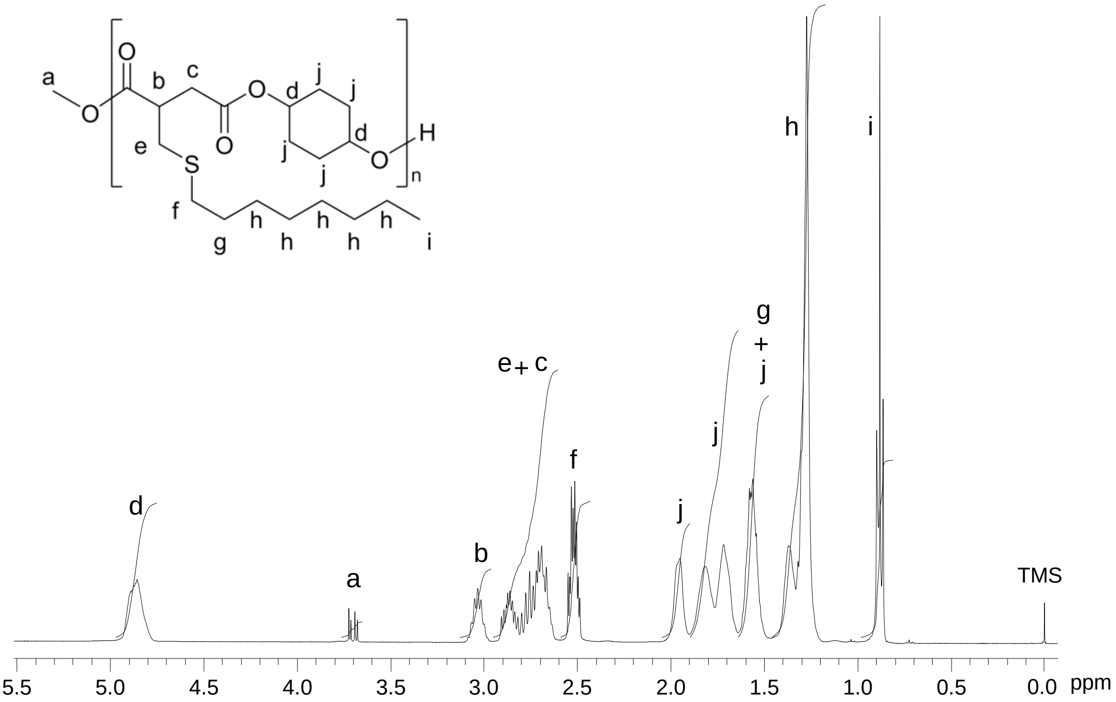

Figure 3.1. 8: ^{1}H-NMR spectrum of the polyester DOMS-CHD obtained by polycondensation of dimethyl 2-((octylthio)methyl)succinate and 1,4-cyclohexanediol.

Isosorbide is characterized by a low reactivity as reported in literature.[123] Therefore, while the first stage was maintained for 3 hours, the second stage was followed by subsequent sampling (4h, 5h, 6h, 8h) in order to monitor the molecular weight growth. Acceptable molecular weight (28700 g mol^{-1}) was achieved after 4 hours at 210 °C and 4 hours at 230 °C under vacuum. So, polyester DOMS-ISO, which ^{1}H-NMR spectrum is reported in Figure 3.1. 9, was obtained by extending reaction times.

DOMS proves to be reactive also with more rigid diols such as CHDM, CHD and isosorbide as demonstrated by the acceptable molecular weight obtained for all the polyesters.

DSC curves reported in Figure 3.1. 11, reveal that all the polyesters are fully amorphous, characterized by higher Tg values with respect to that of DOMS-BD. DOMS-CHDM presents Tg value ranging around -38 °C and DOMS-CHD around -25°C, depending on the molecular weight. The Tg value is also dependent of the cis/trans content of CHDM (66% trans) and CHD (56% trans) which is retained in polyesters structure and it is known that the Tg value increases with the increment of the trans content.[124] DOMS-ISO is characterized by a Tg of 8°C. Such remarkable increment of Tg is related to the diol rigidity. The aliphatic linear chain of the butanediol introduces high chain flexibility and determines very low values of Tg. Otherwise, the glass transition temperature increases in the presence of 6 members cycles: CHDM causes an increment of Tg of about 20 °C, whereas the higher rigidity of CHD increments Tg of about other 20 °C. A further increment of the Tg value is obtained using isosorbide that is constituted by two fused tetrahydrofuran cycles.[125] Therefore, by varying the chemical structure of the diol, it is possible to tailor the thermal properties of the polyesters. However, despite such remarkable increments, all the polyesters are in the fully amorphous state with Tg values below room temperature.

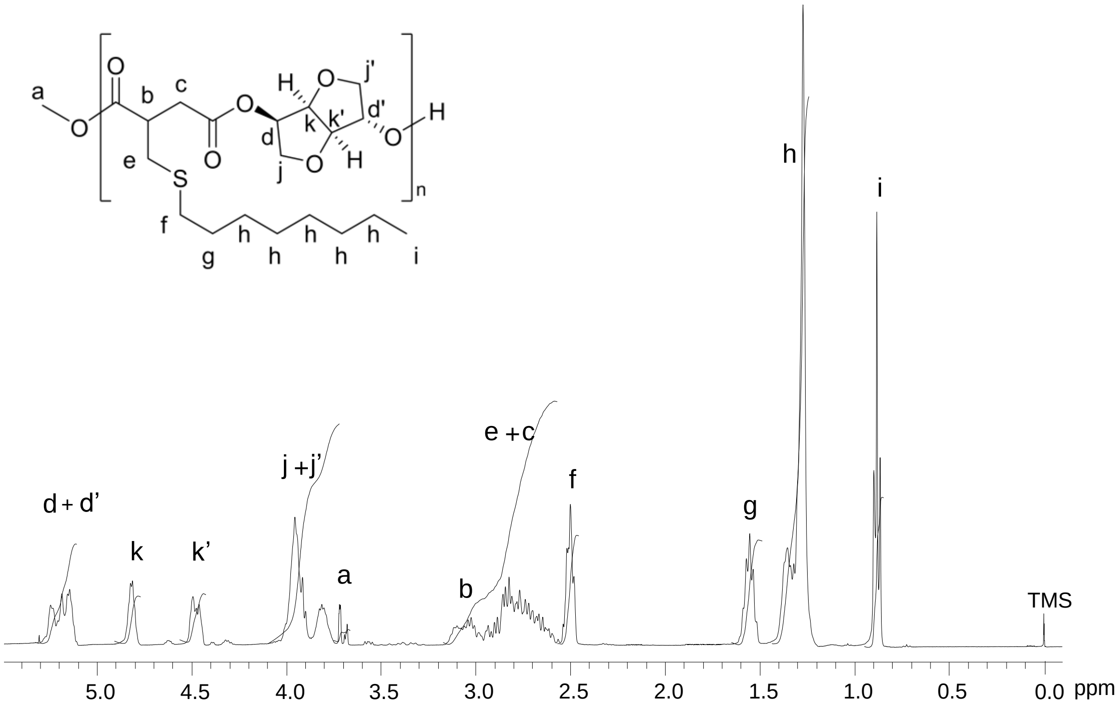

Figure 3.1. 9: ^{1}H-NMR spectrum of the polyester DOMS-ISO obtained by polycondensation of dimethyl 2-((octylthio)methyl)succinate and isosorbide.

The thermogravimetric curves reported in Figure 3.1. 12, show that the initial degradation occurs at temperatures (T_{onset}) higher than 340 °C for all the polymers. DOMS-CHD starts to degrade at 340 °C, DOMS-ISO degrades at 362 °C while DOMS-CHDM shows thermal resistance until 373 °C.

Since the synthesized polyesters exhibit an outstanding thermal stability, if blend mixed or inserted in copolymeric architectures, they might undergo thermo-processing such as extrusion and injection molding to produce films or other materials. In this case, it’s worth noting that blending or copolymerization are necessary requirements to obtain thermo-plastic goods since the polyesters exhibit Tg values below room temperature and they don't crystallize even if slow cooling are applied.

The polyesters can also produce thermosets if a small amount of dimethyl itaconate is inserted as co-unit in the polyester's structure. From preliminary studies, we demonstrated that in the same reaction conditions previously described and whatever the diol used, the polycondensation of DOMS with a 5/10% molar ratio of DMI allow obtain polyesters completely soluble and without crosslinking. In addition, the subsequent UV curing of the viscous prepolymers thus synthesized demonstrated to harden the polymers obtaining insoluble and infusible materials. Clearly, the present research requires additional investigations but from these preliminary studies it can be concluded that it's possible to obtain thermosets fully based on dimethyl itaconate.

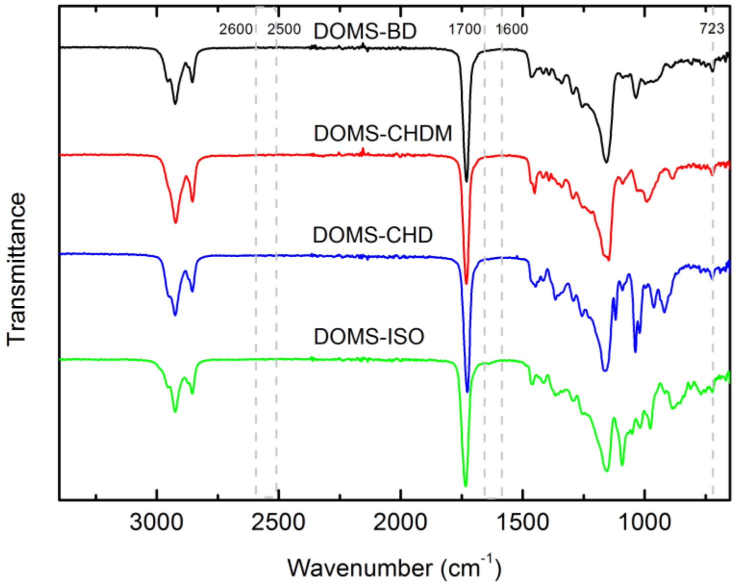

Figure 3.1. 10: FT-IR spectra of polyesters DOMS-BD, DOMS-CHDM, DOMS-CHD, DOMS-ISO.

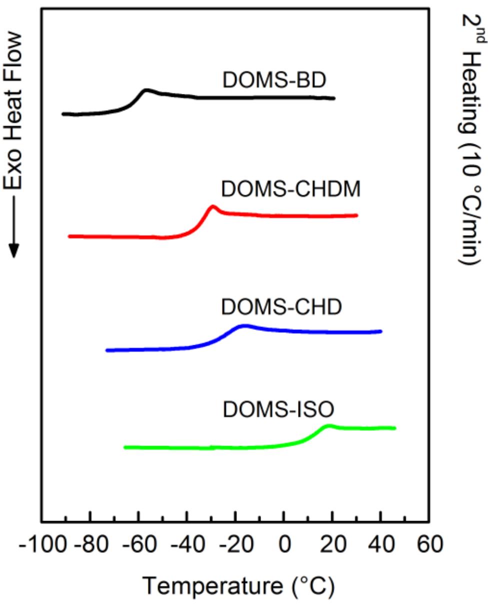

Figure 3.1. 11: Second heating curves of polyesters DOMS-BD, DOMS-CHDM, DOMS-CHD, DOMS-ISO at 10 °C min^{-1}. The curves have been normalized by the weight of the samples.

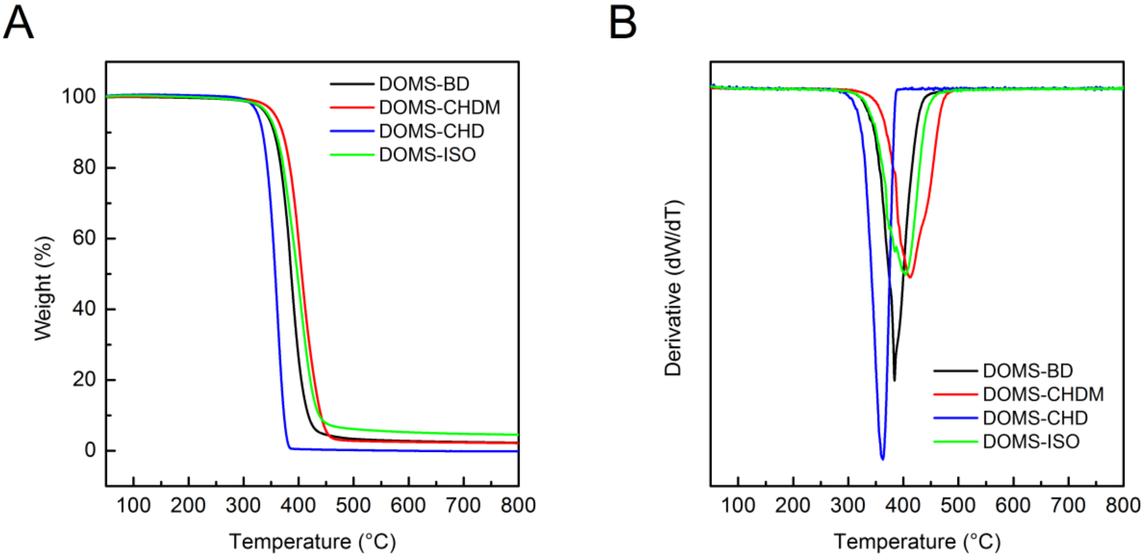

Figure 3.1. 12: TGA curves of polyesters DOMS-BD, DOMS-CHDM, DOMS-CHD, DOMS-ISO at 10 °C min^{-1} under N_2 atmosphere (**A**) and their derivatives (**B**).

3.1.6 Itaconic/furandicarboxylic-based copolymers

With the aim to design copolymeric architectures based on DOMS and improve the thermal properties of the homopolymer, the synthesis of copolymers with a rigid counterpart was studied. To ensure the bio-derivation, dimethyl 2,5-furandicarboxylate (DFDC) was selected as a diester comonomer and 1,3 propanediol as a diol (Scheme 3.1. 4).

Dimethyl 2,5-furandicarboxylate (DFDC) is the dimethyl ester of 2,5-furandicarboxylic acid (FDCA) which is one of the most relevant bio-based building blocks and the first candidate to replace aromatic terephthalic acid. The choice of dimethyl ester is dictated by the fact that acid moieties are responsible for the alkylthio group scission and the undesired crosslinking reactions during polycondensation.

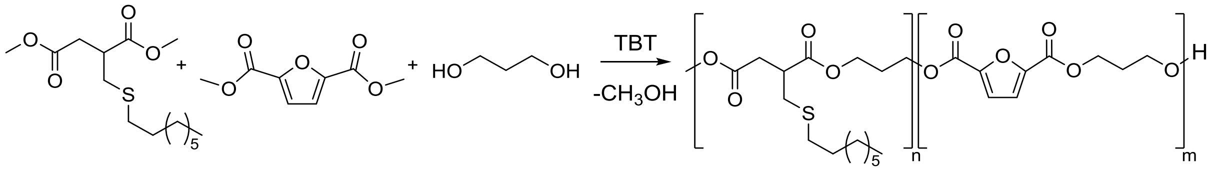

Scheme 3.1. 4: Synthesis of itaconic/furadicarboxylic-based copolymers.

Two different copolymers were synthesized by varying the molar ratio of DOMS and DFDC, considering that DFDC is the structure conferring rigidity: DOMS-DFDC 20/80 and 40/60 were selected as molar compositions as reported in Table 3.1. 3.

The synthetic parameters were adapted from the previously reported procedures. In particular, 175 ppm of TBT were used as a catalyst and the feed ratio of the diol to esters was set at 1.80 according to the literature on PPF synthesis.[126] The first stage was conducted at 180 °C for 1 hour and at 200 °C for the 2nd hour while in the second stage, which lasted 3 hours, the temperature was gradually raised from 200 °C to 230 °C and the pressure reduced to 10^{-1} mbar. The described conditions of reaction allowed DOMS-DFDC 20/80 to achieve a molecular weight of 33300 g mol^{-1} and DOMS-DFDC 40/60 of 26200 g mol^{-1}, as reported in Table 3.1. 3. The chemical structure of the synthesized copolymers was confirmed by ^{1}H-NMR analysis shown in Figure 3.1. 13. In Scheme 3.1. 5 the possible diads for DOMS-DFDC random copolymers are reported. The signals of the protons of the two monomers remain unvaried by the neighborhood. From right to left: 0.87 ppm ^{i}H, 1.26 ppm ^{h}H, 1.55 ^{g}H, 2.50 ppm ^{f}H, from 2.62 to 2.90 ^{e}H and ^{c}H, 3.04 ppm ^{b}H, 3.71 ^{a}H of DOMS monomer; 7.21 ppm ^{m}H of DFDC monomer. On the other hand, the signals of the protons of propanediol split depending on the neighborhood. The signals of propanediol linked from both sides to DOMS (DOMS-DOMS) occur at 2.11 ppm for ^{l}H and 4.42 for ^{d}H. The signals at 2.24 ppm and 4.48 ppm are assigned to the protons of propanediol linked from both sides to DFDC (DFDC-DFDC) labeled as ^{p}H and ^{n}H in Scheme 3.1. 5. When propanediol is linked from one side to one monomer and from the other side to the other (DOMS-DFDC), the system loses symmetry and multiple signals are recorded at 1.98 ppm and 4.22 ppm for ^{r}H and ^{q}H respectively.

The signals at 3.04 ppm (proton ^{b}H of DOMS-unit) and 7.21 ppm (proton ^{m}H of DFDC-unit) were chosen to determine the molar fractions of DOMS (F_{DOMS}) and DFDC (F_{DFDC}) units using the equations:

$$F_{DOMS} = \frac{I_b}{I_b + I_m/2} \tag{3.1. 1}$$

$$F_{DFDC} = \frac{I_m/2}{I_b + I_m/2} \tag{3.1. 2}$$

where I is the integration intensity of signals. The calculated values of the molar fraction are reported in Table 3.1. 3.

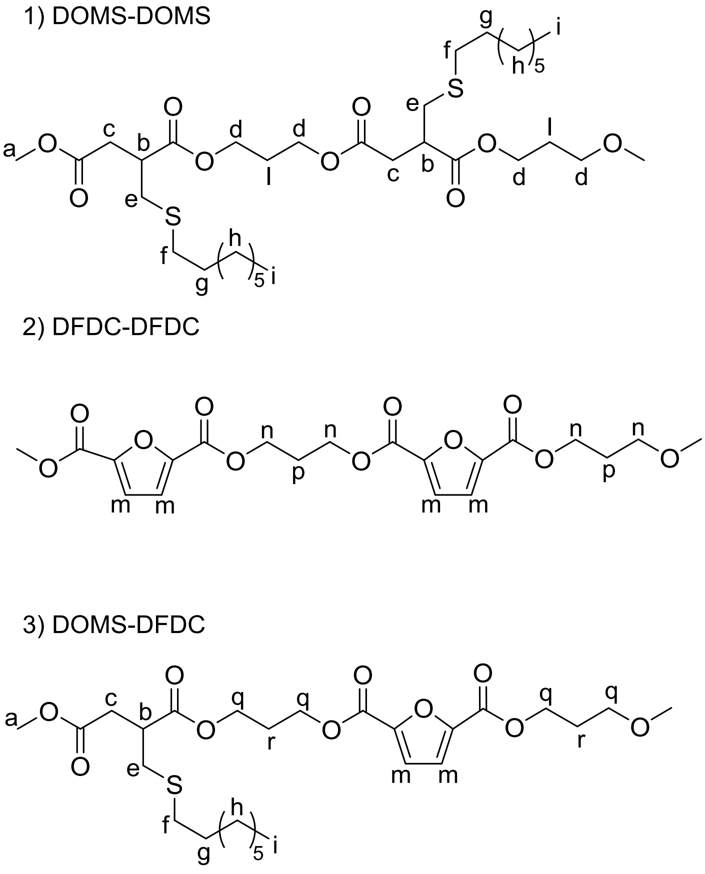
1) DOMS-DOMS

2) DFDC-DFDC

3) DOMS-DFDC

Scheme 3.1. 5: Diads present in DOMS-DFDC random copolymers.

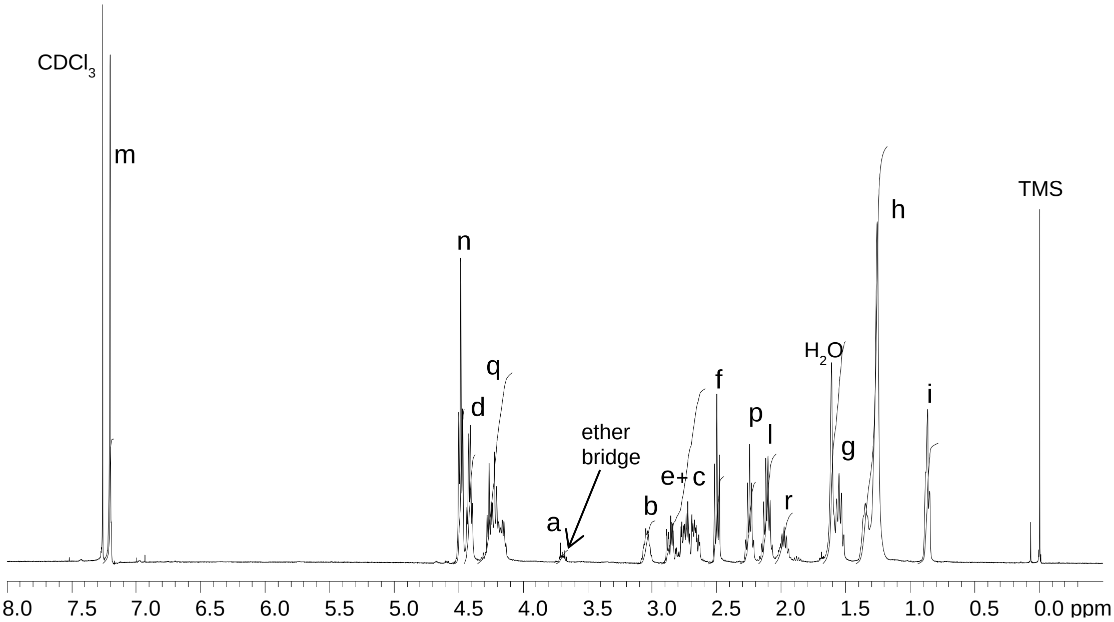

Figure 3.1. 13: ^{1}H-NMR spectrum of the copolymer DOMS-DFDC 40/60.

The DSC analyses reported in Figure 3.1. 14 reveal that the copolymers are fully amorphous, characterized by a Tg value which is a function of the molar composition. The copolymer DOMS-DFDC 20/80 presents a Tg value of 8 °C while the copolymer 40/60 of -19 °C. This trend was expected since DOMS-based polyesters are characterized by low Tg values and PPF is characterized by a Tg value of 54 °C. As reported by Vannini *et al.*[126] PPF is unable to crystallize during the cooling scan at 10 °C per min, but it eventually can crystallize by annealing.

The thermogravimetric curves reported in Figure 3.1. 15, show that the initial degradation occurs at temperatures (T_{onset}) higher than 365 °C for all the copolymers. DOMS/DFDC 20/80 starts to degrade at 370 °C and DOMS/DFDC 40/60 degrades at 365 °C. All the copolymers synthesized present outstanding stability that allows subjecting them to processing methods.

Table 3.1. 3: Molar fractions of DFDC units, weight average molecular weights, polydispersity indexes and glass transition temperatures of copolymers DOMS-DFDC.

sample	F_{DFDC} [a]	Mw × 10^{-3} [b] (g mol^{-1})	PDI [c]	Tg [d] (°C)
DOMS-DFDC 20/80	0.81	33.3	2.0	8
DOMS-DFDC 40/60	0.59	26.2	1.9	-19

[a] determined by ^{1}H-NMR analysis using Equation 3.1. 2. [b] determined by GPC analysis. [c] determined as Mw/Mn.
[d] determined by DSC, second heating scan at 10 °C min^{-1} after cooling from the melt at 10 °C min^{-1}.

The synthesized copolymers powders were thermo-pressed between two Teflon sheets to obtain films. The powder was heated at 120 °C for 4 minutes under pressure and then the film was maintained between the Teflon sheets for a day before opening them. Figure 3.1. 16 shows DOMS-DFDC 40/60 copolymer film. The DSC 1st heating scan on copolymers films showed a broad endothermic peak indicating that during the slow cooling the copolymers reach a certain state of order. Therefore, despite the Tg value of both copolymers is below room temperature, the films were successfully obtained because of that chain reorganization process.

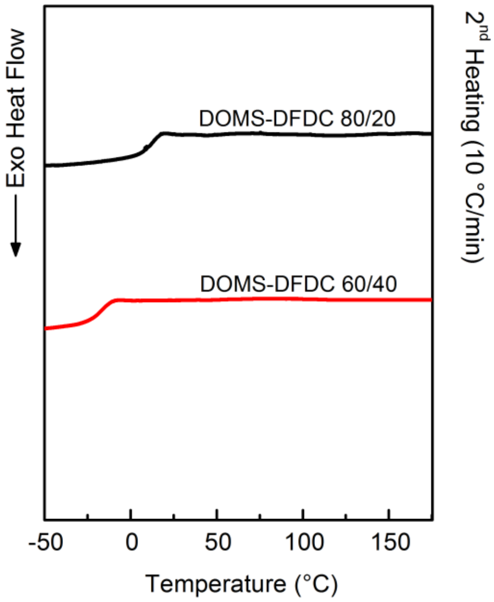

Figure 3.1. 14: Second heating curves of copolymers DOMS-DFDC 20/80 and DOMS-DFDC 40/60 at 10 °C min^{-1}. The curves have been normalized by the weight of the samples.

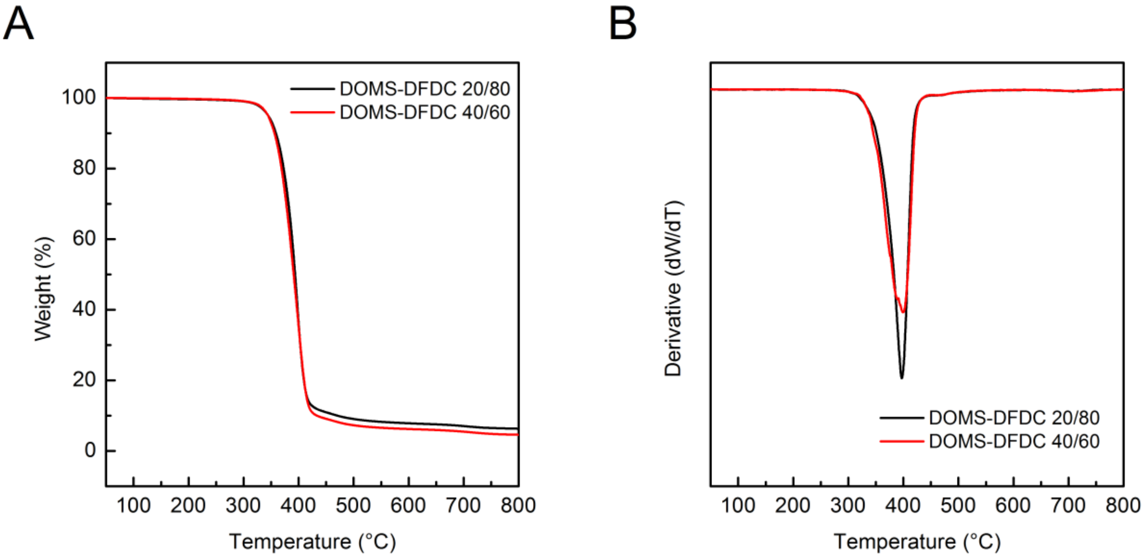

Figure 3.1. 15: TGA curves of copolymers DOMS-DFDC 20/80 and DOMS-DFDC 40/60 at 10 °C min^{-1} under N_2 atmosphere (**A**) and their derivatives (**B**).

Figure 3.1. 16: DOMS-DFDC 40/60 copolymer film.

3.1.7 Antimicrobial test

In order to ascribe antimicrobial activity to the long lateral chain of the thio-functionalized polyesters, the antimicrobial tests were performed on poly(butylene succinate) (PBS), poly(butylene 2-methylsuccinate) (PBMS) and DOMS-BD polyesters whose chemical structures are reported in Figure 3.1. 17. PBS and PBMS were synthesized using TBT as the catalyst, starting from dimethyl succinate and dimethyl 2-methyl succinate monomers respectively. 2-methyl succinate was obtained by hydrogenation of dimethyl itaconate. As shown in Figure 3.1. 17, the chemical structure of the synthesized polyesters differs only for the lateral chain.

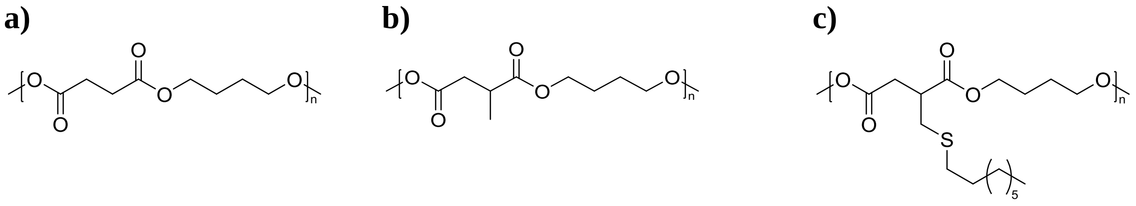

poly(butylene succinate)
PBS

poly(butylene 2-methylsuccinate)
PBMS

DOMS-BD

Figure 3.1. 17: Chemical structure of **a)** poly(butylene succinate) -PBS-, **b)** poly(butylene 2-methylsuccinate) -PBMS- and **c)** DOMS-BD.

The syntheses of the investigated polyesters were governed in order to obtain similar molecular weights which range around 16000 g mol^{-1}, as shown in Table 3.1. 4. Only for DOMS-BD polyester, two samples at different molecular weights, reported as l-M$_w$ and h-M$_w$ in Table 3.1. 4 for the lower and higher molecular weight respectively, were tested. The sample l-M$_w$ is comparable to the molecular weight of PBS and PBMS while the sample h-M$_w$ provides information about the influence of the molecular weight on antimicrobial activity.

Table 3.1. 4: Molecular weight of PBS, PBMS and DOMS-BD polyesters.

sample	Mw × 10^{-3} [a] (g mol^{-1})	PDI [b]
PBS	15.0	1.8
PBMS	20.0	2.2
DOMS-BD l-Mw	12.0	2.4
DOMS-BD h-Mw	87.0	2.5

[a] determined by GPC analysis. [b] determined as Mw/Mn.

Staphylococcus aureus, representing a Gram-positive bacterium, was used as target strain. To estimate the number of viable bacterial cells that form the cell suspension added to the samples, the counting with colony-forming units was performed at time t_0. The samples in contact with the cell suspension were incubated for 24 hours before the evaluation of the number of viable bacterial cells *via* plate counts reported as Log(CFU/ml) at t_{24}. A control sample containing just the cell suspension was submitted to the same experimental condition to ensure the viability of bacterial cells during incubation. The control sample was assessed as 100% cells viability.

Table 3.1. 5 and Figure 3.1. 18 report the antimicrobial tests performed on the samples reported in Table 3.1. 4 using *Staphylococcus aureus* as target strain.

Table 3.1. 5: Antimicrobial activity tests on PBS, PBMS, DOMS-BD l-Mw, DOMS-BD h-Mw polyesters using *Staphylococcus aureus* as target strain. The data are reported as Log of colony forming unit (CFU)/ml and the % of inhibition is calculated as difference with respect to control sample.

	Staphylococcus aureus					
	t_0	t_{24}				
	strain	control	PBS	PBMS	DOMS-BD l-Mw	DOMS-BD h-Mw
Log (CFU/ml)	5.86 ± 0.04	5.95 ± 0.04	5.52 ± 0.07	5.36 ± 0.05	4.79 ± 0.09	5.34 ± 0.06
inh %			7.3 ± 1.0	9.9 ± 0.9	19.5 ± 1.4	10.2 ± 1.0

While PBS and PBMS exhibited a negligible inhibition against *S. aureus* (7.3% and 9.9%, i.e. bacterial cells reduction from 9.0×10^5 to 3.1×10^5 and 2.3×10^5 CFU/ml respectively), DOMS-BD l-Mw caused a cell inhibition of about 20%, i.e. reduction to 6.8×10^4 CFU/ml. Although requiring further studies and optimization, these results undoubtedly demonstrate that the lateral chain can provide a biocidal activity to the final polyester. Totaro *et al.*[102] reported that poly(ricinoleic acid) express strong antimicrobial activity against *S. aureus* due to the long lateral chain able to perforate the inner membrane of a Gram-positive bacterium. A similar mechanism of inhibition can be hypnotized for DOMS-BD due to the comparable chemical structure.

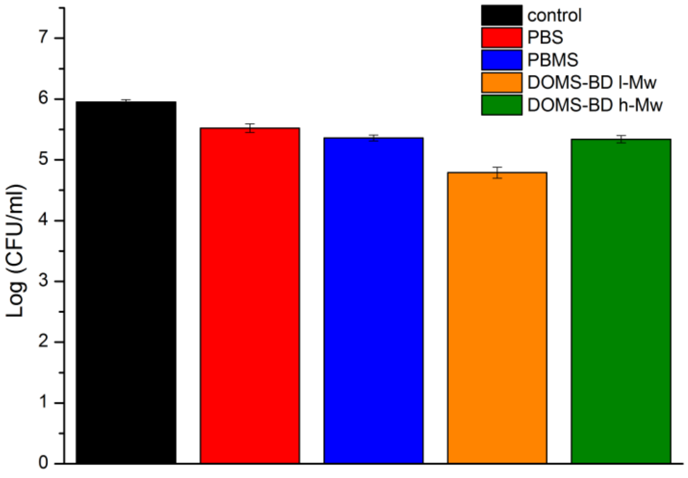

Figure 3.1. 18: Antimicrobial activity tests against *S. aureus* on PBS, PBMS, DOMS-BD l-Mw and DOMS-BD h-Mw reported as Log of colony forming unit (CFU)/ml.

Regarding the influence of the molecular weight, DOMS-BD h-Mw exhibited an inhibition against *S. aureus* of 10.2%, i.e. bacterial cells reduction from $9{,}0\times10^5$ to $2{,}2\times10^5$. This result suggests that the molecular weight of the polymer, which is strictly related to the viscosity, greatly affect the microorganism inhibition capacity of the polymer itself. The viscosity of the polymer is probably related to the dispersion capacity in the cell suspension and hence it results that the contact area is a critical parameter in antimicrobial test.

3.1.8 Conclusions

We successfully proved that the functionalization of dimethyl itaconate allows obtaining a thermo-stable building block that can undergo polycondensation under classical conditions of reaction. The polycondensation optimization was studied using 1,4-butanediol as counterpart and itaconate-based polyesters without crosslinking were obtained. GPC analysis revealed polyesters with a molecular weight up to 107500 g mol^{-1} and homogeneous polydispersity proving the linear structure and the absence of crosslinking. The synthesized DOMS-BD polyesters are completely amorphous and characterized by a Tg value of -60 °C. We also demonstrated that 1,4-cyclohexanedimethanol, 1,4-cyclohexanediol, and isosorbide can be used as diols to obtain different polymeric structures at high molecular weight, high thermal stability and Tg values that vary according to the rigidity of the chain. So, the Tg value of the dimethyl itaconate-based polyesters can be tuned in a wide range of temperatures, from -60 to 8 °C. We also proved that the thio-functionalized itaconic based monomer can be used as co-unit in copolymers with dimethyl 2,5-furandicarboxylate obtaining thermo-processable copolymers.

Finally, we proved that the insertion of a long lateral chain on the polymer backbone allows the polymer to express biocidal activity against Gram-positive bacteria such as *Staphylococcus aureus.*

Therefore, the approach hereby developed will allow the constitution of a platform of functional monomers based on itaconic acid that will be employed for the fabrication of thermosets and thermostable polymeric architectures suitable, as for example, in packaging and antimicrobial applications.

3.1.9 Experimental

3.1.9.1 Materials

Dimethyl itaconate, 1-octanethiol, and 1-butanethiol were purchased from Tokyo Chemical Industry Co. with purities of >98%, >99% and >97% respectively and used as received. K_2CO_3 (99% purity), 1,4-butanediol (99%), 1,4-cyclohexanediol (99%, 56% trans), 1,4-cyclohexanedimethanol (99%, 66% trans), isosorbide (98%), 1,3-propanediol (98%), dimethyl succinate (98%), dibutyltin (IV) oxide -DBTO- (98%), titanium (IV) butoxide -TBT- (97%), octanoic acid (>98%), p-toluenesulfonic acid monohydrate (99%) and Pd/C (5 wt% loading on dry basis) were purchased from Sigma-Aldrich and used without further purification treatments. Dimethyl 2,5-furandicarboxylate was supplied by Tetrapak.

3.1.9.2 Synthesis of dimethyl 2-((octylthio)methyl)succinate

Dimethyl itaconate (10.00 g, 63.31 mmol), 1-octanethiol (9.71 g, 66.48 mmol), K_2CO_3 (3.00 g, 30wt% to dimethyl itaconate) and acetone (50 mL) were introduced in a round bottom flask equipped with a magnetic stirrer. The mixture was stirred for 24 hours at room temperature. After the reaction, K_2CO_3 was removed by filtration and acetone was removed under reduced pressure to obtain the product in 99% yield.

^{1}H-NMR (400 MHz, $CDCl_3$, δ): 0.82 (t, J=7.03 Hz, 3H, C^iH_3), 1.17-1.35 (m, 10H, C^hH_2), 1.47-1.55 (m, 2H, C^gH_2), 2.45 (t, J=7.42 Hz, 2H, C^fH_2), 2.61 (dd, J_1=8.01 Hz, J_2=13.47 Hz, 1H, C^eH), 2.66 (dd, J_1=5.66 Hz, J_2=16.79 Hz, 1H, C^cH), 2.72 (dd, J_1=8.20 Hz, J_2=16.79 Hz, 1H, C^cH), 2.83 (dd, J_1=5.85 Hz, J_2=13.47 Hz ,1H, C^eH), 2.97-3.04 (m, 1H, C^bH), 3.63 (s, 3H, C^dH_3), 3.66 (s, 3H, C^aH_3).

3.1.9.3 Stability tests

Dimethyl 2-((octylthio)methyl)succinate was introduced into a closed vial equipped with a magnetic stirrer and heated at 200 °C for 5 hours. The same procedure was adopted in presence of 7% mol to DOMS of titanium (IV) butoxide, octanoic acid or p-toluenesulfonic acid monohydrate.

3.1.9.4 Synthesis of polyesters

Dimethyl 2-((octylthio)methyl)succinate, the different diol and TBT were introduced into a 500 ml glass reactor bottle equipped with a mechanic stirrer and connected to nitrogen flow. The mixture was heated under nitrogen atmosphere at 200 °C until the complete elimination of methanol. After this first stage, the mixture was subjected to a high vacuum-temperature ramp. During the second stage, the temperature was raised in a range of 210-230 °C and the final pressure was 0.1 mbar.

DOMS-BD ^{1}H-NMR (400 MHz, $CDCl_3$, δ): 0.88 (t, J=7.03 Hz, 3H, $C^{i}H_3$), 1.21-1.41 (m, 10H, $C^{h}H_2$), 1.52-1.60 (m, 2H, $C^{g}H_2$), 1.67-1.76 (m, 4H, $C^{l}H_2$), 2.50 (t, J=7.42 Hz, 2H, $C^{f}H_2$), 2.66 (dd, J_1=8.01 Hz, J_2=13.47 Hz, 1H, $C^{e}H$), 2.70 (dd, J_1=5.66 Hz, J_2=16.79 Hz, 1H, $C^{c}H$), 2.77 (dd, J_1=8.20 Hz, J_2=16.79 Hz, 1H, $C^{c}H$), 2.86 (dd, J_1=5.85 Hz, J_2=13.47 Hz ,1H, $C^{e}H$), 3.01-3.08 (m, 1H, $C^{b}H$), 3.67 (s, 3H, $COC^{a}H_3$), 4.04-4.21 (m, 4H, $C^{d}H_2$).

DOMS-CHDM ^{1}H-NMR (400 MHz, $CDCl_3$, δ): 0.88 (t, J=7.03 Hz, 3H, $C^{i}H_3$), 1.01 (m, 4H, $C^{k\_trans}H_2$), 1.21-1.45 (m, 10H, $C^{h}H_2$; 8H, $C^{k\_cis}H_2$), 1.50-1.59 (m, 2H, $C^{g}H_2$; 2H, $C^{j\_trans}H$), 1.81 (m, 4H, $C^{k\_trans}H_2$; 2H, $C^{j\_cis}H$), 2.51 (t, J=7.42 Hz, 2H, $C^{f}H_2$), 2.67 (dd, J_1=8.01 Hz, J_2=13.47 Hz, 1H, $C^{e}H$), 2.69 (dd, J_1=5.66 Hz, J_2=16.79 Hz, 1H, $C^{c}H$), 2.78 (dd, J_1=8.20 Hz, J_2=16.79 Hz, 1H, $C^{c}H$), 2.87 (dd, J_1=5.85 Hz, J_2=13.47 Hz ,1H, $C^{e}H$), 3.01-3.08 (m, 1H, $C^{b}H$), 3.46, 3.54 (d, 2H, $C^{d}H_2OH$ end group), 3.86-4.08 (m, 4H, $C^{d\_trans}H_2$; 4H, $C^{d\_cis}H_2$).

DOMS-CHD ^{1}H-NMR (400 MHz, $CDCl_3$, δ): 0.88 (t, J=7.03 Hz, 3H, $C^{i}H_3$), 1.21-1.43 (m, 10H, $C^{h}H_2$), 1.50-1.60, 1.72, 1.82, 1.95 (m, 2H, $C^{g}H_2$; 8H, $C^{j\_trans}H_2$; 8H, $C^{j\_cis}H_2$), 2.48-2.56 (m, 2H, $C^{f}H_2$), 2.64-2.89 (m, 2H, $C^{c}H_2$; 2H, $C^{e}H_2$), 2.98-3.08 (m, 1H, $C^{b}H$), 3.69, 3.68, 3.71, 3.72, (s, 3H, $COC^{a}H_3$), 4.86 (m, 2H, $C^{d\_trans}H$; 2H, $C^{d\_cis}H$).

DOMS-ISO ^{1}H-NMR (400 MHz, $CDCl_3$, δ): 0.88 (t, J=7.03 Hz, 3H, $C^{i}H_3$), 1.21-1.43 (m, 10H, $C^{h}H_2$), 1.51-1.58 (m, 2H, $C^{g}H_2$), 2.50-2.55 (m, 2H, $C^{f}H_2$), 2.55-2.95 (m, 2H, $C^{c}H_2$; 2H, $C^{e}H_2$), 3.00-3.15 (m, 1H, $C^{b}H$), 3.67-3.73 (m, 3H, $COC^{a}H_3$), 3.75-3.96 (m, 2H, $C^{j}H_2$; 2H, $C^{j'}H_2$), 4.43-4.53 (m, 1H, $C^{k'}H$), 4.77-4.86 (m, 1H, $C^{k}H$), 5.10-5.29 (m, 1H, $C^{d}H$; 1H, $C^{d'}H$).

3.1.9.5 Synthesis of itaconic/furandicarboxylic-based copolymers

Dimethyl 2,5-furandicarboxilate (15.0 g, 0.08146 mol), DOMS (in different amount depending of the desired composition), 1,3-propanediol (18.60 g, 0.2444 mol) and 175 ppm of TBT were introduced into a 500 ml glass reactor bottle equipped with a mechanic stirrer and connected to nitrogen flow. The polycondensation was performed in two stages. In the first stage, the mixture was heated under nitrogen atmosphere at 180 °C for 1 hour and in the 2nd hour the temperature was increased until 200 °C. In the second stage, the pressure was slowly reduced to 0.1 mbar while the temperature was gradually increased up to 230 °C during 3 hours.

3.1.9.6 Synthesis of dimethyl 2-methyl succinate

The reaction was performed in 500 mL, 3 necks round-bottom flask equipped with a magnetic stirrer, hydrogen inlet, thermometer and reflux column. Dimethyl itaconate (10.00 g, 63.31 mmol), cloridric acid (3 mL), methanol (100 mL) and Pd/C (0.70 g) were introduced in the flask under an inert atmosphere. Hydrogen was bubbled in the mixture replacing the inert atmosphere. The mixture was stirred for 5 hours at 45 °C. After the reaction, the catalyst was filtered and recycled on a Celite pad. Methanol was removed under reduced pressure; the product was solubilized in 75 ml of ethyl acetate and washed twice with deionized water (100 ml). The organic phase was collected, anhydrified with $MgSO_4$ and filtered. Ethyl acetate was removed under reduced pressure to obtain a light yellow dense liquid with a yield >80%.

^{1}H-NMR (400 MHz, $CDCl_3$, δ): 1.21 (d, J=7.03, 3H, CH_3-CH), 2.36 (dd, J_1=6.05 Hz, J_2=16.60 Hz, 1H, CH_2), 2.70 (dd, J_1=8.01 Hz, J_2=16.60 Hz, 1H, CH_2), 2.86-2.95 (m, 1H, CH-CH_3), 3.67 (s, 3H, CH_3COO), 3.76 (s, 3H, CH_3COO).

3.1.9.7 Synthesis of poly(butylene succinate) and poly(buthylene 2-methylsuccinate)

The dimethyl ester (10.00 g), 1,4 butanediol (1.2 equivalent) and 175 ppm of TBT were introduced into a glass round bottom tube equipped with a magnetic stirrer and connected to nitrogen flow. The mixture was heated under nitrogen atmosphere at 190 °C for 2 hours and 30 minutes. After this first stage, the mixture was subjected to a high vacuum ramp. During the second stage, the temperature was maintained 190 °C and the final pressure was 0.1 mbar. For dimethyl succinate the second stage lasted 1 hour while for dimethyl 2-methyl succinate 2 hours. The molecular weight of the polyester was monitored by GPC analysis.

3.1.9.8 Characterization

^{1}H-NMR spectra were recorded at room temperature on samples dissolved in $CDCl_3$ using a Varian Mercury 400 spectrometer operating at 400 MHz. Chemical shifts (δ) are reported in part per million with reference to chloroform solvent ($CHCl_3$).

Gel permeation chromatography (GPC) measurements were performed by a HP 1100 Series equipped with a PL gel 5 μm Minimixed-C column. The instrument, provided with a Refractive Index and UV detectors, worked using chloroform as eluent. Polymer samples were dissolved in chloroform (at a concentration of 0.10 %w/V) and a calibration plot was constructed with polystyrene standards.

The thermal behavior of the samples was studied by means of a Perkin-Elmer DSC7 equipped with a liquid sub-ambient accessory, for experiments at low temperature. The instrument was calibrated using high purity standards and all the measurements were performed under nitrogen flow using samples masses of approximately 5 mg. The samples were heated from 25 °C to 200 °C at 20 °C min^{-1} and held at high temperature for 2 min to erase their previous thermal history. Then they were cooled to -150 °C at 10 °C min^{-1} and finally heated to 200 °C at 10 °C min^{-1}. The glass transition temperature (Tg) was taken at the midpoint of the heat capacity increment during the 2nd scan.

The thermogravimetric analyses (TGA) were performed using a Perkin-Elmer TGA4000 under nitrogen atmosphere (gas flow 40 mL min^{-1}) at 10°C min^{-1} heating rate from 40 to 800 °C. For each sample, the onset degradation temperature (Tonset) was calculated as the intercept of the horizontal zero-line of the curve with the tangent drawn at the inflection point of the decomposition step.

Mass spectra were recorded on a Thermos DSQ GCMS.

Attenuated total reflection infrared (ATR-IR) spectra were recorded on a Di/ZnSe plate by a Perkin-Elmer Spectrum One FT-IR spectrometer.

3.1.9.9 Film preparation

The synthesized DOMS-DFDC copolymers were grinded using an Ika M20 Mill, Staufen, Germany. Resulting powders were dried at 60 °C for 24 hours. The films were obtained using a hydraulic thermo-press Carver, Wabash, Indiana, USA. Dried powder was thermo-moulded between two Teflon sheets at 120 °C for 2 min at 10 bar and 2 min at 100 bar. The film was maintained between the Teflon sheets for a day before opening them.

3.1.9.10 Antimicrobial test

Staphylococcus aureus was used as target strains. The microorganism was grown in nutrient broth for 24 hours at 37 °C under stirring. The culture obtained was centrifuged at 6000 rpm for 10 minutes. The harvested cells were washed with a saline buffer and suspended in the same buffer. The suspension was diluted of 4 orders of magnitude in order to obtain a cell suspension of about 10^5 Colony Forming Unit (CFU)/ml.

200 mg of each polymer sample were weighted in a glass vials and 300 μL of the cell suspension previously prepared were added. Two replicates for each sample were prepared in order to ensure reproducibility. The vials were placed in a lab shaker at 100 rpm at room temperature. After 24 hours of incubation, 100 μL of cell suspension was sampled and used for the evaluation of the concentration of viable bacterial cells *via* plate counts. On agar plates (Plate Count Agar) were seeded drops of 10 μL at a concentration of 10^{-3}, 10^{-4}, 10^{-5} and 10^{-6}. The plates were maintained at 37 °C for 24 hours to promote cells growth and after incubation the number of colonies was counted.

3.2 Fully bio-based aromatic polyesters derived from vanillic acid and ω-pentadecalactone

3.2.1 Introduction

In polymer science, aromatic building blocks are particularly attractive since the insertion of rigid units along the macromolecular chain can impart peculiar features to the material as high thermal stability, good processability, good mechanical performances and barrier properties useful for applications in different fields, as it happens for PET.

In order to move towards a sustainable model of development, several molecules extracted from biomass have been identified as potential substitutes of terephthalic acid as for example 2,5-furandicarboxylic acid (FDCA). However, a crucial step to ensure sustainability requires a careful evaluation of the availability of the target molecule in biomass, chemical characteristics and composition variability of the selected biomass, environmental impact and costs of the extraction technology, impact of the purification process necessary for further steps of polymerization, etc. The complexity of the problem has been addressed by current European projects, such as NoAW [127] and AgriMax [128], which aim at developing innovative and sustainable routes to select and extract these molecules from agricultural residues and agro-industrial by-products. In NoAW project the attention has been focused on vanillic acid and its possible extraction from grape pomaces, which are residual of the wine production. Despite it has been demonstrated that in the residual of the winery industry the presence of vanillic acid is low and its separation from a complex mixture of polyphenols was not achieved, the efforts made at European level fit with the scientific ferment around such aromatic building block which can be exploited in polymer science.

Literature reports that bio-based vanillic acid can be obtained from vegetables, such as basil, thyme and oregano. Vanillic acid can also be obtained from ferulic acid, whose extraction from natural feedstocks (such as wheat, sugar beet and rice by-products) is under development as a green, efficient and cheap synthetic way [129,130] and whose bioconversion to vanillic acid appears industrially feasible.[131,132] Moreover, vanillic acid can be prepared from vanillin, a biophenol relatively abundant in *Vanilla planifolia* orchid green pods, even if today the majority of the commercially available vanillin is synthesized from petroleum-derived precursors. However, it is expected that in a near future the ever-increasing demand for natural products will move the production of vanillin towards sustainable pathways.[133]

Vanillic acid can be exploited to obtain a bio-based aromatic polyester named poly(ethylene vanillate) (PEV) and the research group to which I belong already worked on the optimization of the synthetic procedure.[134,135] The great interest on PEV is motivated by its similarity to commercial poly(ethylene terephthalate) (PET): both polyesters present a *para*-substituted aromatic ring and show similar thermal transitions. PEV is characterized by a glass transition temperature (Tg) of 75 °C and melting temperature (Tm) of 264 °C [134] similarly to PET characterized by Tg = 78 °C and Tm = 252 °C.[136] However, PEV presents a notable high crystallinity that makes the material very brittle and difficult to process. The copolymerization of vanillic acid with flexible counterparts is a smart approach to moderate the brittleness of the material and to promote processability. The present work reports the use of a bio-based aliphatic comonomer such as ω-pentadecalactone (PDL), able to enhance the flexibility of PEV. PDL, although currently produced from petrochemical sources, can also be extracted from ambrette seed oil and roots of *Angelica archangelica* and it's known especially by the fragrance industry.[137,138] Moreover, macrocyclic lactones as PDL can be synthesized from inexpensive and naturally sourced ω-hydroxy fatty acids using either chemical or enzymatic routes.[139,140,141,142]

As matter of fact, the presence of vanillic acid in agro-waste or the possibility of obtaining it starting from bio-based vanillin or ferulic acid can define a new value chain that starts from biomass residuals to produce new aromatic building blocks and new materials, in this case aromatic PET-like polyesters.

3.2.2 Synthesis of poly(ethylene vanillate), poly(ω-pentadecalactone) and copolymers

The synthetic procedure here proposed was adapted from a previous work [134] and it results fully sustainable. Indeed, to produce poly(ethylene vanillate) (PEV), Gioia *et al.*[134], first developed an eco-friendly route in opposition to previous pathways which required petrochemical reagents as chloroethanol [143] or toxic compounds such as ethyleneoxide [144].

The polymerization is a one-pot procedure that completely relies on bio-based chemicals, e.g. methyl vanillate and ethylene carbonate, and avoids solvents and purification steps as shown in Scheme 3.2. 1.

This one-pot procedure features an initial step in which methyl vanillate reacts with ethylene carbonate in the presence of K_2CO_3 providing methyl 4-(2-hydroxyethoxy)-3-methoxybenzoate. The etherification reaction on phenolic functionality allows improving its reactivity. Indeed, only when the intermediate is formed the polymerization begins: transesterification occurs in the presence of DBTO catalyst and poly(ethylene vanillate) is produced. It's worth noting that methyl vanillate was chosen instead of vanillic acid because in the initial step VA could react with EC to produce a hydroxyl ester group interfering with the subsequent transesterification reaction.

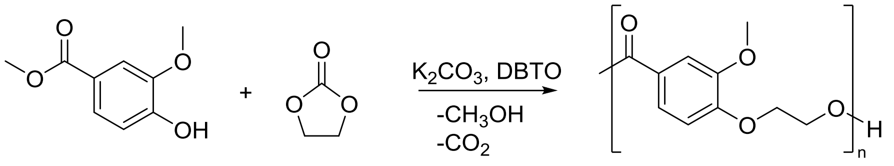

Scheme 3.2. 1: Synthesis of poly(ethylene vanillate) starting from methyl vanillate and ethylene carbonate proposed by Gioia *et al.*[134]

The reported synthetic pathway, in addition to be safe and sustainable, turns out to be very adaptable because it can be applied to prepare even copolymers with different co-units as ε-caprolactone and ricinoleic acid.[134,135] For this reason, this procedure was adapted to produce copolymers with ω-pentadecalacone (PDL), a bio-based macro-lactone bearing 14 methylenic atom carbons.

However, in the reported conditions the ring opening polymerization (ROP) of ω-pentadecanolactone results hard to proceeds: in fact, poly(ω-pentadecanolactone) (PPDL) is usually prepared by means of enzymatic route [145,146] with lipase catalysts. As a consequence, the copolymerization of methyl vanillate with PDL appears as a more complex challenge, because the combination of the two techniques (polycondensation and ROP) requires a catalyst effective both in the Fisher esterification and in the ROP. Antimony (III) oxide proves to be able to satisfy this double demand, as already reported.[147] Copolymers based on methyl vanillate and ω-pentadecanolactone (named P(EV-*co*-PDL)) were synthesized in the presence of K_2CO_3 and Sb_2O_3 in different molar ratio of EV and PDL (EV/PDL 80:20, 60:40, 40:60, 20:80). The schematic procedure is reported in Scheme 3.2. 2. For comparison, also poly(ethylene vanillate) (PEV) was synthesized in the same reaction conditions.

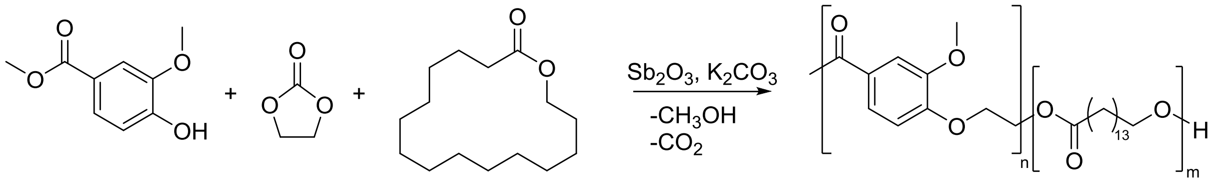

Scheme 3.2. 2: Synthesis of random copolymers named P(EV-*co*-PDL) containing repeating unit derived from methyl 4-(2-hydroxyethoxy)-3-methoxybenzoate (EV) and ω-pentadecalactone (PDL).

Contrary, poly(ω-pentadecalactone) (PPDL) was obtained by enzymatic ring-opening polymerization of ω-pentadecalactone using *Candida antarctica* lipase B according to the study of Focarete *et al.*[145]

3.2.3 Molecular characterization

The structural identification of PEV, PPDL and P(EV-*co*-PDL) copolymers was carried out by ^{1}H-NMR.

Figure 3.2. 1 shows the ^{1}H-NMR spectrum of methyl vanillate while Figure 3.2. 2 shows the ^{1}H-NMR spectrum of poly(ethylene vanillate). The reduction of the ^{a}H proton signal at 3.99 ppm related to the metoxy group and at the same time the appearance of ^{f}H and ^{g}H proton signals at 4.48 and 4.76 ppm related to etherification reaction on phenolic functionality are registered proving that polycondensation occurred.

^{1}H-NMR analysis also confirms chemical structure of poly(ω-pentadecalactone) reported in Figure 3.2. 3.

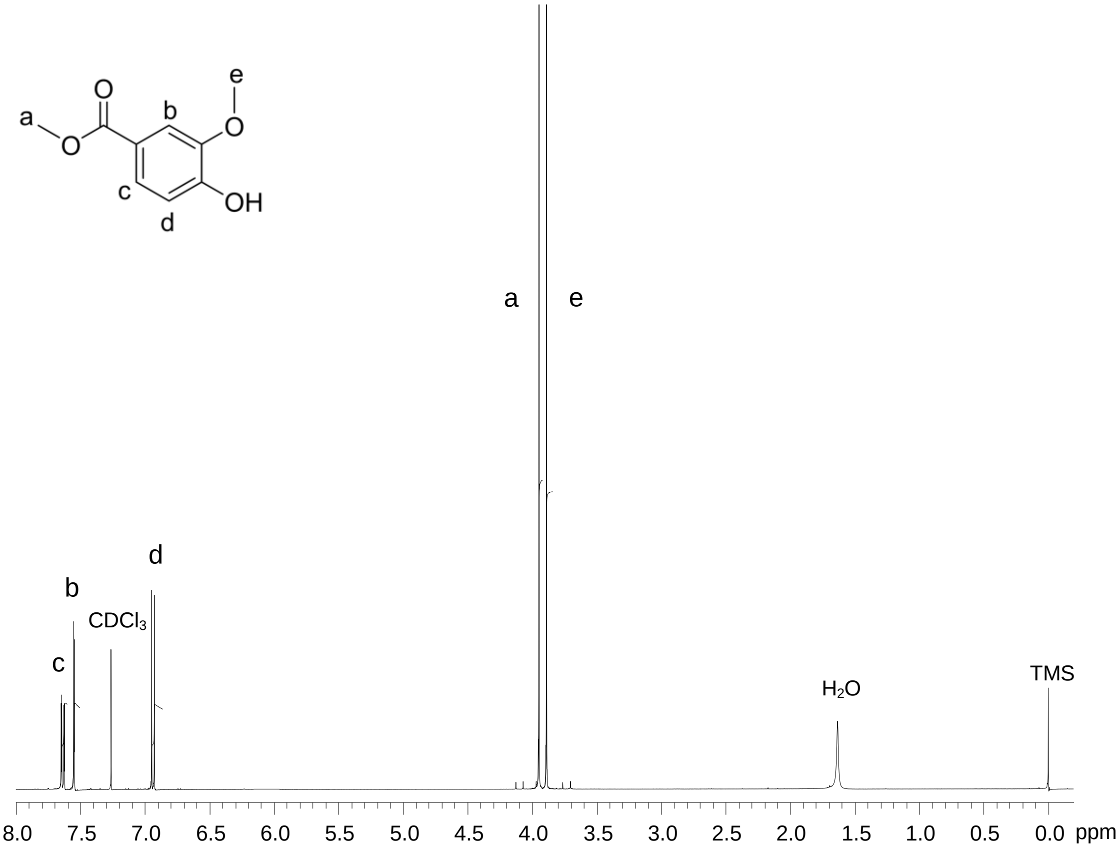

Figure 3.2. 1: ^{1}H-NMR spectrum of methyl vanillate.

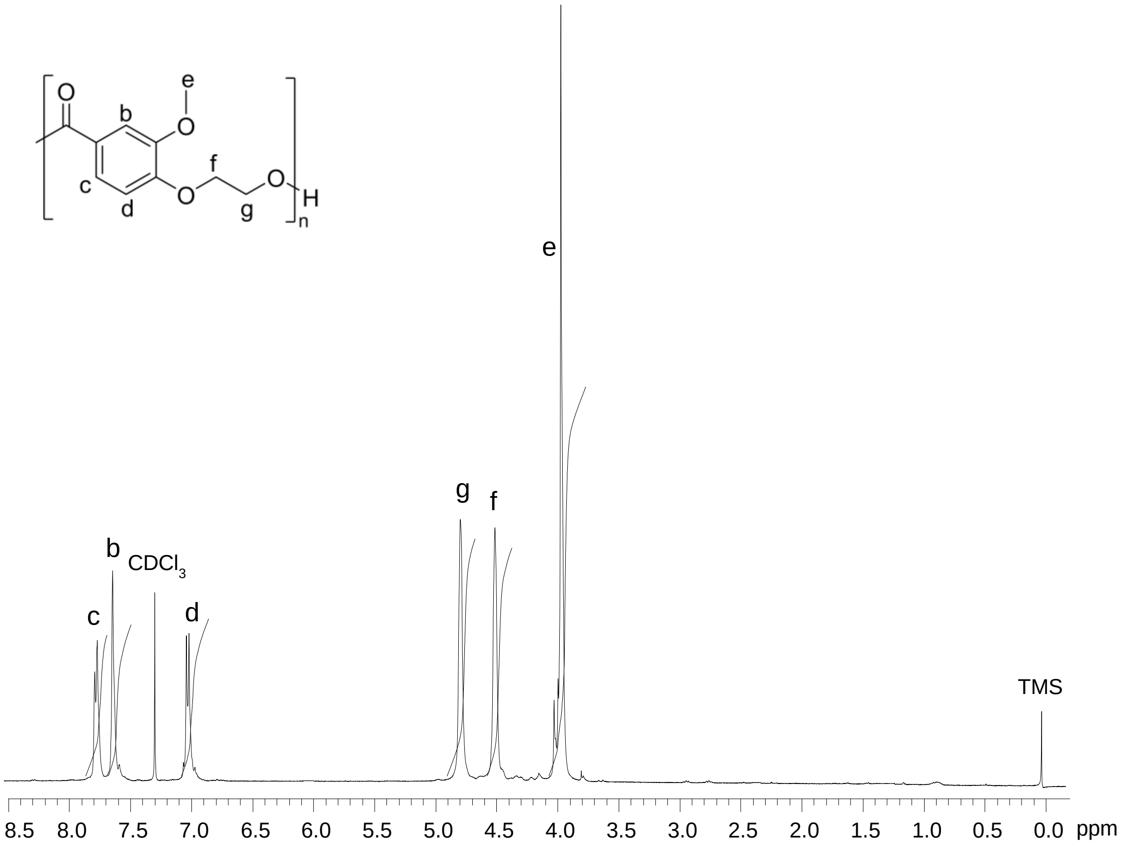

Figure 3.2. 2: ^{1}H-NMR spectrum of poly(ethylene vanillate) PEV.

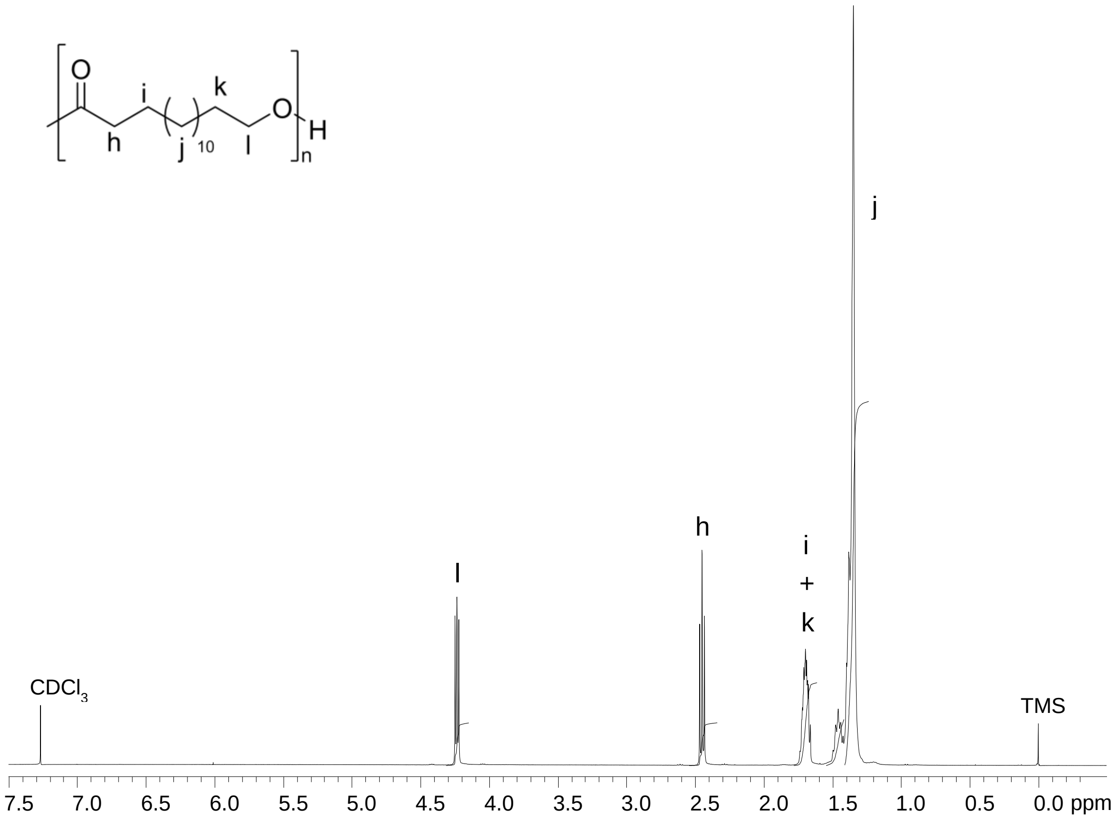

Figure 3.2. 3: ^{1}H-NMR spectrum of poly(ω-pentadecalactone) PPDL.

Based on the ^{1}H-NMR spectra recorded on PEV and PPDL homopolymers, peaks assignment of copolymers P(EV-*co*-PDL) was carried out (Figure 3.2. 4). Scheme 3.2. 3 reports all the four possible diads present in P(EV-*co*-PDL) systems: (1) EV-EV sequence, obtained from the reaction between carboxylic and hydroxylic groups of the EV units, (2) PDL-PDL sequence, obtained from the reaction between the carboxylic and hydroxylic groups of the PDL units, (3) EV-PDL sequence, obtained from the reaction between hydroxylic groups of the EV units and carboxylic groups of PDL units, and (4) PDL-EV sequence, obtained from the reaction between hydroxylic groups of PDL units and carboxylic groups derived from EV units.

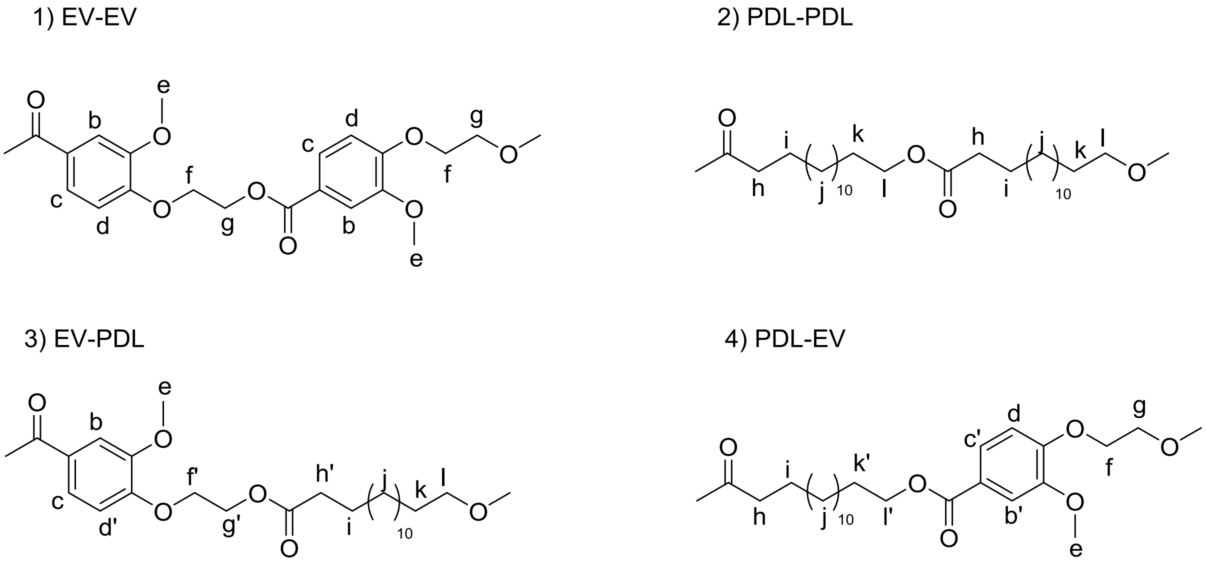

Scheme 3.2. 3: Diads present in P(EV-*co*-PDL) random copolymers.

For the aromatic ^{b}H and ^{c}H protons the signals centred at 7.59 and 7.71 ppm change their multiplicity with respect to the corresponding signal recorded for the homopolymer, thus indicating a weak influence of the neighbouring PDL units in PDL-EV sequence (represented as $^{b'}$H and $^{c'}$H in Scheme 3.2. 3). The other aromatic ^{d}H proton, instead, is strongly influenced by the neighbouring unit (EV or PDL) and two multiplets are observed at 7.00 (proton ^{d}H) and 6.95 ppm (proton $^{d'}$H), corresponding to EV-EV and EV-PDL sequences respectively. The signal at 3.93 ppm of ^{e}H protons remains a singlet.

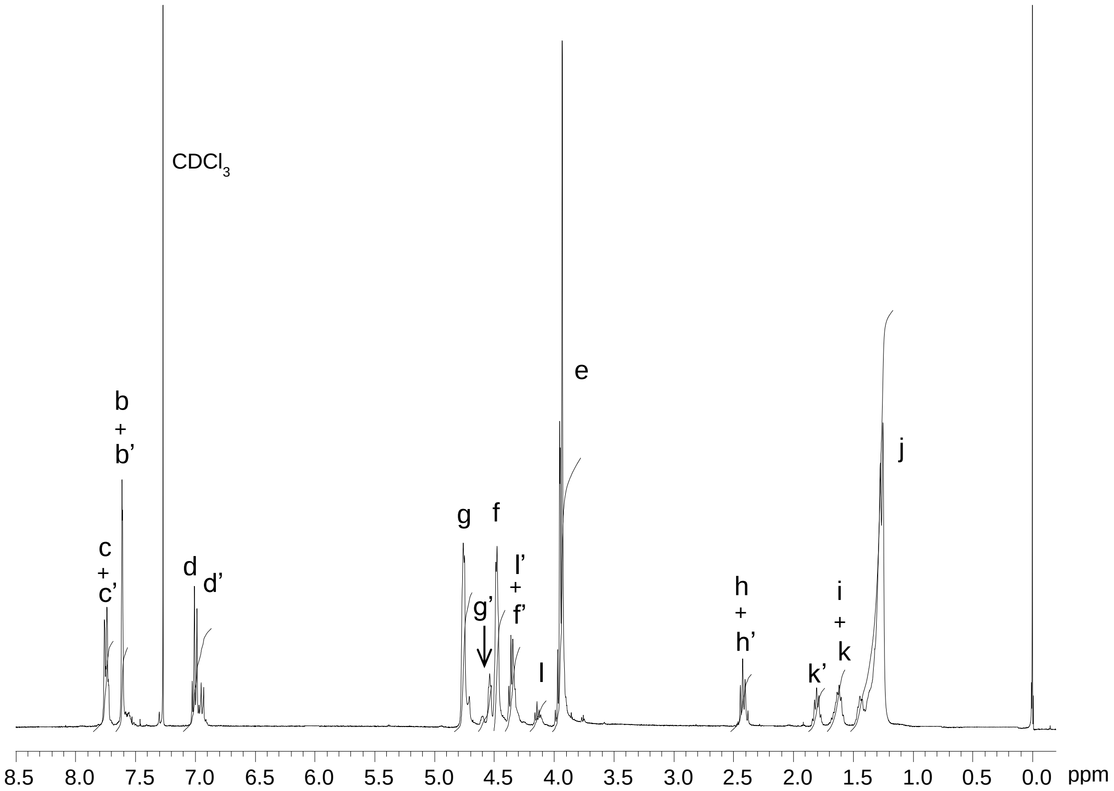

Figure 3.2. 4: ^{1}H-NMR spectrum of copolymer P(EV-*co*-PPDL) 80/20.

The aliphatic ^{g}H proton (in α to the ester oxygen atom) and ^{f}H proton (linked to the ether group) are also influenced by the neighbouring units, according to the EV-EV and EV-PDL diads in Scheme 3.2. 3 (^{g}H centered at 4.76 ppm, $^{g'}$H at 4.55 ppm, ^{f}H at 4.49 ppm and $^{f'}$H at about 4.36 ppm). Only the signal of ^{g}H proton is well resolved, while the $^{g'}$H, ^{f}H and $^{f'}$H protons signals partially overlap with other signals.

The ^{l}H (4.15 ppm), ^{h}H (2.42 ppm), ^{k}H, ^{i}H (1.62 ppm) and ^{j}H (1.12-1.50 ppm) protons are assigned to the PDL unit according to the signals recorded for the PPDL sample. PDL-unit protons in α and β to the ester oxygen atom (^{l}H, ^{k}H) are strongly influenced by the neighbouring unit (PDL or EV) (see PDL-PDL and PDL-EV diads in Scheme 3.2. 3) and the signals due to $^{l'}$H (4.36 ppm) and $^{k'}$H (1.81 ppm) protons are also observed in the spectrum, even if the $^{l'}$H proton signal overlaps with that of the $^{f'}$H. The ^{h}H proton, in α to the ester carbonyl moiety in the PDL unit, appear to be weakly influenced by whether the neighbouring group is a PDL or EV-unit and only a change in the multiplicity of the signals is observed represented as $^{h'}$H in Scheme 3.2. 3. The ^{j}H proton (centred at 1.26 ppm) isn’t affected by the neighbouring unit.

To determine the molar fractions of copolymer units, the signals at 3.93 ppm (proton ^{e}H of EV-unit) and at 2.39 ppm (proton ^{h}H of PDL-unit) were chosen, because independently of the molar composition such signals maintain their chemical shifts and do not show any splitting, thus assuring a minimal error in the integration evaluation. Therefore, the molar fractions of EV (F_{EV}) and PDL (F_{PDL}) units were calculated by means of the equations:

$$F_{EV} = \frac{I_e/3}{I_e/3 + I_h/2} \tag{3.2. 1}$$

$$F_{PDL} = \frac{I_h/2}{I_e/3 + I_h/2} \tag{3.2. 2}$$

where I is the integration intensity of signals.

Values of F_{EV} are listed in Table 3.2. 1.

Table 3.2. 1 shows the molecular weights of all the synthesized samples determined by GPC analysis in a mixture of $CHCl_3$/1,1,1,3,3,3-hexafluoro-2-propanol (HFIP) (95/5 vol%). Since PEV is insoluble in the GPC solvent, its number average molecular weight was determined by ^{1}H-NMR.

Table 3.2. 1: Molar fraction of EV units and molecular weights of PEV, PPDL and P(EV-*co*-PDL) copolymers.

sample	F_{EV} [a]	Mn × 10^{-3} [b] (g mol^{-1})	Mw × 10^{-3} [b] (g mol^{-1})
PEV	1	11.0 [c]	-
P(EV-*co*-PDL) 80/20	0.81	7.3	17.3
P(EV-*co*-PDL) 60/40	0.61	8.5	20.5
P(EV-*co*-PDL) 40/60	0.37	7.2	13.9
P(EV-*co*-PDL) 20/80	0.19	10.0	23.8
PPDL	-	37.5	63.7

[a] measured by ^{1}H-NMR analysis by equation 3.2. 1. [b] measured by GPC analysis. [c] measured by ^{1}H-NMR analysis.

3.2.4 Thermal stability

The thermogravimetric curves reported in Figure 3.2. 5A show that the degradation process occurs at temperatures (T_{onset}) higher than 370 °C for all the synthesized materials. PEV degrades first at 372 °C while PPDL shows thermal resistance up to 407 °C; the copolymers exhibit in-between thermal stability up to 386/399 °C. Table 3.2. 2 lists the initial degradation temperatures (T_{onset}) and the temperatures at which the decomposition rate is maxima (T_p).

Since PEV thermal stability is lower than that of PET (T_p = 440 °C) [148] despite their similar chemical structures, PEV thermal lability has to be ascribed mainly to ether bonds, which are generally referred as weak points as for DEG groups in PET.[149] In random copolymers the reduction of ether linkages because of the inclusion of PDL units results in higher thermal stability than PEV. Moreover, both for PEV and copolymers, thermal stability is affected by their low molecular weight, whose influence on the final thermal resistance is well known in literature.[150] As far as the PPDL sample is concerned, it presents a notably high T_{onset} value, as confirmed by the literature where it is reported that PPDL has a higher thermal stability compared to other polylactones, such as poly(glycolic acid), poly(lactic acid) and poly(ε-caprolactone) whose peak decomposition temperatures (T_p) are 360, 295, 402 °C, respectively.[151]

PEV and copolymers rich in PEV show a single degradation step while PPDL and copolymers rich in PPDL show two degradation steps: a main one where about 90% of the initial weight is lost, followed by a minor final loss appearing as a shoulder (Figure 3.2. 5B). As reported by Focarete *et al.*[145] in the first degradation step the main volatile product is carbon dioxide whereas in the second step a cluster of higher mass products analogous to those released by low-density polyethylene [152] attributed to the degradation of the hydrocarbon part of poly(PDL) chain is observed. PPDL degradation process ends in a complete weight loss.

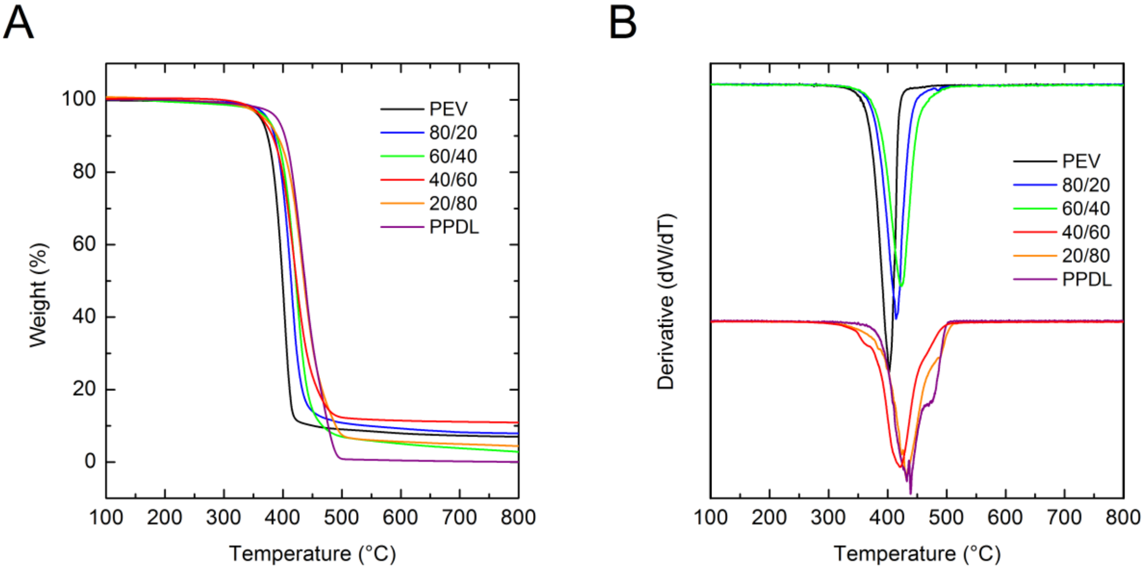

Figure 3.2. 5: Thermogravimetric curves of PEV, PPDL and P(EV-*co*-PDL) copolymers at 10 °C min^{-1} under N_2 atmosphere (**A**) and their derivatives (**B**).

3.2.5 Non-isothermal DSC analysis and WAXS analysis

Figure 3.2. 6 shows DSC cooling and subsequent heating scans at 10 °C min^{-1} on PEV, PPDL homopolymers and P(EV-*co*-PDL) copolymers while Table 3.2. 2 reports the corresponding calorimetric data. Figure 3.2. 7 shows WAXS diffractometer profiles at room temperature of the samples obtained by melting and subsequent controlled cooling at 10 °C min^{-1}.

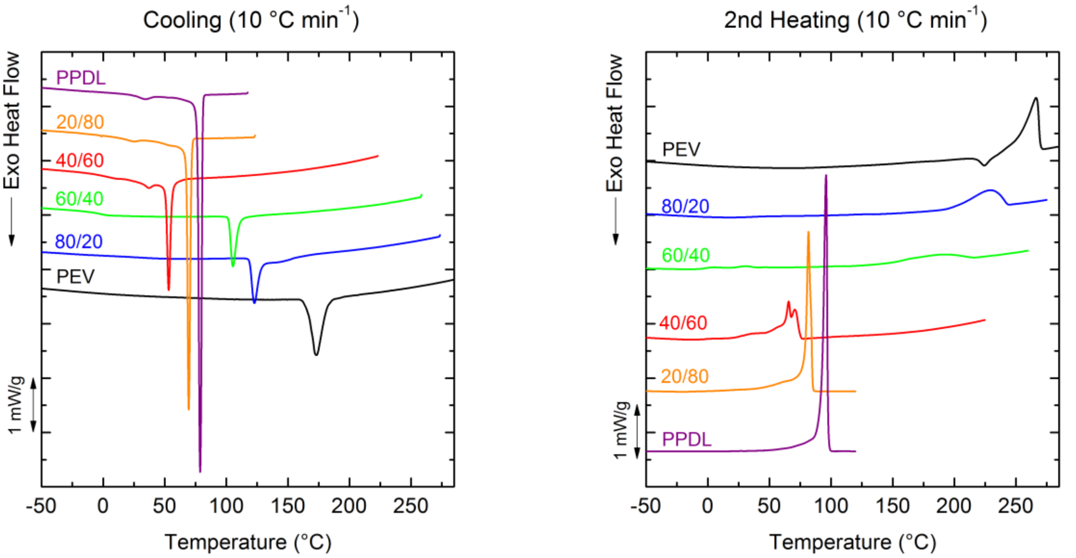

Figure 3.2. 6: Non-isothermal DSC analysis of PEV, PPDL and P(EV-*co*-PDL) copolymers. Cooling scans from the melt and 2nd heating scans at 10 °C min^{-1}. The curves are normalized by the weight of the sample.

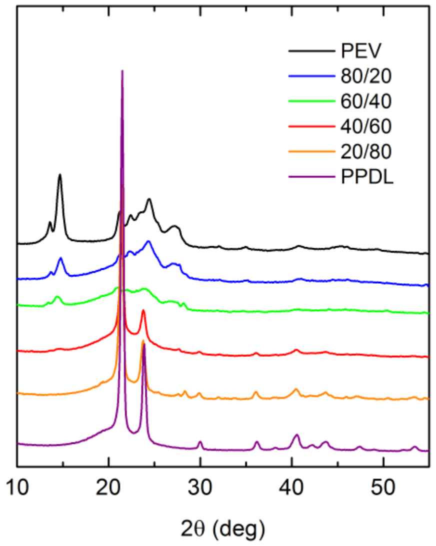

Figure 3.2. 7: X-ray diffractometer profile of PEV, PPDL and P(EV-*co*-PDL) copolymers.

As reported in Table 3.2. 2 all the samples are semicrystalline and the Tg values vary as a function of the composition, indicating a single homogeneous amorphous phase.

During cooling scan, homopolymers and the copolymers rich in PEV or PPDL units (80/20 and 20/80 samples) show a single crystallization peak while the copolymers with intermediate compositions (60/40 and 40/60 samples), although present a main crystallization peak which can be related to the crystalline phase of the major comonomer, show more complicated thermograms due to the presence of the comonomeric units.

PEV presents high values of crystallization temperature (173 °C) and enthalpy (69 J g^{-1}), confirming the ability of the polymer to reach a state of high order when cooled from the melt. WAXS analysis on PEV sample at room temperature (Figure 3.2. 7) validates this consideration: its pattern is characterized by the presence of six intense reflections at about 13.55°, 14.65°, 21.25°, 22.25°, 24.25° and 27.05°.

As expected, also PPDL exhibits very high value of crystallization enthalpy (124 J g^{-1}) at lower temperature (79 °C). Its ability to crystallize is confirmed by WAXS analysis since PPDL diffraction profile (Figure 3.2. 7) shows intense reflections at 21.31° and 23.79°. Powder-diffraction pattern of PPDL is similar to that of PE [153] proving similarity in crystal structures. Indeed, as stated by Gazzano *et al.*[154] PPDL unit cell is pseudo-orthorhombic with the following lattice parameters a = 7.40 Å, b = 4.93 Å, c = 2.534 Å and α = 90.06 °. The polymer chains disposed in a planar zigzag conformation inside the crystal are parallel to the c-axis of the unit cell.

P(EV-*co*-PDL) 80/20 copolymer show a single crystallization peak at 123 °C with ΔHc = 48 J g^{-1} meaning that it crystallizes in the phase of PEV homopolymer as confirmed by WAXS measurement since 80/20 sample exhibits the typical reflections observed for PEV. However the lower Tc with respect to that of PEV indicates lower crystals perfection as expected for random copolymers.

Similar behaviour is registered for the copolymer rich in PPDL: P(EV-*co*-PDL) 20/80 presents a single crystallization peak at lower temperature (69 °C) and with lower ΔHc (93 J g^{-1}) than PPDL and reflects the diffractometer pattern of PPDL.

On the other hand, copolymers with intermediate compositions, i.e. P(EV-*co*-PDL) 60/40 and 40/60, present multiple exothermic processes. P(EV-*co*-PDL) 60/40 shows a sharp peak at 105 °C which can be referred to PEV crystalline phase and a broad small peak at lower temperature (6 °C) referable to PPDL crystalline phase. It probably presents two crystalline phases even if WAXS analysis confirms that PEV crystalline phase, which is the major comonomer, prevails. P(EV-*co*-PDL) 40/60 shows two peaks at 37 and 53 °C both ascribable to PPDL crystals. WAXS analysis confirms that a single phase referable to PPDL crystalline phase occurs in P(EV-*co*-PDL) 40/60 copolymer. However, the double crystalline peak means the formation of imperfect PPDL crystals. This different behaviour between 60/40 and 40/60 copolymers suggests that PDL comonomer is able to crystallize even when present in 40% molar fraction unlike EV comonomer does.

Table 3.2. 2: Thermal properties of PEV, PPDL and P(EV-*co*-PDL) copolymers obtained from TGA and DSC non-isothermal analysis.

sample	T_{onset} (°C) [a]	T_p (°C) [a]	Tc (°C)[b]	ΔHc (J g^{-1}) [b]	Tm (°C) [c]	ΔHm (J g^{-1}) [c]	Tg (°C) [c]
PEV	372	404	173	69	266	78	74[d]
P(EV-*co*-PDL) 80/20	391	416	123	48	229	49	34
P(EV-*co*-PDL) 60/40	395	423	6-105	6-34	31-187	2-26	-2
P(EV-*co*-PDL) 40/60	386	420	37-53	63	66-71	61	-3
P(EV-*co*-PDL) 20/80	399	431	69	93	82	99	not detectable
PPDL	407	439	79	124	96	132	-27[e]

[a] measured by TGA analysis in nitrogen at 10 °C min^{-1}. [b] measured by non-isothermal DSC analysis during the cooling scan at 10 °C min^{-1}. [c] measured by non-isothermal DSC analysis during the 2nd heating scan at 10 °C min^{-1}. [d] measured by non-isothermal DSC analysis during the 2nd heating scan at 10 °C min^{-1} of the amorphous sample obtained after quenching from the melt, using liquid nitrogen. [e] measured by DMTA analysis from ref.[145]

In the second heating scan, depending on the crystalline phases formed during cooling, one or two melting peaks are recorded. PEV exhibits very high melting temperature (266 °C) and enthalpy (78 J g^{-1}) in agreement with Gioia *et al.*[134] PEV is characterized by higher melting enthalpy than PET (45 J g^{-1}) demonstrating the attitude of PEV to crystallize and to reach a state of high order. Such behavior has been ascribed to the higher mobility of the constituent units of PEV chain with respect to the terephthalic units of PET.[134] Indeed, in terephthalic units the sp^2 hybridization of the carbon atoms of the two carboxylic groups induces coplanarity between carboxyl and phenyl groups, restricting the rotational angles of Cphenyl-COO to 0 and 180°. In PEV such rigidity is avoided because one carboxylic group is substituted by an ether unit, which can confer more flexibility to the chain and can impart a higher chain folding capability. This chain folding ability can probably overcome the hindrance to crystallization due to the presence of the side methoxy group.

PPDL shows the melting endotherm at 96 °C associated with a very high melting entlaphy of 132 J g^{-1}. Melting temperature of PPDL interpose between Tm of PCL (58 °C) and Tm of PE (HDPE 120 °C).

A single melting peak is also observed for P(EV-*co*-PDL) 80/20 and 20/80 at 229 °C and 82 °C respectively. The lower Tm values with respect to the values of the respective homopolymer indicate low crystal perfection due to the comonomer interference present at 20% of molar composition. The melting enthalpy is 49 J g^{-1} for P(EV-*co*-PDL) 80/20 and 99 J g^{-1} for P(EV-*co*-PDL) 20/80 proving the enhanced ability of PPDL moiety to crystallize.

P(EV-*co*-PDL) 60/40 show two broad melting peaks at 31 °C and 187 °C related to the two crystalline phases: one referable to PDL units and the other to EV units.

P(EV-*co*-PDL) 40/60 shows a broad melting process that starts at 35 °C and ends at 76 °C meaning the formation of imperfect crystals because of the inclusion of EV units.

3.2.6 Isothermal DSC analysis

The isothermal crystallization process of the synthesized materials was studied by means of DSC in order to investigate the overall crystallization rate and compare it with commercial polymers such as PET and poly(buthylene terephthalate) (PBT).

After a rapid quench (150 °C min^{-1}) from the molten state, the sample was held at the chosen temperature of crystallization (Tc) for the time long enough to complete the crystallization process. The half-crystallization time ($t_{1/2}$) is the time necessary to reach the 50% of crystallinity measured as enthalpy of crystallization and $t_{1/2}$-t_0 is the difference between the half-crystallization time and the time at which crystallization begins. The inverse of $t_{1/2}$-t_0 provides an experimental measure of the overall crystallization rate. Table 3.2. 3 reports the values of crystallization temperature (Tc) and the values of $t_{1/2}$-t_0 for PEV, P(EV-*co*-PDL) and PPDL samples.

Table 3.2. 3: Isothermal crystallization temperatures (Tc) and $t_{1/2}$-t_0 values for PEV, P(EV-*co*-PDL) and PPDL samples.

Isothermal crystallization											
PEV		80/20		60/40		40/60		20/80		PPDL	
Tc (°C)	$t_{1/2}$-t_0 (min)	Tc (°C)	$t_{1/2}$-t_0 (min)	Tc (°C)	$t_{1/2}$-t_0 (min)	Tc (°C)	$t_{1/2}$-t_0 (min)	Tc (°C)	$t_{1/2}$-t_0 (min)	Tc (°C)	$t_{1/2}$-t_0 (min)
240	1.63	172	1.47	138	2.10	63	2.82	76	2.16	84	1.31
242	2.39	176	2.09	142	2.67	64	3.57	77	3.79	85	3.17
244	3.19	180	2.66	144	3.13	64.5	4.93	78	6.65	85.5	5.74
246	4.86	182	3.12	146	3.33	65	5.82	79	15.31	86	7.54
248	6.84	184	3.47	148	4.06	66	7.52	80	33.01	87	16.99
		186	4.07	150	4.35						
		188	4.81								

As reported in Table 3.2. 3 it's worth noting that isothermal crystallization was studied at high Tc, near the melting point and far from the crystallization peak registered during cooling at 10 °C min^{-1} (Figure 3.2. 6), for all the samples. Since the range of crystallization temperatures of the two homopolymers are significantly different, in copolymers only the crystallization of the major comonomer occurs, i.e. single-phase crystallization: for P(EV-*co*-PDL) rich in PEV, the Tc is high enough that PDL moiety is in the molten state, while for P(EV-*co*-PDL) rich in PPDL, PEV moiety doesn't crystallize when present in 40% or lower as shown by WAXS analysis (Figure 3.2. 7).

Figure 3.2. 8 shows typical heating scans of the samples that were isothermally crystallized at different temperatures (Tc) and subsequently melted.

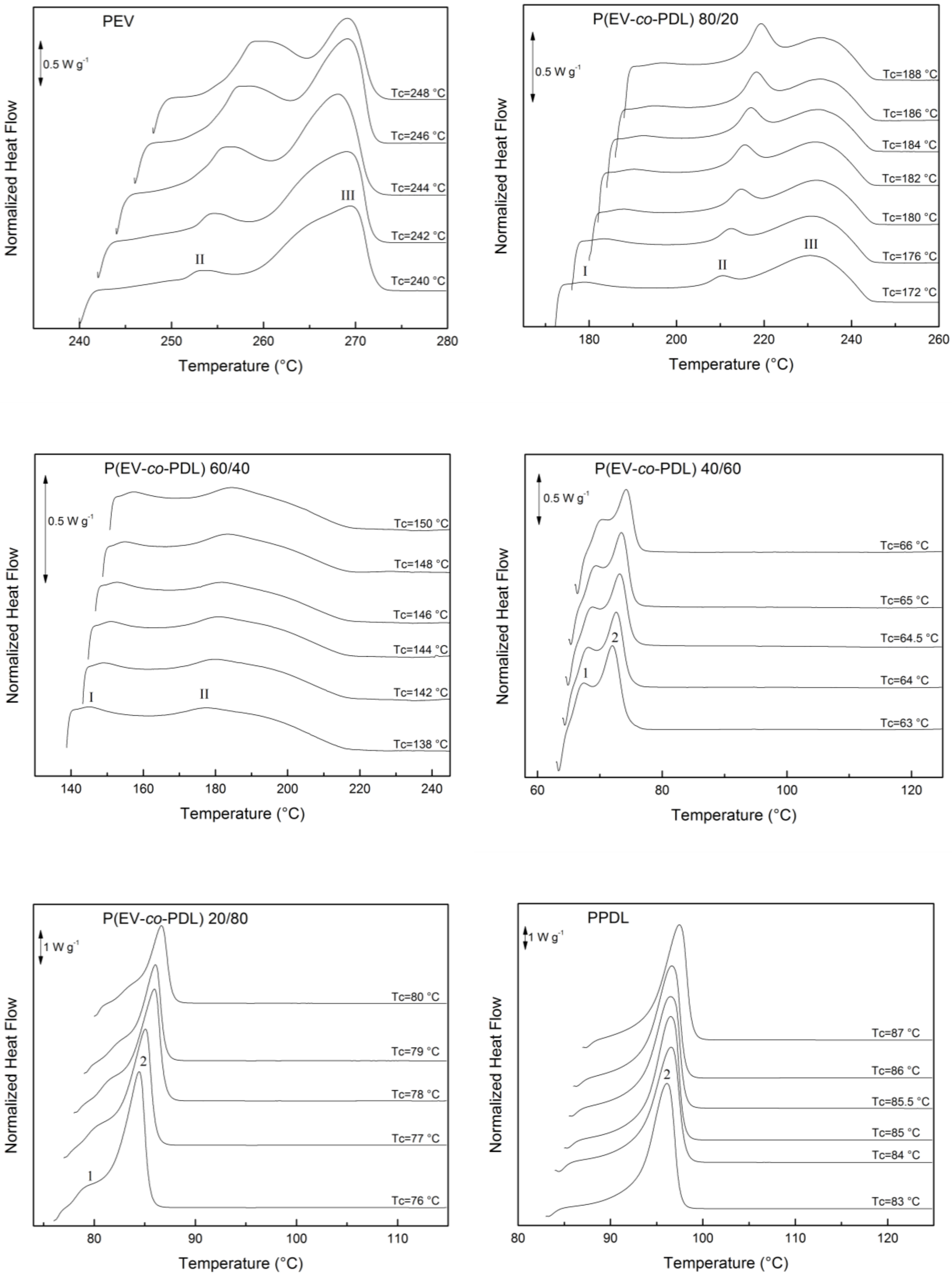

Figure 3.2. 8: Heating scans at 10 °C min^{-1} of PEV, P(EV-*co*-PDL) and PPDL samples after crystallization at the Tc indicated on the curves.

As shown, multiple and complex melting process are involved both in homopolymers and copolymers. In order to better understand such behaviour, we first focus our attention on homopolymers curves. In PEV sample, two endotherms appear in the thermogram and are labelled with Roman numerals (II and III). Peak II can be ascribed to the fusion of the crystals actually formed at Tc during primary crystallization while peak III can be associated to the fusion of the crystals with higher perfection, grew during the heating scan as a consequence of recrystallization. Recrystallization phenomena in PEV sample is confirmed by the small exotherm exhibited during the non-isothermal DSC 2nd heating scan (Figure 3.2. 6) just before the single melting peak. PPDL shows a single melting peak labelled with Arabic numerals (2) which is associated to the fusion of the crystals formed at Tc. Already during primary crystallization PPDL sample forms crystals with high perfection. In copolymers samples, appear an extra endotherm peak labelled as (I) for copolymers reach in PEV and (1) for copolymers reach in PPDL. The peak can be referred to the melting of defective crystals grew at Tc. In P(EV-*co*-PDL) 80/20 all the peaks (I, II, III) are registered, in P(EV-*co*-PDL) 60/40 peak I is more pronounced while peak III is overlapped to peak II since a broad melting peak is registered. As far as P(EV-*co*-PDL) 20/80 and P(EV-*co*-PDL) 40/60 is concerned, peak 1 is detected as expected because of the formation of imperfect crystals due to EV units presence.

The equilibrium melting temperature (Tm°) is a crucial parameter to determine the undercooling (ΔT=Tm°-Tc) necessary to compare crystallization rates. Tm° is the melting temperature of lamellar crystals with an infinite thickness and was determined by the Hoffman and Weeks method.[155] That method analyses the dependence of the melting temperatures (Tm of peak II or 2) of crystals grown at the corresponding Tc through the relationship:

$$T_m = T_m^{\circ}\left(1 - \frac{1}{\gamma}\right) + \frac{T_c}{\gamma} \qquad (3.2.\ 3)$$

where γ is a factor depending on lamellar thickness.

In that method, the observed melting temperatures (Tm) of the crystals formed at different temperatures of crystallization are plotted against the crystallization temperature (Tc), and the Tm° is estimated at the intersection point with the linear fit Tm=Tc. Figure 3.2. 9 presents the Hoffman and Weeks plots constructed for PEV, PPDL homopolymers and P(EV-*co*-PDL) copolymers while the calculated values after the extrapolation are reported in Table 3.2. 4 together with the values of r^2.

The value of Tm° for PPDL sample is the same reported by Cai *et al.*[156] Instead, the value of Tm° calculated for PEV sample is different from that reported by Zamboulis *et al.*[157] (301.4 °C) because they plotted Tm° values of peak III against Tc.

In random copolymers the theoretical equilibrium melting temperature (Tm°$_{co}$) can be determined by theories based on the comonomer exclusion model. The Baur equation [158] is particularly interesting as it takes into account the molar fraction Xc of crystallizable comonomer as follows:

$$\frac{1}{T^{\circ}_{m,co}} = \frac{1}{T^{\circ}_{m}} - \left(\frac{R}{\Delta H^{\circ}_{m}}\right) \cdot [ln x_c - 2x_c(1 - x_c)] \tag{3.2. 4}$$

where Tm° and ΔHm° are the equilibrium melting temperature and enthalpy of the corresponding homopolymer and R is the gas constant.

By setting homoplymers Tm° values determined in the present work and homopolymers ΔHm° values determined in the study of Zamboulis *et al.*[157] and of Cai *et al.*[156] for PEV (166 J g^{-1}) and PPDL (227 J g^{-1}) respectively, theoretical equilibrium melting temperatures (Tm°$_{co}$) very close to the experimentally estimated one were obtained and are reported in Table 3.2. 4. Such trend confirms the validity of the Bauer model and hence the occurrence of complete rejection of minority comonomer by the crystals.

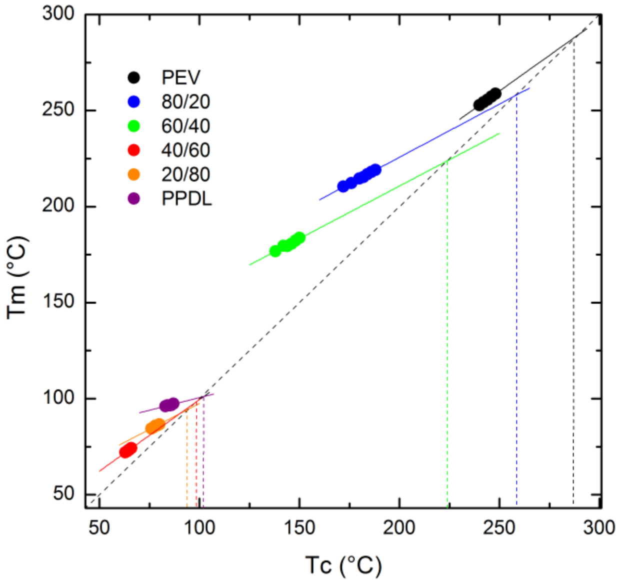

Figure 3.2. 9: Hoffmann-Weeks plots for the determination of Tm° of PEV, PPDL and P(EV-*co*-PDL) copolymers.

Table 3.2. 4: Equilibrium melting temperatures of PEV, PPDL and P(EV-*co*-PDL) copolymers.

sample	Tm° (°C)[a]	r^2	Tm°$_{co}$ (°C)[b]
PEV	290	0.998	-
P(EV-*co*-PDL) 80/20	258	0.997	251
P(EV-*co*-PDL) 60/40	224	0.961	223
P(EV-*co*-PDL) 40/60	98	0.994	82
P(EV-*co*-PDL) 20/80	95	0.954	91
PPDL	101	0.965	-

[d] determined experimentally by Hoffmann-Weeks plots. [b] determined by the Baur model.

Figure 3.2. 10 shows plots of the overall crystallization rate expressed as $1/(t_{1/2}-t_0)$, as a function of undercooling for all the synthesized samples. The half-crystallization time ($t_{1/2}$) is the time necessary to reach the 50% of crystallinity measured as enthalpy of crystallization during isothermal DSC experiments, t_0 is the time at which crystallization begins and the inverse of $t_{1/2}-t_0$ ($1/t_{1/2}-t_0$) provides an experimental measure of the overall crystallization rate; undercooling (ΔT) is the difference between the equilibrium melting temperature, Tm°, and the isothermal crystallization temperature, Tc. As previously mentioned, the crystallization experiments were performed at Tc near the melting point for all the samples since at lower Tc, crystallization is too fast and the samples start to crystallize during rapid cooling. The solid lines shown in Figure 3.2. 10 correspond to arbitrary fits performed to guide the eye. PET (Mw = 68400 g mol^{-1}) and PBT (Mw = 77400 g mol^{-1}) were used as reference materials from the study of Chisholm *et al.*[159] It is clearly shown that the aliphatic polyester PPDL crystallize very fast while the aromatic polyesters (PEV, PBT and PET) have slower crystallization rate. PEV is characterized by a crystallization rate similar to that of PBT, faster with respect to that of PET. Copolymers show behaviour similar to that of the corresponding homopolymer although characterized by a slower crystallization rate, depending on the composition.

The crystallization process consists of two consecutive phenomena: nucleation and crystal growth. Nucleation of a crystal starts with the formation of small-sized areas where a group of molecular chains or their segments occur aligned (primary nucleation) whereas crystal growth is achieved by further addition of polymer chains which first diffuse towards the growth front and then form an ordered surface.

Polymer chain flexibility is a crucial parameter as it correlates to the diffusion in the molten state and to the chain folding capability during the formation of the crystal. By comparing the chemical structures of PPDL and aromatic polyester (PEV, PBT and PET), it is evident that the long aliphatic sequence of 14 -(CH_2)- units of PPDL is very flexible thus fitting easily in folded crystals: PPDL is the fastest crystallizing polymer in Figure 3.2. 10.

Inside the poly(alkyleneterephtalate)s, PBT is characterized by a sequence of four methylene units while PET by two hence justifying the improved chain mobility and crystallization of PBT. From Figure 3.2. 10, it results that PEV has a crystallization rate similar to that of PBT proving their comparable chain flexibility. It can be deduced that, in spite of the two methylene units as PET, PEV chain has higher rotational freedom around the aromatic ring that imparts a chain folding capability during crystallization similar to that of PBT.

As far as random copolymers is concerned, they retain the same chain flexibility of the respective homopolymer but the crystallization rates result slowed down because of the presence of the comonomer. The minority comonomer is fully excluded from the crystalline phase and constitutes defects for the crystals formation.

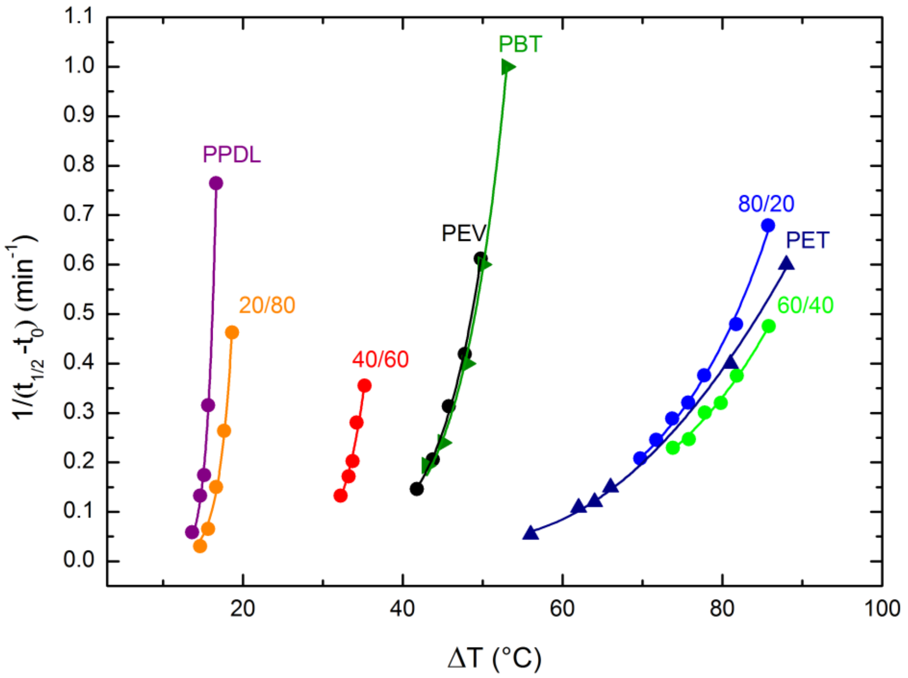

Figure 3.2. 10: Crystallization rate ($1/t_{1/2}$-t_0) as a function of the undercooling for PEV, PPDL and P(EV-*co*-PDL) copolymers samples, PBT and PET of ref. [159].

3.2.7 Processability

The synthesized copolymers powders were thermo-pressed between two Teflon sheets to obtain films. Since all the copolymers are characterized by a lower degree of crystallinity with respect to PEV homopolymer, films were successfully obtained for all the copolymers. In Figure 3.2. 11 is reported the film of P(EV-*co*-PDL) 80/20 copolymer.

As expected, copolymers with intermediate compositions, i.e. 60/40 and 40/60, appear more flexible than the copolymers 80/20 and 20/80 because of their lower crystallization ability. Therefore, the brittleness of PEV homopolymer can be overcome and the copolymers appear as interesting bio-based materials for possible applications in flexible packaging.

Figure 3.2. 11: P(EV-*co*-PDL) 80/20 copolymer film.

3.2.8 Conclusions

Novel copolyesters, based on vanillic acid and ω-pentadecalactone, have been successfully synthesized and characterized. The synthesis is a one-pot procedure, no solvent involved, and no purification step is required, demonstrating to be suitable for an industrial upscaling, even if the availability of bio-based vanillic acid is still a matter of discussion.

The obtained random copolymers are characterized by good thermal stability, a homogeneous amorphous phase, crystal phases that depend on the composition and a lower ability to crystallize than the corresponding homopolymers PEV and PPDL. As a matter of fact, the copolymerization with ω-pentadecalactone proofs to be a relevant strategy to moderate the brittleness of PEV homopolymer due to the copolymers' lower degree of crystallinity. Random copolymers demonstrate to be processable and filmable and hence they can be considered potential bio-based substitutes of petro-derived aromatic polyesters for packaging applications.

The end of life of these materials was not studied yet, but it is expected that strategies of recycling can be successfully applied.

In conclusion, the vanillin platform for polymer synthesis is now enriched of new copolymers with tuneable properties.

3.2.9 Experimental

3.2.9.1 Materials

Vanillic acid (VA) and ethylene carbonate (EC) with purities of 99% or more were purchased from Zentek. ω-pentadecalactone (PDL) (>98%), sulfuric acid H_2SO_4 (>97.5%), potassium carbonate K_2CO_3 (99%), antimony (V) oxide Sb_2O_3 (99.99%) and Lipase B *Candida antartica* (immobilized on Immobead 150, recombinant from yeast) were purchased from Sigma-Aldrich. Reagents were used as received without further purification.

3.2.9.2 Synthesis of methyl vanillate monomer

Vanillic acid (33.6 g, 0.200 mol), methanol (300 ml) and sulfuric acid (2 ml) were introduced in a round-bottom flask equipped with a magnetic stirrer and a reflux column. The mixture was heated at 80 °C for 24 hours until a clear solution was obtained. Methanol was removed under reduced pressure; the product was solubilized in 75 ml of ethyl acetate and washed twice with deionized water (100 ml). The organic phase was collected, anhydrified and ethyl acetate was removed under reduced pressure to obtain dense oil. Finally, the product was crystallized in water to obtain pure methyl vanillate (yield 98%).

^{1}H-NMR (400 MHz, $CDCl_3$, δ): 7.63 (dd, J_1=1.95 J_2=8.2 Hz, 1H, C^cH), 7.55 (d, J=1.95 Hz, 1H, C^bH), 6.94 (d, J=8.2 Hz, 1H, C^dH), 3.94 (s, 3H, C^aH_3), 3.88 (s, 3H, C^eH_3) ppm.

3.2.9.3 Synthesis of poly(ethylene vanillate) homopolymer (PEV)

Methyl vanillate (25.0 g, 0.137 mol), ethylene carbonate (13.3 g, 0.151 mol), K_2CO_3 (0.142 g, 0.00103 mol), Sb_2O_3 (1 wt% to the final product) were introduced into a 500ml glass reactor bottle equipped with a mechanic stirrer and connected to nitrogen flow. The polycondensation was performed in two stages. In the first stage, the mixture was heated under nitrogen atmosphere at 180 °C for 1 hour and then the temperature was gradually increased until 240 °C in the subsequent 2 hours. In the second stage, the pressure was slowly reduced from atmospheric to 0.3 mbar while the temperature was gradually increased up to 270 °C during 3 hours. Finally, the resulting material was collected from the reactor and purified by dissolution in $CHCl_3$ and $CHCl_3$/1,1,1,3,3,3-hexafluoro-2-propanol (HFIP) (80/20 v/v) mixture, filtration of insoluble catalyst and finally precipitation in cold methanol (yield 85%).

^{1}H-NMR (400 MHz, $CDCl_3/CF_3COOD$, δ): 7.74 (dd, 1H, C^cH), 7.61 (d, 1H, C^bH), 6.99 (d, 1H, C^dH), 4.76 (t, 2H, C^gH_2), 4.48 (t, 2H, C^fH_2), 3.93 (s, 3H, C^eH_3) ppm.

3.2.9.4 Synthesis of poly(ethylene vanillate-*co*-ω-pentadecalactone) copolymers (P(EV-*co*-PDL))

Methyl vanillate (25.0 g, 0.137 mol), ethylene carbonate (13.3 g, 0.151 mol), ω-pentadecalactone (in different amount depending of the desired composition), K_2CO_3 (0.142 g, 0.00103 mol), Sb_2O_3 (1 wt% to the final product) were introduced into a 500 ml glass reactor bottle equipped with a mechanic stirrer and connected to nitrogen flow. The polycondensation was performed in two stages. In the first stage, the mixture was heated under nitrogen atmosphere at 180 °C for 1 hour and then the temperature was gradually increased until 240 °C in the subsequent 2 hours. In the second stage, the pressure was slowly reduced to 0.3 mbar while the temperature was gradually increased up to 270 °C during 3 hours. Finally, the resulting material was collected from the reactor and purified by dissolution in $CHCl_3$ or $CHCl_3$/1,1,1,3,3,3-hexafluoro-2-propanol (HFIP) (80/20 v/v) mixture, filtration of insoluble catalyst and finally precipitation in cold methanol.

The copolymers are named P(EV-*co*-PDL) X/Y, where EV indicates the units derived from methyl 4-(2-hydroxyethoxy)-3-methoxybenzoate and PDL indicates the units derived from ω-pentadecalactone. X/Y is the % molar ratio of EV units and PDL units.

3.2.9.5 Synthesis of poly(ω-pentadecalactone) homopolymer (PPDL)

Poly(ω-pentadecalactone) was synthesized according the study of Focarete et al.[145] ω-pentadecalactone (PDL) (30.0 g, 0.125 mol) and anhydrous *Candida antartica* lipase B CalB (10 wt% to PDL) were introduced under nitrogen atmosphere in a 500 ml round-bottom flask equipped with a magnetic stirrer. Under a constant strain of nitrogen flow, 60 ml of toluene were added and the flask was placed into a constant-temperature (70 °C) oil bath. The mixture was heated for 4 hours under stirring. The reaction was terminated with the addition of an excess of cold chloroform and the removal of the enzymes by filtration on Buchner. Then the solvent was removed under reduced pressure and the remaining concentrated polymer solution was precipitated in cold methanol. The white solid precipitate was isolated by filtration and dried in a vacuum oven (yield 81%).

^{1}H NMR (400 MHz, $CDCl_3/CF_3COOD$, δ): 4.23 (t, J=5.66 Hz, 2H, C^lH_2O), 2.44 (t, J=7.02 Hz, 2H, $C^hH_2C=O$), 1.69 (brs, 4H, C^kH_2, C^iH_2), 1.26-1.52 (brs, 20H, C^jH_2) ppm.

3.2.9.6 Chemical characterization

^{1}H-NMR spectra were recorded at room temperature on samples dissolved in $CDCl_3$ or $CDCl_3/CF_3COOD$ (80/20 v/v) mixture using a Varian Mercury 400 spectrometer, the proton frequency being 400 MHz. The measurements were performed at 25 °C. Chemical shifts (δ) are reported in part per million with reference to chloroform solvent ($CHCl_3$).

Gel permeation chromatography (GPC) measurements were performed at 30 °C by a GPC Knauer Azura equipped with a PL gel 5 µm Minimixed-C column. The instrument worked using chloroform as eluent with a 0.3 mL/min flow; the Refractive Index detector was used and a calibration plot was constructed with monodisperse polystyrene standards. The samples were dissolved in $CHCl_3$ or in a mixture of $CHCl_3$/1,1,1,3,3,3-hexafluoro-2-propanol (HFIP) (95/5 v/v) and filtered on Teflon syringe filter with pore size of 0.45 µm Teflon sieve.

3.2.9.7 Thermal analysis

The thermal stability of the samples was studied by thermogravimetric analysis (TGA) using a PerkinElmer TGA 4000 thermobalance. All measurements were performed under nitrogen atmosphere (gas flow 40 ml min^{-1}) at 10 °C min^{-1} heating rate from 40 °C to 800°C.

The thermal behaviour of the samples was studied by differential scanning calorimetry (DSC) using a Perkin-Elmer DSC8000 calorimeter equipped with an IntraCooler 2 as refrigerating system and calibrated with high purity standards. All measurements were performed under nitrogen atmosphere and using sample masses of approximately 5 mg.

In non-isothermal analyses, the samples were initially heated at 10 °C min^{-1} from 25 °C to different temperatures, varying from 130 °C to 295 °C according to the sample characteristic, and held at high temperature for 2 min to erase thermal history. Then they were cooled to -70 °C at 10 °C min^{-1} and finally heated at the same rate from -70°C to 130-300 °C. During the cooling scan the crystallization temperature (Tc) and the enthalpy of crystallization (ΔHc) were measured. During the 2nd heating scan, the glass transition temperature (Tg), the melting temperature (Tm) and the enthalpy of fusion (ΔHm) were determined.

For PEV sample, Tg was measured during a 2nd heating scan after quenching the molten sample in liquid nitrogen.

In isothermal analyses, the samples were initially heated at 20 °C min^{-1} from 25 °C to 130-300°C according to the sample characteristic, and held at this temperature for 2 min in order to completely destroy any previous crystalline order. Then they were quickly cooled at 150 °C min^{-1} to different crystallization temperatures (Tc). The samples were held at the chosen Tc for the time long enough to complete the crystallization process before heating at 10 °C min^{-1}

to 130-300°C in order to observe the melting process. The isothermal crystallization temperature range was determined by preliminary tests to ensure that no crystallization occurred during the cooling step.

3.2.9.8 Wide angle X-ray scattering analysis

Powder Wide Angle X-ray Scattering (WAXS) measurements were carried out with a X'PertPro diffractometer, equipped with a copper anode (Kα radiation, $\lambda = 1.5418$ Å). The data were collected at room temperature in the 2θ range of 5-60° by means of a X'Celerator detector. The measurements were performed on samples prepared in DSC with the following thermal treatment: 1st heating scan at 10 °C min^{-1} from 25 °C to 130-300 °C according to the sample characteristic and cooling scan at 10 °C min^{-1} to room temperature.

3.2.9.9 Film preparation

The synthesized materials were grinded using an Ika M20 Mill, Staufen, Germany. Resulting powders were dried at 60 °C for 24 hours. The films were obtained using a hydraulic thermo-press Carver, Wabash, Indiana, USA. Dried powder was thermo-molded between two Teflon sheets at a temperature above 5 °C the end melting temperature for 2 min at 10 bar and 2 min at 100 bar. Film was quickly cooled to room temperature between the sheets under pressure by using running water.

3.3 Water vapor barrier properties of bio-based poly(ethylene vanillate), poly(ω-pentadecalactone) and copolymers

3.3.1 Introduction

Investigating the sorption and transport behaviour of water in polymeric materials is crucial for packaging applications, especially in food packaging. Indeed, moisture can have detrimental effects on thermal, mechanical and barrier properties of polymers thus affecting the shelf-life of food.

1) In polymers where the amorphous phase is in the glassy state at room temperature ($Tg>T_{room\ temperature}$), water is known to plasticize the amorphous phase at high water vapor activity resulting in a reduction of glass transition temperature [160] as well as in a degradation of stiffness and strength.[161] Two cases: **a)** At high temperature (near water boiling point) and high water vapor activity, water can hydrolyse polymers with COO, OH, NH groups causing the rupture of the covalent bonds along the polymer backbone.[161,162] This leads to a reduction of molecular weight which can be recorded as glass transition temperature decrement. **b)** At low temperature (close to rt) even at high water vapor activity, such chemical degradation is improbable according to literature and it is more likely that plasticization results from the rupture of the intermolecular weak hydrogen bonds induced by swelling or water clustering.[163] Swelling is associated with the creation of strong water molecules-polymer interactions and a subsequent chain rearrangement while water clustering results from the self-hydrogen bonding of water molecules when absorbed in a polymer since water is a condensable penetrant.

2) In polymers where the amorphous phase is in the rubbery state at room temperature ($Tg<T_{rt}$), water molecules can interact with macromolecular chains *via* hydrogen-bonds favouring swelling or clusters formation. As opposed to glassy polymers, in rubbery polymers swelling or clustering-induced plasticization doesn’t occur since the amorphous phase is above glass transition temperature.

The swelling of the matrix and water clusters can, in turn, impact the diffusion of water vapor through the polymer and increase or decrease, respectively, their diffusion pathways. These effects are more pronounced in polyesters since water shows great interaction with esters groups.

The current chapter provides a detailed investigation of water vapor sorption kinetics in PEV, PPDL and P(EV-*co*-PDL) at 20 °C using a gravimetric method. Since at 20 °C PEV is in a glassy state while PPDL and P(EV-*co*-PDL) in a rubbery state and their behaviour result completely different, the discussion of sorption and transport properties of the investigated polyesters is split in two parts.

In the first part, the water vapor sorption kinetic of both amorphous and semicrystalline PEV films was studied. PEV sorption data were compared to commercial amorphous PET data from the study of Dubelley *et al.*[164] To understand the water sorption mechanism, the isotherms were modelled using a new dual mode sorption model proposed by Feng [165]. This model, based on multilayer sorption theory and assuming the coexistence of dense polymer matrix and unrelaxed microvoids, proves to successfully describe sorption in the investigated glassy polymers. To understand the water transport mechanism, the model proposed by Barens and Hopfeberg [166], which is a combination of Fickian and non-Fickian relaxations, was applied.

In the second part, the water vapor sorption kinetic of PPDL, P(EV-*co*-PDL) 60/40 and P(EV-*co*-PDL) 40/60 was studied. The sorption isotherms were modelled with the Park model which is a combination of Langmuir mode sorption, Henry's law and clusters formation. The water clustering phenomenon was investigated also owing to the ENSIC model. The transport mechanism was described by means of Crank model [167] since all the samples obey Fick's law.

3.3.2 Water vapor barrier properties of poly(ethylene vanillate)

3.3.2.1 Chemical structure and thermal transitions

The chemical structure of poly(ethylene vanillate) (Figure 3.3. 1a) is characterized by a *para*-substitute aromatic ring bonded to a carboxylic group from one side and to an ether group from the other. The benzoate structure presents also a methoxy group. The PEV chemical structure differs from that of PET (Figure 3.3. 1b) in the substitution of a carboxyl group with an ether one and in the presence of an additional methoxy group.

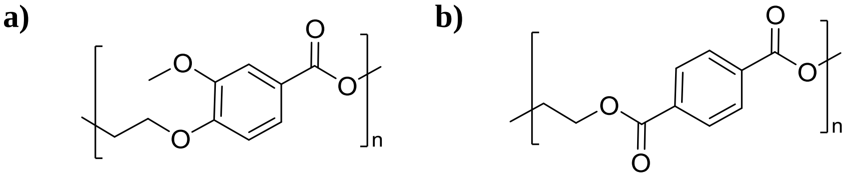

Figure 3.3. 1: Chemical structures of **a)** poly(ethylene vanillate) (PEV) and **b)** poly(ethylene terephthalate) (PET).

As far as thermal behavior is concerned, PEV is characterized by a glass transition temperature (Tg) of 75 °C and a melting temperature (Tm) of 266 °C, as observed in chapter 3.2. The thermal transition values are close to those of PET (Tg = 76 °C and Tm = 247 °C [136,168]), but PEV demonstrates to crystallize faster and to reach a state of high order, as observed by isothermal crystallization in paragraph 3.2.6. As stated by Gioia *et al.*[134] such behavior can be justified by considering a higher mobility of the constituent units of the PEV chain with respect to the terephthalic units of PET. Indeed, in terephthalic units the sp^2 hybridization of the carbon atoms of the two carboxylic groups induces coplanarity between carboxyl and phenyl groups, restricting the rotational angles of Cphenyl-COO to 0 and 180°. In PEV such rigidity is avoided because one carboxylic group is substituted by an ether unit, resulting in enhanced chain flexibility and hence higher chain folding capability.

3.3.2.2 Films crystallinity

The structural state of amorphous and semicrystalline poly(ethylene vanillate) films was determined by Differential Scanning Calorimetry (DSC) and Wide Angle X-ray Scattering (WAXS) analyses.

The 1st DSC heating scan of the quenched PEV film, obtained by melt-quenching in liquid nitrogen, is reported in Figure 3.3. 2. It is notable that the enthalpy of cold crystallization at 104 °C is quite identical to the enthalpy of melting at 271 °C, indicating that the film is in a completely amorphous state ($\Delta Hcc = \Delta Hm = 75\ J\ g^{-1}$). A second film of PEV was not quenched after compression-molding and the 1st DSC heating scan is reported in Figure 3.3. 2. The sample presents a single melting peak at 269 °C with a $\Delta Hm = 108.3\ J\ g^{-1}$. By DSC analysis, the degree of crystallinity of the film is calculated as follows:

$$X_c\ (\%) = \frac{\Delta H_m}{\Delta H_m^{\circ}} \times 100 \qquad (3.3.\ 1)$$

where ΔH_m is the experimental melting enthalpy measured during the 1st heating ramp ($J\ g^{-1}$) and $\Delta H_m°$ the theoretical melting enthalpy of a corresponding 100% crystalline sample. A value of $\Delta H_m° = 166\ J\ g^{-1}$ was used according to the study of Zamboulis *et al.*[157] Therefore, from DSC analysis, the crystallinity turned out to be 65% confirming the ability of PEV to reach a high degree of order. The crystallinity of the film was also calculated by WAXS analysis, whose spectrum is reported in Figure 3.3. 3, together with the amorphous sample scattering profile. The degree of crystallinity was determined according to the formula:

$$X_c\ (\%) = \frac{I_c}{I_c + I_a} \times 100 \qquad (3.3.\ 2)$$

where *Ic* and *Ia* are the intensities of X-rays scattered from the crystalline and the amorphous phases, respectively. The intensity of X-rays scattered from the crystalline regions of a specimen is proportional to the area under the sharp peaks of the spectrum, while the intensity of radiation scattered from the amorphous regions is proportional to the background area which underlines the crystalline peaks. The intensity of radiation scattered from the entire sample (*Ic* + *Ia*) is proportional to the total area under the curve.[169] According to WAXS analysis, the degree of crystallinity is 60%. The value is quite close to the one calculated by DSC analysis.

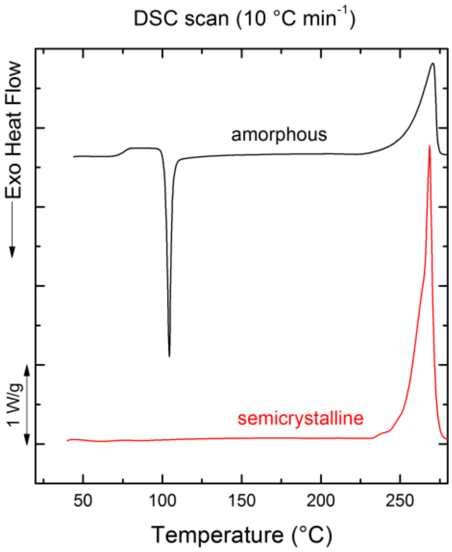

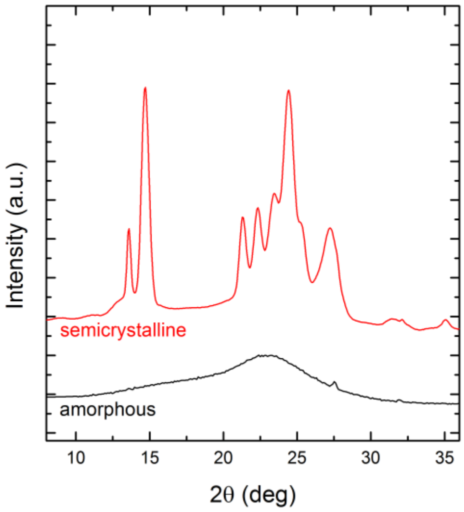

Figure 3.3. 2: DSC 1st heating scans at 10 °C min^{-1} for amorphous and semicrystalline PEV films.

Figure 3.3. 3: Wide angle X-ray scattering pattern of amorphous and semicrystalline PEV films.

3.3.2.3 Sorption measurements

The gravimetric water vapor sorption kinetic measurements on amorphous and semicrystalline PEV films were performed using a Dynamic Vapor Sorption (DVS) system at 20 °C over a wide range of relative humidity: from 0 to 95% in increments of 10% up to 90% and 5% for the last point, then followed by desorption measurements from 95 to 0% in same increments. Each RH% step lasted 12 hours. Examples of raw kinetic measurements are provided in Figure 3.3. 4 and Figure 3.3. 5 for amorphous and semicrystalline PEV respectively.

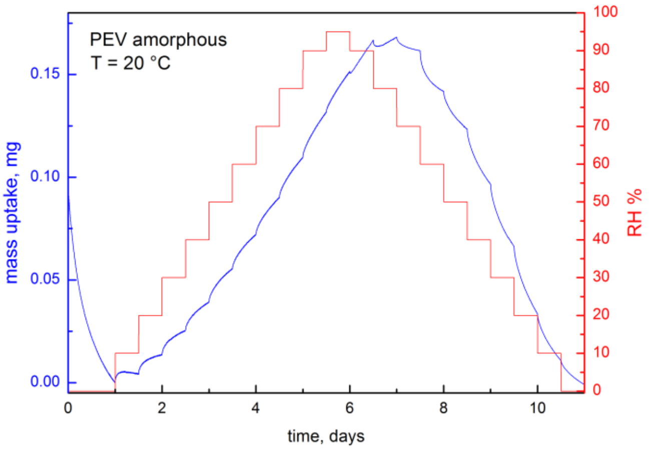

Figure 3.3. 4: Example of gravimetric water vapor sorption/desorption kinetic measurements of amorphous PEV (all measurements carried out at 20 °C).

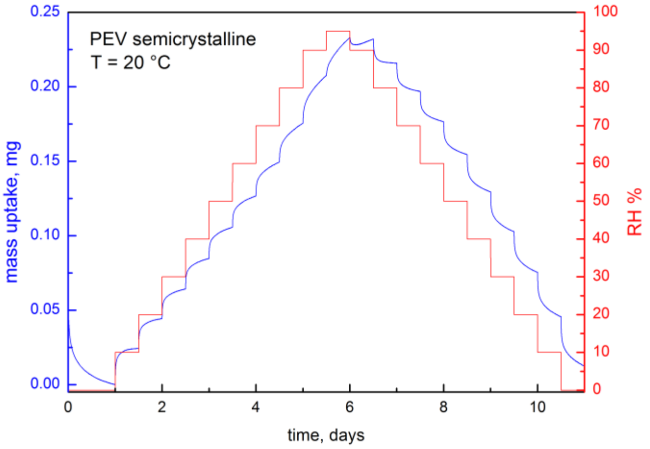

Figure 3.3. 5: Example of gravimetric water vapor sorption/desorption kinetic measurements of semicrystalline PEV (all measurements carried out at 20 °C).

Figure 3.3. 6 and Figure 3.3. 7 show an excerpt of sorption kinetic at 10, 20 and 60% RH for amorphous and semicrystalline PEV, respectively. At RH 10% and 20% (curves A and B in Figure 3.3. 6 and Figure 3.3. 7) the mass reaches the equilibrium after 12 hours in both samples. This behavior relates to the random motion of vapor molecules without interaction with the polymer matrix: the water diffusion through the polymer is faster than water-polymer interactions and relaxation of the matrix, as Fickian type sorption provide. On the contrary, at RH 60%, the mass equilibrium is not reached even after 12 hours of exposition as shown by curve C in both figures.

In order to investigate time-dependence at high water vapor activity a_w, an extra experiment was conducted at constant temperature and RH (60%) by varying the time step.

Both semicrystalline and amorphous PEV films were exposed at 20 °C to the following RH% profile: from 50% to 60% RH for 12 h and 24 h time duration (Figure 3.3. 8). As shown, all the curves exhibit a mass drift, and the mass equilibrium is not reached even after 24 hours of exposition at RH = 60%. This behavior has been largely described for glassy polymers in contact with condensed vapor and it was assigned to long-term non-Fickian relaxations of the polymer matrix causing an extra water vapor uptake without ever reaching mass equilibrium.

For example, poly(ethylene terephthalate) shows this drift of sorption curve at high water vapor activity (above $a_w = 0.6$) even at low temperature.[164,170] Several authors associated these relaxations in glassy polymers to morphological changes such as plasticization [171,172] and free volume increase.[170]

Since at low temperature, the hydrolytic degradation of the covalent bonds is improbable, the authors associated free volume increase and plasticization to swelling of the polymer matrix.

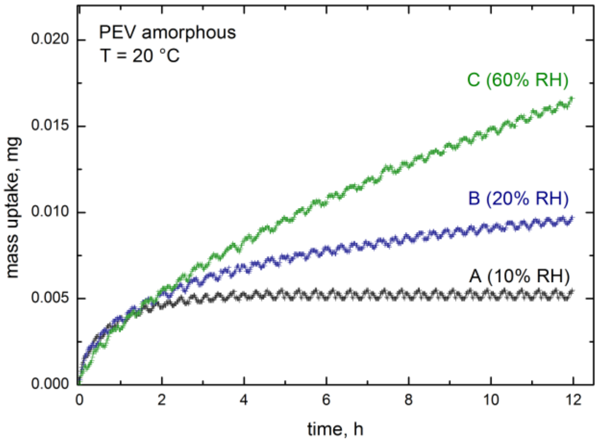

Figure 3.3. 6: Water vapor sorption kinetic of amorphous PEV at 20 °C and different relative humidity (10, 20, 60%). The time step is maintained constant at 12 hours.

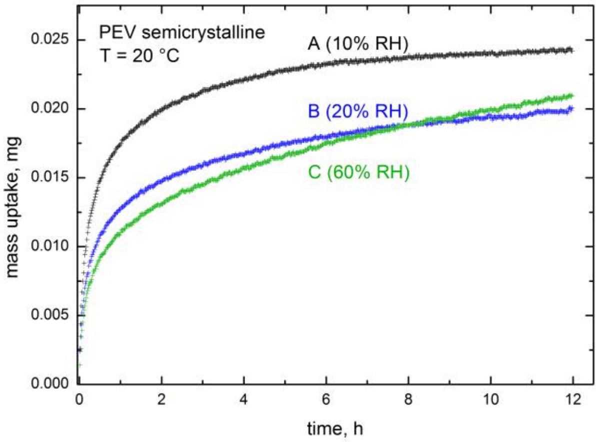

Figure 3.3. 7: Water vapor sorption kinetic of semicrystalline PEV at 20 °C and different relative humidity (10, 20, 60%). The time step is maintained constant at 12 hours.

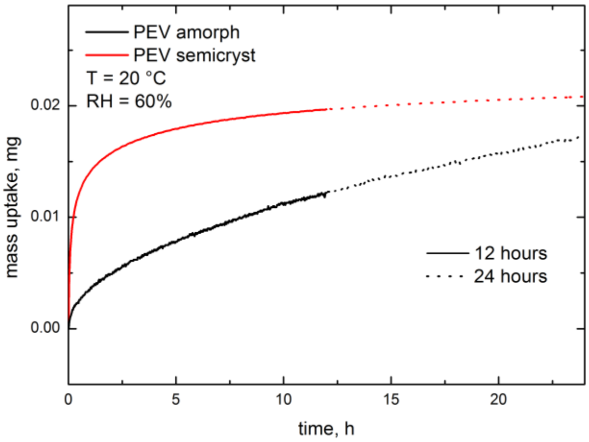

Figure 3.3. 8: Water vapor sorption kinetic of amorphous and semicrystalline PEV at 20 °C and RH 60% for increasing the time step: 12 and 24 hours.

3.3.2.4 Sorption isotherms

Water vapor sorption isotherms were determined from the water vapor pseudo-equilibrium content at each RH% step. At each sorption measurement conducted by varying the RH%, steady state must be reached for a correct interpretation of the sorption isotherm. Nevertheless, as discussed in the previous paragraph, mass equilibrium could not be achieved at high relative humidity because of the presence of non-Fickian relaxations. For semicrystalline PEV, relaxation is dominant from RH = 60% while for amorphous PEV, sorption measurements have time-dependence from RH = 50%. As in the previous work of Barens *et al.*[166], we considered that determination of the true equilibrium is impracticable even increasing the step time duration and that the differences between the pseudo-equilibrium and the true equilibrium were minor due to the small “extra” non-Fickian relaxations; therefore all sorption measurements were stopped after 12 hours of exposition.

Water vapor sorption isotherms of amorphous and semicrystalline PEV films in the water activity range between 0 and 0.95 at 20 °C are shown in Figure 3.3. 9 (black and red full circles respectively). In the same Figure the sorption isotherm of commercial amorphous PET from the study of Dubelley *et al.*[164] is reported in the water activity range between 0 and 0.90 at 23 °C (blue full circles). As shown, the sorption isotherms of PEV and PET are arranged in the same concentration range, proving the similarity of the two polyesters.

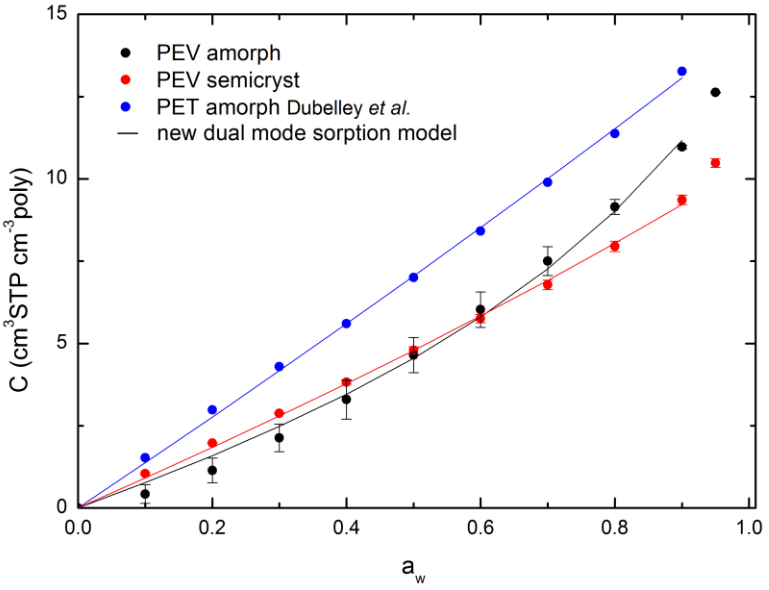

Figure 3.3. 9: Water vapor sorption isotherms of amorpohous (●) and semicrystalline (●) poly(ethylene vanillate) (PEV) at 20 °C (two replicates for each point). Water vapor sorption isotherm of amorphous PET (●) at 23 °C from the study of Dubelley *et al.*[164] The solid lines represent the new dual mode sorption model fitting in the a_w range 0-0.9.

The isotherm curves of semicrystalline PEV and amorphous PET are rather linear on the a_W range between 0 and 0.6 with a slight upturn for $a_W > 0.6$. At low activity ($a_W < 0.2$) a concavity in the curve ascribable to the Langmuir mode sorption is generally observed in glassy polymers: water molecules occupy specific sites (frozen microvoids) in the polymer and water-polymer interactions would predominate .[173] However, this concavity is difficult to observe in the case of semicrystalline PEV and amorphous PET. Between 0.2 and 0.6, a linear relation ($r^2 = 0.999$ for semicrystalline PEV, $r^2 = 0.998$ for amorphous PET) between the water concentration in the polymer and the water activity is noticed: the system water/polymer follows Henry’s law. In that later case, the penetrant is randomly dispersed in the matrix and polymer-polymer interactions are favoured.[174,175] At high activity ($a_W > 0.6$) the curve registers an upturn: the water-polymer interactions become stronger, especially for semicrystalline PEV, for which this upturn is much more pronounced than for amorphous PET. Contrary to semicrystalline PEV and amorphous PET, the isotherm curve of amorphous PEV is rather convex to the water activity axis on the entire a_w range indicating stronger water-polymer interactions. The upturn in the curve is also observed for $a_w > 0.6$. The upward of the curves recorded at high a_w was already observed by some studies on PET and it has been related to swelling. Therefore, it can be supposed that, for both amorphous and semicrystalline PEV, non-Fickian relaxations observed at high activity would result from swelling-induced plasticization of the polymer matrix. This should be confirmed by a deepened analysis of the diffusion phenomenon in the polymer.

To describe the sorption isotherm behavior and determine the sorption parameters there are several mathematical models. In glassy polymers, the conventional dual mode sorption model (CDMS), which is a combination of Langmuir mode sorption and Henry's law, is largely applied to describe sorption isotherms at low water vapor activity until the isotherm exhibits concavity to activity axis. However, the CDMS cannot effectively describe convex and sigmoidal sorption isotherms and it is inconsistent with the aim of the present work. On the other hand, Guggenheim-Anderson-de Boer (GAB) model fits extremely well sigmoidal isotherms but the assumption of this model that all the sorption sites are equivalent is inconsistent with glassy polymers which are considered to have two species of sorption sites as the CDMS assumes: i) the dense polymer matrix ii) the non-equilibrium unrelaxed microvoids frozen in the glassy state.

Based on a multilayer sorption theory on which the GAB equation is based and assuming the coexistence of two different sorption sites as the CDMS does, Feng [165] proposed a new dual mode sorption model for water vapor sorption in glassy polymer able to describe concave, convex and sigmoidal isotherms. According to Feng [165], the sorbate concentration in the polymer is given as:

$$C = C_p \frac{k'a}{1 - k'a} + C_p \frac{(A' - 1)k'a}{1 + (A' - 1)k'a} \qquad (3.3.\ 3)$$

where a is the water vapor activity, C_p is the weighted mean value of the sorption capacity of a polymer to water; k' is the ratio of the partition function of water vapor molecules sorbed in the multilayer (water-polymer interaction) to that of molecules in bulk liquid (water-water interaction); A' is the ratio of the partition function of the first water vapor molecule sorbed on a microvoid to that of molecules sorbed beyond the first molecule in the multilayer. According to the assumption of the model, the interaction of a microvoid and the water molecules sorbed beyond the first molecule are equal to those of water-polymer. Therefore, A’ is a measure of the interaction of the water vapor molecule and a microvoid (water-micovoid interaction).

In the present work, the new dual mode sorption model is applied to amorphous and semicrystalline PEV and amorphous PET [164] sorption isotherms in the water activity range 0-0.90. Figure 3.3. 9 shows the new dual mode sorption model fitting and Table 3.3. 1 lists the three parameters C_p, k’ and A’ of the model. A very good fitting of experimental sorption data was obtained for amorphous PET and semicrystalline PEV with very low root mean square error (RMSE) value (less than 0.05 cm^3 STP cm^{-3} poly) while a less good fitting but still acceptable, was obtained for amorphous PEV (RMSE value of 0.28 cm^3 STP cm^{-3} poly). Therefore, the sorption curves of semicrystalline PEV and amorphous PET are well fitted by the new dual mode sorption model confirming that, even if obviously almost linear, the curves rather display a sigmoidal pattern

Table 3.3. 1: Sorption parameters Cp, k’, A’ of amorphous and semicrystalline PEV and amorphous PET polyesters at 20 °C according to the new dual mode sorption model.

sample	a_w range	Cp (cm^3 STP cm^{-3} poly)	k’	A’	RMSE (cm^3 STP cm^{-3} poly)
PEV amorph.	0-0.9	7.757	0.605	1.501	0.282
PEV cryst.	0-0.9	6.661	0.528	3.087	0.029
PET Dubelley	0-0.9	10.161	0.496	3.217	0.049

The parameter C_p (cm^3 STP cm^{-3} poly) follows the order amorphous PET > amorphous PEV > semicrystalline PEV confirming that PET has higher sorption capacity than both amorphous and semicrystalline PEV samples. It is well known that water molecules interact with carboxylic groups on the polyester backbone *via* hydrogen-bonding and the lower sorption capacity of PEV can be related to the carboxylic groups’ concentration in the polymer backbone which is lower for PEV than PET because of the substitution of one carboxylic group with an ether group from one side. The increased sorption capacity of amorphous PEV than semicrystalline PEV was expected since crystallites act as impermeable particles in the polymer matrix.

The parameter k’ respects the trend: amorphous PEV > semicrystalline PEV > amorphous PET. The mathematical meaning of k’ is to describe the departure from linearity of the isotherm curve. Greater the upturn at high water activity, larger the value of k’ meaning stronger interactions water-polymer. As previously discussed, at high water vapor activity swelling-induced plasticization of the polymer matrix is hypothesized and according to the new dual mode sorption model, k’ value is an indication of the interactions water molecules-polymer which lead to such phenomenon. By comparing amorphous and semicrystalline PEV samples, the parameter k' is higher for amorphous PEV, meaning that, in semicrystalline PEV, the water-polymer interactions responsible for swelling are less important than in amorphous PEV. Since swelling occurs in the amorphous phase, this result was expected. Moreover, PEV demonstrates to have higher k' value than PET, meaning that chain rearrangement is more pronounced in the new bio-based aromatic polyester.

Finally, the parameter A' ≠ 1 for all the samples, confirming that the polyesters contain microvoids and thus are in their glassy state.

3.3.2.5 Hysteresis

Sorption hysteresis occurs when the penetrant sorption and the subsequent desorption cycles do not superimposes and can occur in a wide variety of penetrant-material combinations. Very often, hysteresis is linked to swelling of the polymer matrix, where the chains irreversibly relax because of the rupture of intermolecular hydrogen bonds and incorporate extra penetrant at high concentration.[176,177] Figure 3.3. 10 shows that water uptake in amorphous and semicrystalline PEV exhibits hysteresis between sorption and subsequent desorption cycles. This behavior correlates with the upturn in concentration *vs* activity of the sorption isotherm (Figure 3.3. 9) and the presence of non-Fickian relaxations and demonstrates the occurrence of morphological changes in the polymer matrix because of the swelling-induced plasticization.

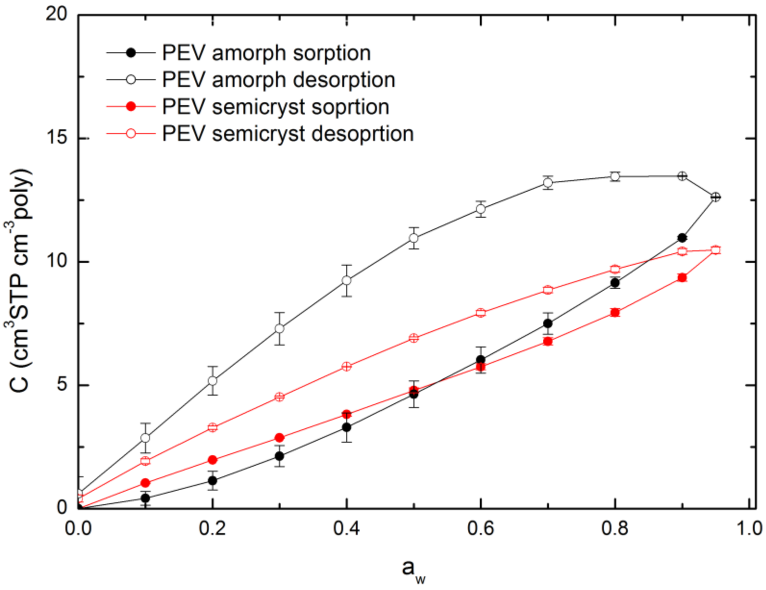

Figure 3.3. 10: Sorption hysteresis at 20 °C for amorphous and semicrystalline PEV (two replicates for each point). Lines are drawn to aid the eye and do not represents model fits.

Hysteresis is much more important for amorphous PEV than for semicrystalline PEV, confirming the higher swelling of the polymer matrix in such a sample film. The present observation will be deeply discussed in diffusivity chapter (3.3.2.6).

3.3.2.6 Diffusivity

Water vapor diffusivity values were estimated for each relative humidity step from individual kinetic gravimetric water vapor uptake measurements.

Since both Fickian diffusion and relaxation processes occur, the analytical solution proposed by Barens and Hopfenberg [166] (BH) was applied to experimental data for extracting diffusivity values.

The BH model is:

$$\frac{m_t}{m_\infty}\Big|_{BH} = \left[\phi\left(1-\sum_{n=0}^{\infty}\frac{8}{(2n+1)^2\pi^2}exp\left(-\frac{D\,(2n+1)^2\pi^2 t}{L^2}\right)\right)+(1-\phi)\left(1-exp\left(-\frac{1}{\tau_R}\right)\right)\right] \qquad (3.3.\ 4)$$

where m_t denotes the water uptake at time t, m_∞ denotes the water uptake after infinite time represented by equilibrium, D ($m^2\ s^{-1}$) is the Fickian diffusion coefficient, φ is a weighting factor that ranges from 0 to 1 and specifies the relative Fickian (φ = 1) and relaxation (φ = 0) contributions and τ_R (s) is the time constant for the non-Fickian relaxations.

Individual kinetic sorption/desorption uptake curves for each relative humidity step are provided in Figure 3.3. 11 for amorphous PEV and in Figure 3.3. 12 for semicrystalline PEV. The red lines labelled as “calculated” represent the BH model fits from Equation 3.3. 4 while the experimental data are reported in blue. For amorphous PEV, the BH model fits well the kinetic curves at low water vapor activity while at high a_w the model doesn’t describe very accurately the experimental data but still acceptable (averaged RMSE = 1.08×10^{-8} mg over the entire a_w interval). For semicrystalline PEV, the BH model fits well all the kinetic curves (RMSE = 0.79×10^{-8} mg). The kinetic curves for whose the fitting is unacceptable have not been considered for diffusivity determination. The parameters obtained from the BH model fit to the kinetic sorption/desorption curves of amorphous and semicrystalline PEV are plotted in Figure 3.3. 13, Figure 3.3. 14 and Figure 3.3. 15.

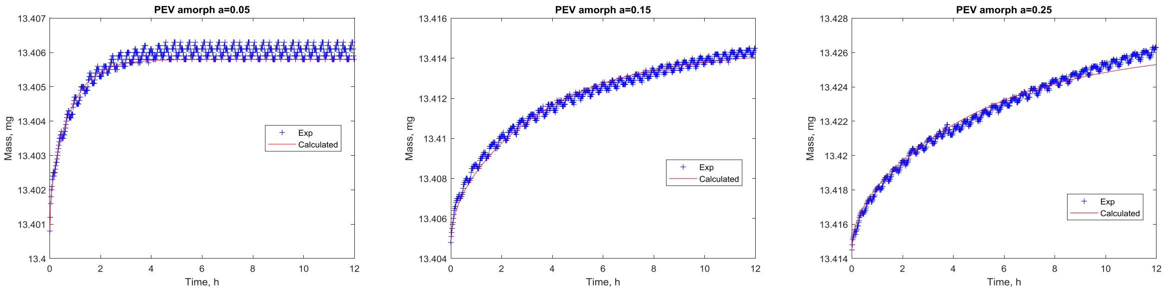

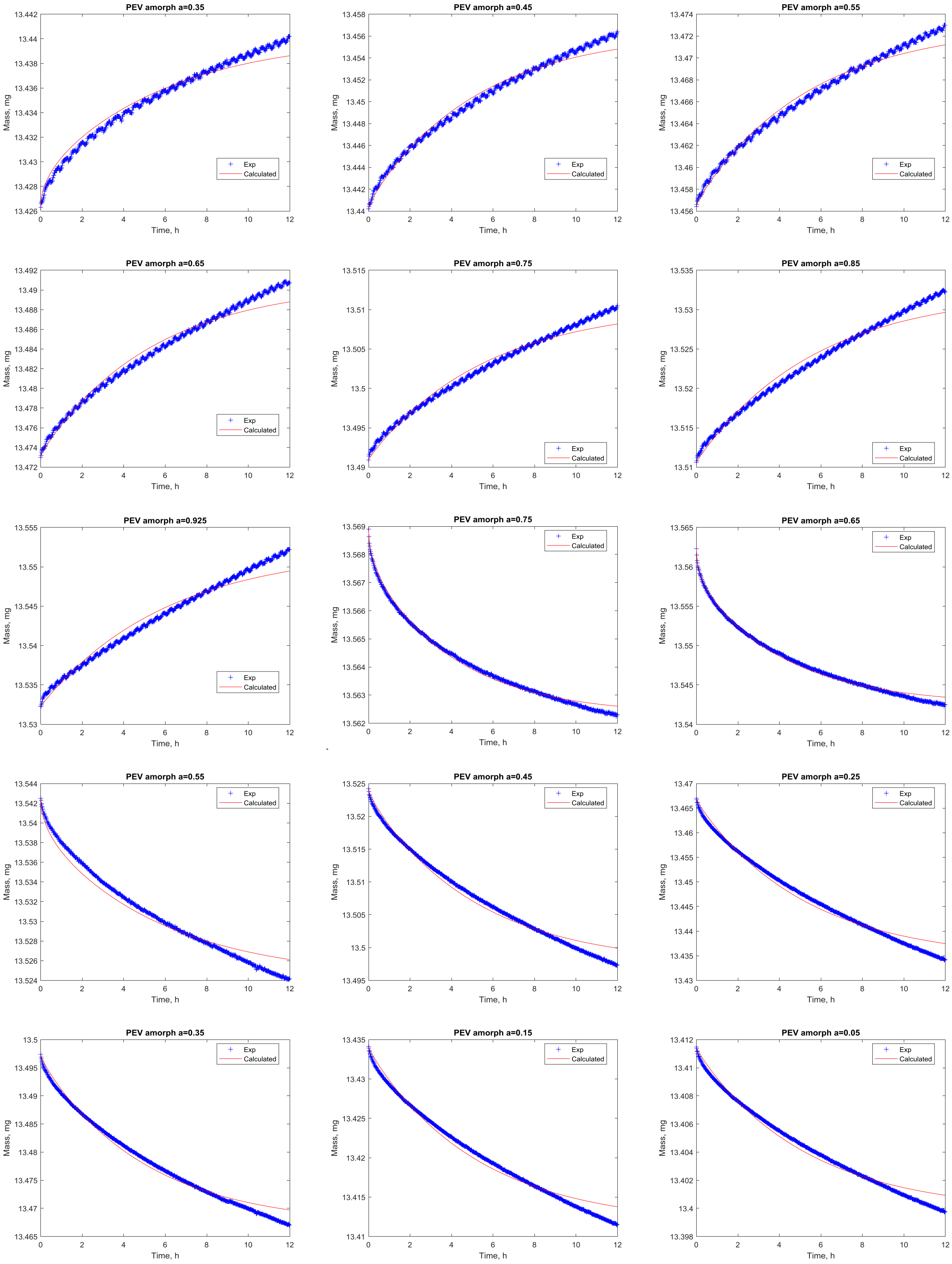

Figure 3.3. 11: Kinetic sorption/desorption data for water vapor on amorphous PEV at 20 °C measured by DVS. Red lines represent model fits from Equation 3.3. 4 while experimental data are represented in blue. The sorption intervals are labelled in each respective graph.

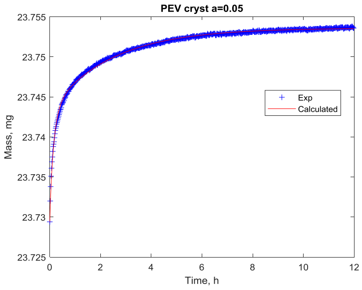
PEV cryst a=0.05
Mass, mg
Time, h
23.755
23.75
23.745
23.74
23.735
23.73
23.725
0
2
4
6
8
10
12
Exp
Calculated

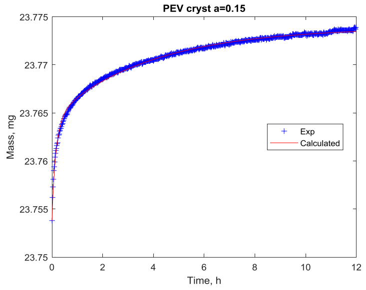
PEV cryst a=0.15
Mass, mg
Time, h
23.775
23.77
23.765
23.76
23.755
23.75
0
2
4
6
8
10
12
Exp
Calculated

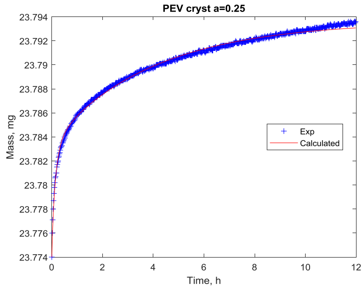
PEV cryst a=0.25
Mass, mg
Time, h
23.794
23.792
23.79
23.788
23.786
23.784
23.782
23.78
23.778
23.776
23.774
0
2
4
6
8
10
12
Exp
Calculated

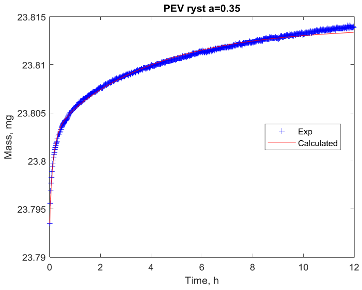
PEV ryst a=0.35
Mass, mg
Time, h
23.815
23.81
23.805
23.8
23.795
23.79
0
2
4
6
8
10
12
Exp
Calculated

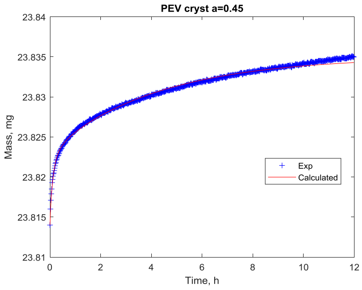
PEV cryst a=0.45
Mass, mg
Time, h
23.84
23.835
23.83
23.825
23.82
23.815
23.81
0
2
4
6
8
10
12
Exp
Calculated

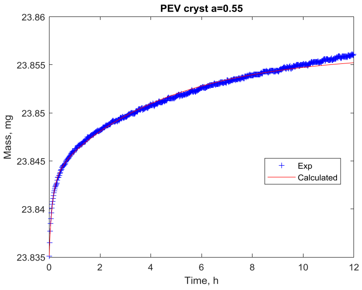
PEV cryst a=0.55
Mass, mg
Time, h
23.86
23.855
23.85
23.845
23.84
23.835
0
2
4
6
8
10
12
Exp
Calculated

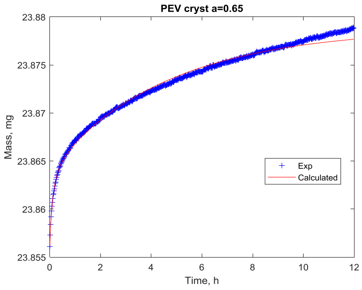
PEV cryst a=0.65
Mass, mg
Time, h
23.88
23.875
23.87
23.865
23.86
23.855
0
2
4
6
8
10
12
Exp
Calculated

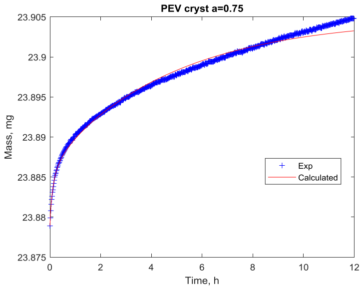
PEV cryst a=0.75
Mass, mg
Time, h
23.905
23.9
23.895
23.89
23.885
23.88
23.875
0
2
4
6
8
10
12
Exp
Calculated

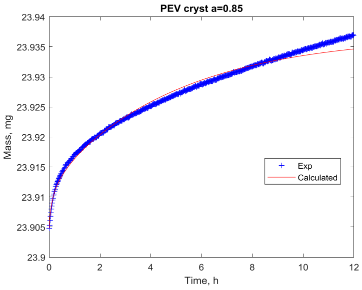
PEV cryst a=0.85
Mass, mg
Time, h
23.94
23.935
23.93
23.925
23.92
23.915
23.91
23.905
23.9
0
2
4
6
8
10
12
Exp
Calculated

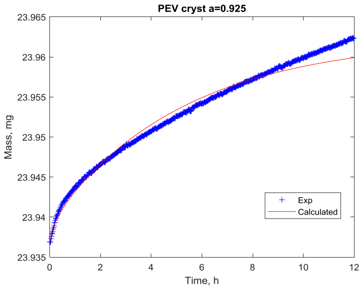
PEV cryst a=0.925
Mass, mg
Time, h
23.965
23.96
23.955
23.95
23.945
23.94
23.935
0
2
4
6
8
10
12
Exp
Calculated

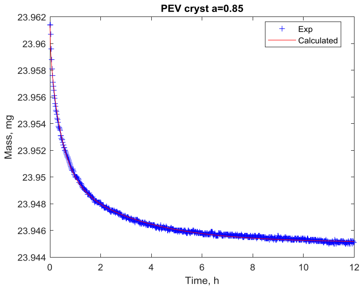
PEV cryst a=0.85
Mass, mg
Time, h
23.962
23.96
23.958
23.956
23.954
23.952
23.95
23.948
23.946
23.944
0
2
4
6
8
10
12
Exp
Calculated

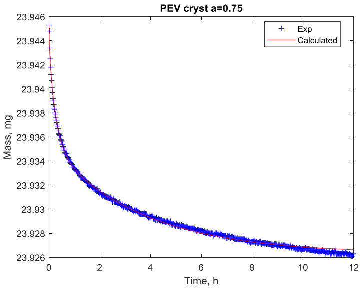
PEV cryst a=0.75
Mass, mg
Time, h
23.946
23.944
23.942
23.94
23.938
23.936
23.934
23.932
23.93
23.928
23.926
0
2
4
6
8
10
12
Exp
Calculated

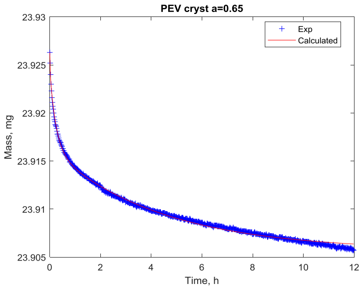
PEV cryst a=0.65
Mass, mg
Time, h
23.93
23.925
23.92
23.915
23.91
23.905
0
2
4
6
8
10
12
Exp
Calculated

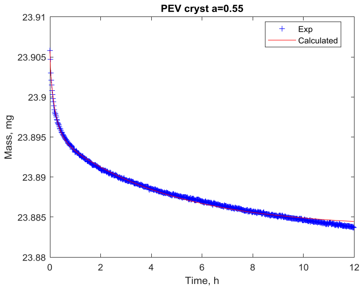
PEV cryst a=0.55
Mass, mg
Time, h
23.91
23.905
23.9
23.895
23.89
23.885
23.88
0
2
4
6
8
10
12
Exp
Calculated

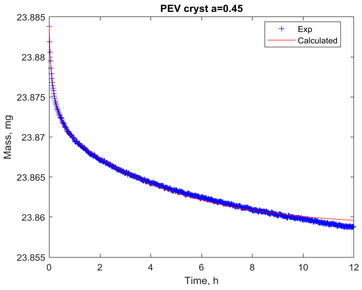
PEV cryst a=0.45
Mass, mg
Time, h
23.885
23.88
23.875
23.87
23.865
23.86
23.855
0
2
4
6
8
10
12
Exp
Calculated

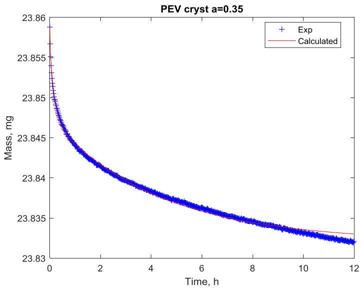
PEV cryst a=0.35
Mass, mg
Time, h
23.86
23.855
23.85
23.845
23.84
23.835
23.83
0
2
4
6
8
10
12
Exp
Calculated

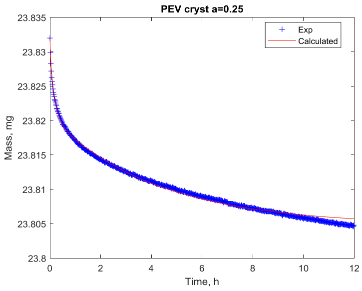
PEV cryst a=0.25
Mass, mg
Time, h
23.835
23.83
23.825
23.82
23.815
23.81
23.805
23.8
0
2
4
6
8
10
12
Exp
Calculated

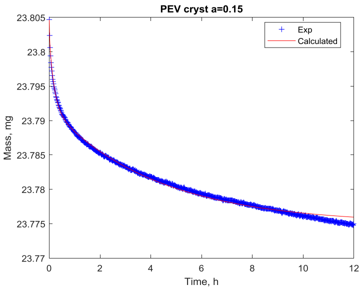
PEV cryst a=0.15
Mass, mg
Time, h
23.805
23.8
23.795
23.79
23.785
23.78
23.775
23.77
0
2
4
6
8
10
12
Exp
Calculated

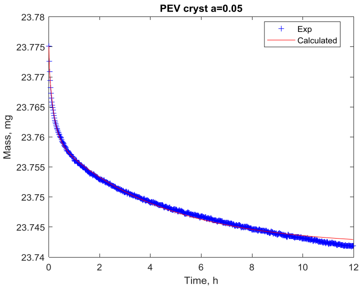

Figure 3.3. 12: Kinetic sorption/desorption data for water vapor on semicrystalline PEV at 20 °C measured by DVS. Red lines represent model fits from Equation 3.3. 4 while experimental data are represented in blue. The sorption intervals are labelled in each respective graph.

Since D is an overall mass transport phenomenon that does not only represent Fick's diffusion, but all the different water transport mechanism occurring in the material, D is conceived as an apparent or effective diffusivity, noted as D_{eff} in the following. D_{eff} is considered constant for the RH step considered, therefore D_{eff} values are plotted at the midpoint of the respective RH step intervals.

Effective diffusion coefficients (D_{eff}) obtained from the BH model fit (equation 3.3. 4) to the kinetic sorption/desorption curves for amorphous PEV and semicrystalline PEV of Figure 3.3. 11 and Figure 3.3. 12 respectively, are plotted in Figure 3.3. 13.

In spite of few variations, it may be considered that diffusivity remains constant over the entire water vapor activity range investigated. In addition, the values for sorption and desorption are similar in magnitude. Therefore, an average diffusivity value was calculated over the entire water vapor activity range investigated: 4.0×10^{-10} m^2 s^{-1} for semicrystalline PEV and 1.0×10^{-11} m^2 s^{-1} for amorphous PEV.

Semicrystalline PEV shows a D_{eff} value significantly higher than amorphous PEV and the explication has to be found in the different degree of crystallinity. In semicrystalline polymers, the crystalline regions act as impermeable barriers analogous of filler particles. However, in highly crystalline materials the permeable amorphous phase is trapped in between a crystal and the near one and thus, the interface amorphous/crystalline constitutes a considerable fraction of the sample. Bastioli *et al.*[161] reported how water sorption in the amorphous phase of a semicrystalline polymer can produce stress at the amorphous/crystalline interface, followed by "microvoids" formation that might favour water diffusion and this is the case of semicrystalline PEV (Xc = 60%).

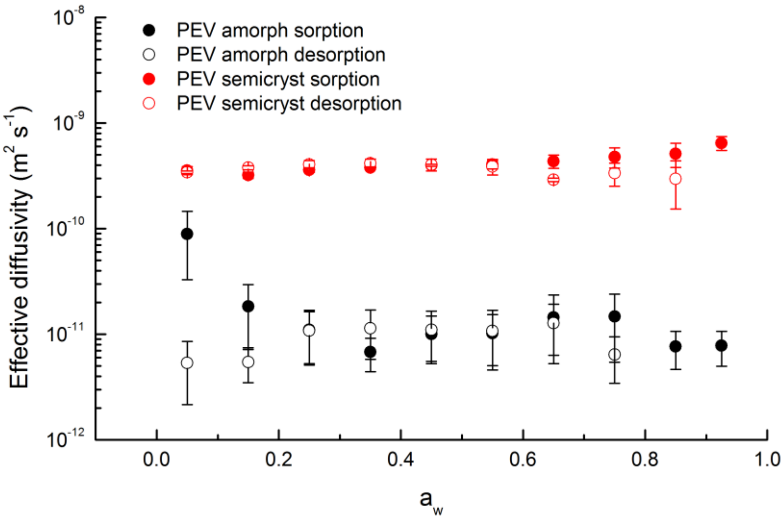

Figure 3.3. 13: Effective water vapor diffusivity (D_{eff}) at 20 °C in amorphous (●) and semicrystalline (●) PEV determined from BH model (two replicates for each point). Sorption and subsequent desorption values are plotted at the midpoint activity of the respective sorption interval.

As concerns amorphous PEV, it exhibits an average D_{eff} value of 1.0×10^{-11} m^2 s^{-1} across the entire concentration range. The D_{eff} value of amorphous PEV is higher than D_{eff} value of amorphous PET reported in literature. Dubelley *et al.*[164] determined a value of D_{eff} equal to 6.1×10^{-13} m^2 s^{-1} for water diffusion at 23 °C after a correction of swelling on amorphous PET by Rexor; Burgess *et al.*[170] observed an average D_{eff} value of 1.5×10^{-12} m^2 s^{-1} at 35 °C by using the BH model on amorphous PET supplied by Coca-Cola.

By comparing PEV and PET chemical structures, PEV aromatic ring is less sterically hindered by the presence of an ether group from one side rather than two carboxylic groups as for PET. As a consequence, the aromatic ring has a greater range of rotation that leads to an enhanced segmental flexibility of the chain which can result in favoured chain rearrangement when water molecules are absorbed. The greater diffusion coefficient for PEV, compared to PET, originates from the inherent differences in segmental mobility.

A plot of parameter φ, which is a weighting factor that specifies the relative Fickian (φ = 1) and relaxation (φ = 0) contributions, *vs* water activity is provided in Figure 3.3. 14 for both amorphous and semicrystalline PEV.

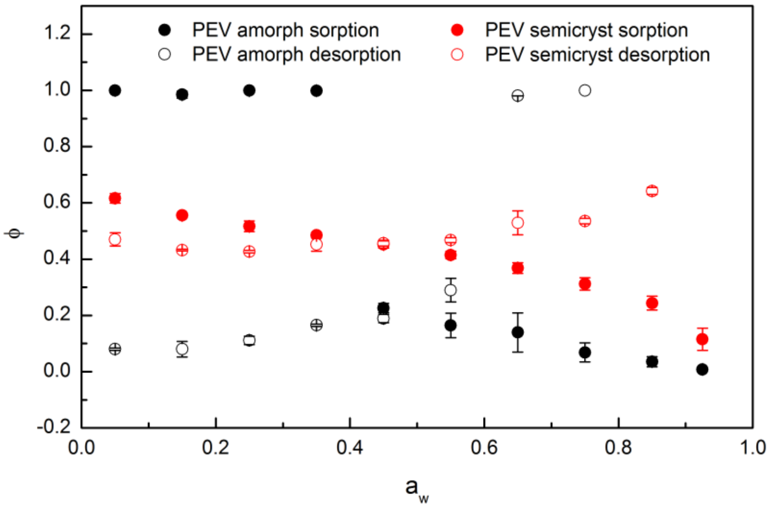

Figure 3.3. 14: Plot of φ from BH model for water vapor at 20 °C in amorphous (●) and semicrystalline (●) PEV for sorption and desorption (two replicates for each point).

For semicrystalline PEV in sorption mode, the contribution ascribable to relaxation process is evident for the entire a_W range, even at low water vapor activity (φ always < 1) and the inversion from Fickian-dominated to relaxation-dominated process occurs at 0.55 of water activity. However, after 0.55 of water activity, the contribution of the relaxation-dominated process, even predominant, remains low (φ about 0.4/0.5 except for $a_W > 0.85$). The parameter φ of amorphous PEV levelled off at 1 in sorption mode until $a_W = 0.35$, then drops suddenly below 0.2 and stays low up to $a_W = 0.925$. At $a_W < 0.35$, the diffusion in amorphous PEV is clearly Fickian and quickly reversed to pure relaxation mechanism after 0.35. This trend is close to those of amorphous PET and PEF at 35 °C as observed by Burgess *et al.*[170] However, for both PET and PEF, the inversion from Fickian to relaxation occurs at 0.6 instead of 0.35 water activity, meaning that PEV would start relaxing at lower a_W. The rotation of the aromatic ring and the presence of the lateral methoxy group determine an enhanced segmental mobility of the PEV polymer backbone, which results in favoured chain rearrangement when water molecules are absorbed. In semicrystalline PEV, the relaxation phenomenon is evident even at low water vapor activity because the absorption of water occurs in the rigid amorphous phase, which is the amorphous region trapped in between a crystal and the near one.[178] As demonstrated by Lin *et al.*[179], this rigid amorphous fraction surrounding the crystallites is less dense than the core of the amorphous phase, resulting in enhanced sorption capability and the eased rupture of intermolecular hydrogen bonds. Nevertheless, above 0.55 activity, the φ value remains higher for semicrystalline than for amorphous PEV because the volume fraction occupied by crystallites remains unaffected during the entire sorption process and the relaxation is ascribed only to the amorphous phase. The lower the volume fraction of the amorphous phase, the lower the impact of plasticization over the sample. As concerns desorption, for semicrystalline PEV, Fickian diffusion is dominant during the entire activity range, since $\varphi \geq 0.5$, while for amorphous PEV, Fickian diffusion is dominant until 0.65 activity; afterwards, relaxation-dominated processes predominant. In desorption mode, the protracted approach to equilibrium, recorded as $\varphi \neq 1$, can result from the collapse of extra free-volume introduced during sorption, as observed by Barens *et al.*[180] in the case of vinyl chloride sorption in poly(vinyl chloride).

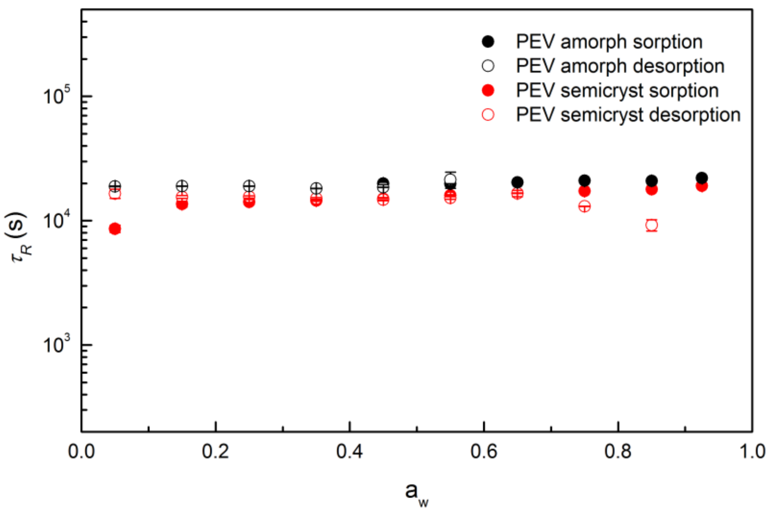

Figure 3.3. 15: Plot of τ_R from BH model for water vapor at 20 °C in amorphous (●) and semicrystalline (●) PEV for sorption and desorption (two replicates for each point).

The plot of τ_R *vs* activity is provided in Figure 3.3. 15 for both amorphous and semicrystalline PEV. The parameter τ_R is determined accurately for the kinetic uptake curves for whose φ is far from 1. Consequently, Figure 3.3. 15 only reports τ_R values in conjunction with the respective φ parameters represented in Figure 3.3. 14.

Both amorphous and semicrystalline PEV samples exhibit similar relaxation rates despite their different degree of crystallinity and the values are very close to those of PET and PEF at 35 °C as observed by Burgess *et al.*[170] in their study of water vapor kinetic sorption. Therefore, relaxation-dominated process in both amorphous and semicrystalline PEV is detected as $\varphi \neq 1$ and times of relaxation of about 2×10^4 s. Compared to PET, PEV (either amorphous or semicrystalline) exhibits slightly lower water uptake due to the lower concentration of carboxylic groups on the polyester backbone. However, the diffusivity value of amorphous PEV results ≈ 10× higher than that of amorphous PET because of the inherent differences in segmental mobility. Moreover, the high degree of crystallinity (Xc = 60%) of semicrystalline PEV film proves to favour the diffusivity of water vapor molecules damaging water vapor barrier properties of PEV. As a consequence, both amorphous and highly crystalline PEV present worst water vapor barrier performances than PET.

3.3.3 Water vapor barrier properties of poly(ω-pentadecalactone) and P(EV-*co*-PDL) copolymers

3.3.3.1 Chemical structure and films crystallinity

Chemical structural information of poly(ω-pentadecalactone) (PPDL) and poly(ethylene vanillate-*co*-pentadecalactone) (P(EV-*co*-PDL)) random copolymers are provided in Figure 3.3. 16. In the current study, PPDL, P(EV-*co*-PDL) 60/40 and P(EV-*co*-PDL) 40/60 semicrystalline films were investigated. The glass transition temperature (Tg), measured by differential scanning calorimetry, is below room temperature for all the samples meaning that they are in a rubbery state at room temperature (Tg<Trt) and hence crystallization can't be avoided even if a rapid cooling is applied during film preparation.

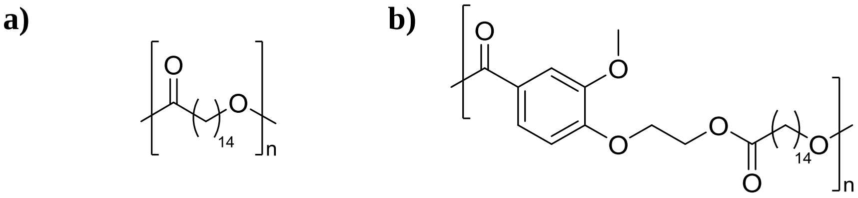

Figure 3.3. 16: Chemical structures of **a)** poly(ω-pentadecalactone) (PPDL) and **b)** poly(ethylene vanillate-*co*-pentadecalactone) copolymers (P(EV-*co*-PDL)).

Table 3.3. 2: Molar fraction of PDL units, molecular weight and degree of crystallinity of P(EV-*co*-PDL) copolymers and PPDL.

sample	F_{PDL}[a]	Mn × 10^{-3} (g mol^{-1})[b]	Mw × 10^{-3} (g mol^{-1})[b]	Tg (°C)[c]	Xc (%)[d]
P(EV-*co*-PDL) 60/40	0.44	7.4	12.7	-2	11
P(EV-*co*-PDL) 40/60	0.64	7.2	13.9	-2	24
PPDL	1	37.5	63.7	-27	62

[a] measured by ^{1}H-NMR analysis. [b] measured by GPC analysis. [c] measured by DSC 2nd heating scan at 10 °C min^{-1} after cooling at 10 °C min^{-1}. [d] measured by WAXS analysis.

The degree of crystallinity of P(EV-*co*-PDL) and PPDL films was evaluated by WAXS analysis shown in Figure 3.3. 17 and calculated according to Equation 3.3. 2. The values of crystallinity degree are reported in Table 3.3. 2 together with the molar composition, the molecular weight and the glass transition temperature of the investigated polyesters.

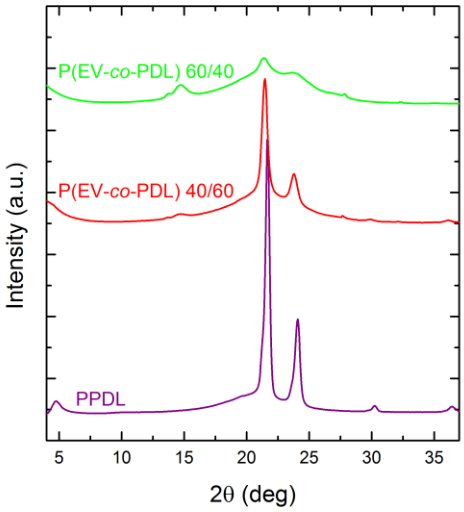

Figure 3.3. 17: WAXS pattern of P(EV-*co*-PDL) copolymers and PPDL semicrystalline films.

3.3.3.2 Sorption measurements

Kinetics gravimetric sorption measurements at 20 °C of P(EV-*co*-PDL) 60/40, P(EV-*co*-PDL) 40/60 and PPDL samples are depicted in Figure 3.3. 18, Figure 3.3. 19 and Figure 3.3. 20, respectively. As shown, the sample was exposed to sorption/desorption cycle from 0% RH to 95% RH and return. Each RH% step lasted 5 hours and mass equilibrium was reached for all the samples.

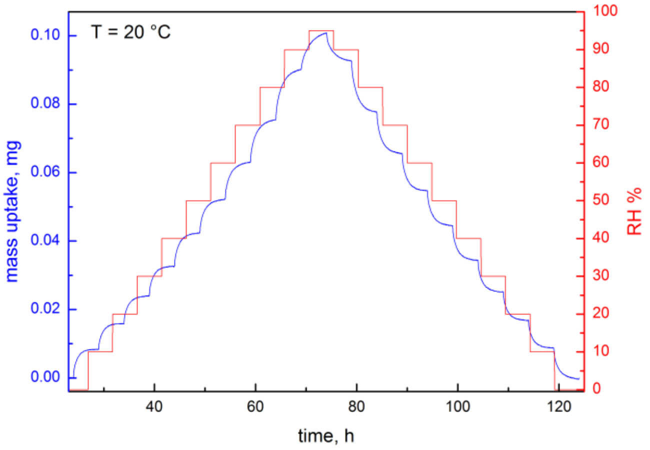

Figure 3.3. 18: Example of gravimetric water vapor sorption/desorption kinetic measurements of P(EV-*co*-PDL) 60/40 sample at 20°C.

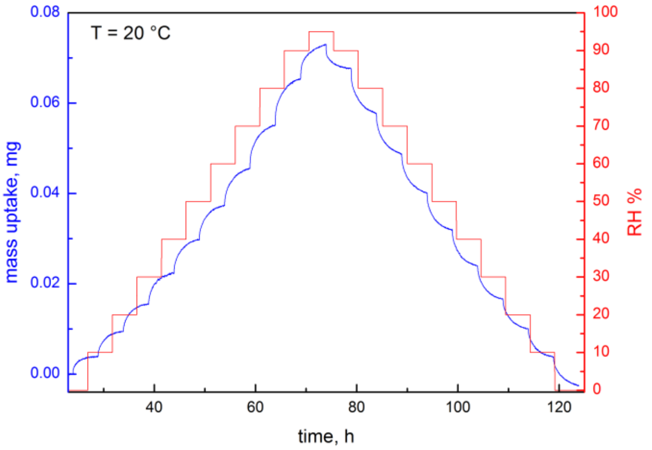

Figure 3.3. 19: Example of gravimetric water vapor sorption/desorption kinetic measurements of P(EV-*co*-PDL) 40/60 sample at 20 °C.

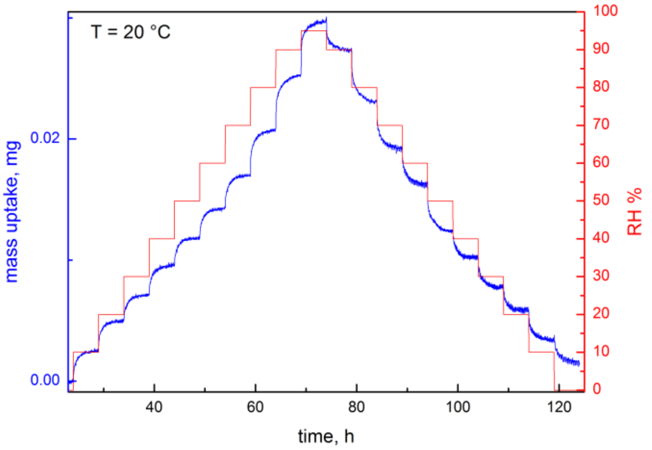

Figure 3.3. 20: Example of gravimetric water vapor sorption/desorption kinetic measurements of PPDL sample at 20 °C.

3.3.3.3 Sorption/desorption isotherms

Water vapor sorption and desorption isotherms of semicrystalline P(EV-*co*-PDL) 60/40, P(EV-*co*-PDL) 40/60 and PPDL films in the water activity range between 0 and 0.95 at 20 °C are shown in Figure 3.3. 21. In the same graph the sorption isotherm of the amorphous PEV film is reported for comparison. The water vapor sorption isotherms are almost linear to the activity axis up to $a_w = 0.6$ and weakly convex at high water vapor activity.

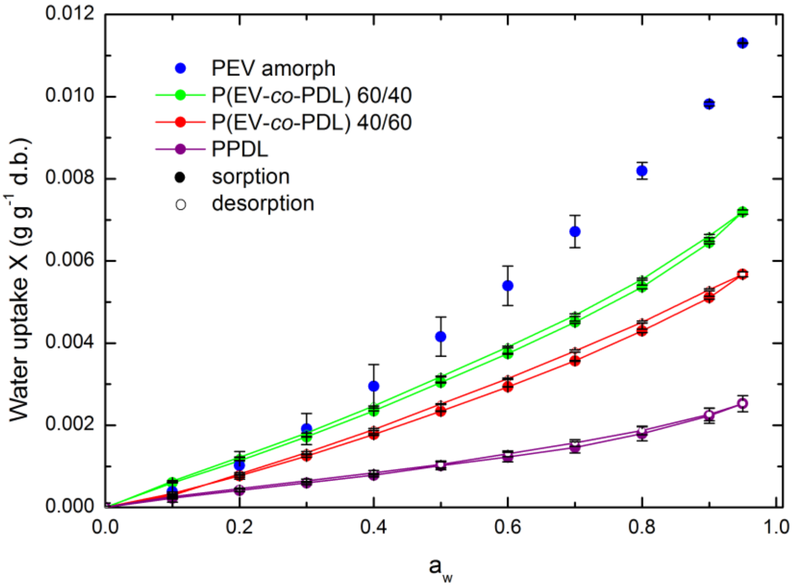

Figure 3.3. 21: Water vapor sorption isotherms of semycristalline P(EV-*co*-PDL) copolymers, PPDL and amorphous PEV films at 20 °C. The solid lines represent the Park model fitting.

Random sorption of water vapor in rubbery polymers matrix is described by Henry's law which provides a linear correlation between penetrant concentration and pressure: the penetrant randomly dissolves in the equilibrium dense polymer matrix and it is absorbed. However, a positive deviation from Henry's law sorption at high water vapor activity is observed and can indicate swelling or clustering which is the non-random distribution of penetrant within the polymer matrix. Swelling, as already discussed, is a rearrangement of polymer chains as function of water content and time, while clustering derives to self-hydrogen bonding of water molecules.

In PEV sample, swelling-induced plasticization recorded as time-dependent non-Fickian relaxations has been observed in paragraph 3.3.2. Since water vapor sorption kinetic curves of rubbery P(EV-*co*-PDL) and PPDL samples obey Fick's law and there's no evidence of non-Fickian relaxations, the upturn of the sorption isotherm has been ascribed to water clustering.

A model able to describe clustering phenomenon is the Park model.[181]

Park model corresponds to a multi-sorption mode which can be divided into three steps: (1) Langmuir sorption, (2) Henry's law and, (3) water clustering. The corresponding equation is:

$$X = \frac{A_L \cdot b_L \cdot a_w}{1 - b_L \cdot a_w} + k_H \cdot a_w + K_a \cdot a_w^n \tag{3.3. 5}$$

where X is the water vapor content (g g$^{-1}_{\text{d.b.}}$), A_L is the Langmuir capacity constant, b_L is the Langmuir affinity constant, k_H is the Henry's solubility coefficient, K_a is the equilibrium constant for the clustering reaction, n is the mean number of water molecules per cluster and a_w is the water vapor activity. The model fits extremely well all experimental sorption isotherms as shown in Figure 3.3. 21. The fitting parameters of the Park model are reported in Table 3.3. 3.

The Langmuir adsorption isotherm is used to describe the equilibrium between adsorbate and adsorbent system, where the adsorbate adsorption is limited to one molecular layer at or before a relative pressure of unity is reached. Although the isotherm initially proposed by Langmuir in 1918 [182] is generally suitable for describing the chemisorption process when ionic or covalent chemical bonds are formed between the adsorbent and the adsorbate, the equation is obeyed in many systems with moderately low surface coverage and can be easily extended to describe the behaviour of the binary adsorption system.

As shown in Table 3.3. 3, the contribution ascribable to Langmuir sorption (A_L and b_L values) is close to zero for all the samples as expected. The formation of a first monolayer of water molecules (surface coverage) on polymer surface isn't observed indicating that there are very few specific sites for water vapor adsorption. It was expected since all the samples are in their rubbery state characterized by the absence of frozen micropores as happens conversely in glassy polymers and are strongly hydrophobic.

Table 3.3. 3: Park fitting parameters which were identified from the water vapor sorption isotherm of P(EV-*co*-PDL) 60/40, P(EV-*co*-PDL) 40/60 and PPDL semicrystalline films at 20 °C.

Park model						
sample	k_H	K_a	n	A_L	b_L	RMSE
P(EV-*co*-PDL) 60/40	0.0058	0.0020	4.6	4.8E-12	1.7E-5	4.1E-5
P(EV-*co*-PDL) 40/60	0.0039	0.0020	2.6	1.7E-13	5.0E-5	4.5E-5
PPDL	0.0020	0.0009	7.0	8.1E-9	1.6E-5	1.3E-5

The parameter k_H, defined as the absorption by a dissolution mechanism of water molecules into the polymer matrix according to Henry's law, decreases with the increment of PDL molar fraction and is very low for PPDL sample proving the high hydrophobicity of PPDL homopolymer. Inclusion of ethylene vanillate units in copolymer structure slightly increases polyester absorption capability. Water molecules interact with carboxylic groups on the polyester backbone *via* hydrogen-bonding. By increasing the molar ratio of PDL units, decreases the molar density of carboxylic groups, likely reducing the amount of strong hydrogen bonding occurring between water molecules and the polyester. The molar density of carboxylic groups decreases in the following order: P(EV-*co*-PDL) 60/40 (0.00536 mol -COO groups per cm^3 polymer) > P(EV-*co*-PDL) 40/60 (0.00483 mol cm^{-3}) > PPDL (0.00325 mol cm^{-3}). Values of k_H decrease in the same order suggesting that absorption capability may be influenced by the concentration of strong hydrogen bonding sites on the polyester backbone. PPDL has the lowest carboxylic groups' molar density of the three polyesters and hence the lower water uptake and Henry's law constant.

The equilibrium constant for the clustering reaction K_a, which is correlated to the polymer ability to form water clusters, is lower for PPDL homopolymer than P(EV-*co*-PDL) copolymers. However, the size of water vapor clusters, related to the n mean number of water molecules per cluster, follows the order: PPDL (7.0) > P(EV-*co*-PDL) 60/40 (4.6) > P(EV-*co*-PDL) 40/60 (2.6). In copolymers, by increasing the amount of PDL units in the copolymer structure the ability to form clusters remains the same but the size of these clusters is decreased (n=2.6 in P(EV-*co*-PDL) 40/60). On the contrary, and unexpectedly, PPDL homopolymer form few clusters (low K_a) with high number of water molecules per water cluster (high n). This is probably correlating to the high degree of crystallinity of PPDL sample, i.e. Xc = 62% (Table 3.3. 2). Amorphous/crystalline interface is a non-equilibrium area and the water sorption in the amorphous phase can produce stress at the interface followed by "microvoids" formation. These interfacial gaps may promote aggregates formation even if PPDL chemical structure isn't predisposed to form clusters as proven by the lower value of K_a.

To confirm this clustering effect, the ENSIC (Engaged Species Induced Clustering) theory has been then used to determine the extent of water vapor clustering into P(EV-*co*-PDL) and PPDL. ENSIC model, based on a probabilistic and mechanistic approach, has been developed to describe molecular interactions in a solvent/polymer system and detect clustering.[183,184] The model is based on the assumption that the insertion of a solvent molecule into the polymer/solvent system will be governed by the affinity of the solvent for either a polymer segment or an already adsorbed solvent molecule. The increase of sorbed solvent molecule number (dn_S) due to an increase of the pressure (dp) in the gasesous phase can be related as:

$$dn_s = \ (k_p \cdot n_p + k_s \cdot n_s) \cdot \left(\frac{dp}{p_0}\right) \tag{3.3. 6}$$

where n_s and n_p represent the solvent and the polymer cell numbers into the polymer/solvent system, k_p is the affinity between the solvent and the polymer and k_s is the affinity between the solvent and a previously adsorbed molecule. Assuming the gas phase as ideal, integration of Equation 3.3. 6 leads to the following expression:

$$\phi_w = \frac{e^{(k_s - k_p)\cdot a_w} - 1}{(k_s - k_p)/k_p} \tag{3.3. 7}$$

where φ_w and a_w are the water volume fraction and activity.

Calculation of φ_w can be derived from m_{uptake} experimental data through Equation 3.3. 8 where 1.0018 (g cm^{-3}) is the density of water at 20 °C.

$$\phi_w = \frac{V_w}{V_w + V_{poly}} = \frac{m_{uptake}/1.0018}{m_{uptake}/1.0018 + m_{poly}/\delta_{poly}} \tag{3.3. 8}$$

The fitting parameters of the ENSIC model are reported Table 3.3. 4.

The parameter k_p is very low for all the samples proving the poor affinity between water and the investigated polyesters and is the lowest for PPDL homopolymer confirming conclusion made based on Park model fitting about the high hydrophobicity of this polymer. Indeed, PPDL sample, which is characterized by the lowest carboxylic groups' molar density, shows the lowest water-polymer affinity between the three polyesters. As expected, for P(EV-*co*-PDL) copolymers, k_p decreases with the increase of PDL molar fraction proportional to carboxylic groups' molar density. As stated before, inclusion of ethylene vanillate units in copolymer structure slightly increases water-polymer interactions. The values of k_s representing water-water interaction evolve in the following order: PPDL (0.96) > P(EV-*co*-PDL) 60/40 (0.95) > P(EV-*co*-PDL) 40/60 (0.93). The order is identical to that of the size of water vapor molecules aggregates n determined by the Park model. Aggregation of water molecules is higher in PPDL because of lack of water-polymer interaction; clustering is thus favoured. In addition, water strongly aggregate in PPDL sample because of the supposed presence of microvoids which would occur preferably in PPDL than in copolymers due to the high crystallinity of the material.

The results of ENSIC theory demonstrate that the water-water interactions extent in all materials and corroborate the analysis made with the Park parameters.

Table 3.3. 4: ENSIC fitting parameters which were identified from the water vapor sorption isotherm of P(EV-*co*-PDL) 60/40, P(EV-*co*-PDL) 40/60 and PPDL semicrystalline films at 20 °C.

	ENSIC			
sample	kp	ks	RMSE	ks/kp
P(EV-co-PDL) 60/40	0.140	0.95	1.1E-4	6.78
P(EV-co-PDL) 40/60	0.063	0.93	5.6E-5	14.76
PPDL	0.035	0.96	5.3E-5	27.43

Figure 3.3. 21 shows that the desorption isotherm superimposes that of sorption for all the samples. This is a proof that the upturn of the sorption isotherms at high water vapor activity is related to clustering and not to swelling since the swelling of polymer matrix is often linked to a hysteretic behaviour.[176]

3.3.3.4 Solubility

The water vapor solubility S of P(EV-*co*-PDL) copolymers and PPDL was determined by Henry's law in the water activity range 0-0.6 where the sorption isotherm is linear and clustering doesn't occur.

Henry's law allows determine solubility as follows:

$$C = k_D \cdot p \tag{3.3. 9}$$

where C is the water vapor concentration ($cm^3_{STP}\ cm^{-3}_{d.b.}$), p (Pa) is the pressure and k_D is the solubility coefficient ($cm^3_{STP}\ cm^{-3}_{d.b.}\ Pa^{-1}$).

As shown in Table 3.3. 5, the solubility coefficient k_D decreases with the increment of PDL molar fraction and results to be very low for PPDL sample corroborating the analysis made with the Park model. Inclusion of ethylene vanillate units in copolymer structure slightly increases $k_{D,}$ which is an index of absorption polymer capability. This is correlated to the molar density of carboxylic groups in the polyester chain. In the water activity range 0-0.6, the linear regression fits well experimental data as shown by r^2 reported in Table 3.3. 5.

Since solubility occurs in the amorphous phase and crystalline regions are almost impermeable, the solubility coefficient can be normalized by the degree of crystallinity in order to compare materials with different crystallinity as follows.

$$k_D = X_a \cdot k_D^a \tag{3.3. 10}$$

where k_D^a is the solubility in the amorphous phase and X_a is volume fraction of the amorphous phase. The trend of k_D^a is retained even when a normalization by the crystallinity is applied to P(EV-*co*-PDL) copolymers and PPDL: P(EV-*co*-PDL) 60/40 (3.94) > P(EV-*co*-PDL) 40/60 (3.45) > PPDL (2.20).

The solubility coefficient was determined also for the desorption isotherm in the a_w range 0.6-0 for all the samples. Table 3.3. 5 shows that sorption and desorption solubility coefficients are very similar proving that the sorption and desorption cycles superimpose.

Table 3.3. 5: Solubility coefficient k_D determined by Henry's law in the sorption water activity range 0-0.6 and desorption a_w 0.6-0 for P(EV-*co*-PDL) 60/40, P(EV-*co*-PDL) 40/60 and PPDL samples. Solubility coefficient k_D^a of the amorphous phase determined by normalizing for the degree of crystallinity.

sample	activity range	$k_D \times 10^3$ (cm^3_{STP} $cm^{-3}_{d.b.}$)	$k_D^a \times 10^3$ (cm^3_{STP} $cm^{-3}_{d.b.}$)	r^2
P(EV-*co*-PDL) 60/40	0-0.6	3.50 ± 0.01	3.94	0.997
	0.6-0	3.68 ± 0.01	4.13	0.997
P(EV-*co*-PDL) 40/60	0-0.6	2.62 ± 0.02	3.45	0.987
	0.6-0	2.81 ± 0.02	3.69	0.979
PPDL	0-0.6	0.84 ± 0.01	2.20	0.998
	0.6-0	0.84 ± 0.04	2.21	0.994

The water vapor solubility coefficients k_D determined for P(EV-*co*-PDL) and PPDL samples have been compared with the k_D values of some other polymers as function of temperature as shown in Figure 3.3. 22. The solubility values of P(EV-*co*-PDL) copolymers at 20 °C are close to those of other polyesters such as poly(ethylene terephthalate) (PET) and poly(lactic acid) (PLA). This can be related to their similar chemical structure presenting carboxylic groups along the polymer backbone.

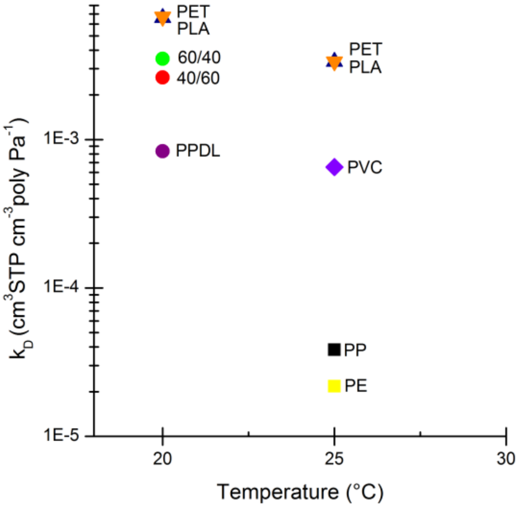

Figure 3.3. 22: Water vapor solubility coefficient k_D of P(EV-*co*-PDL) 60/40, P(EV-*co*-PDL) 40/60 and PPDL samples of the current study compared with other polymeric samples as function of temperature. PET 20 °C ref. [185], 25 °C ref. [186]; PLA 20 °C ref. [187], 25 °C ref. [188]; PVC 25 °C ref. [189]; PP 25 °C ref. [186]; PE 25 °C ref. [186].

It is well known that the solubility is function of temperature and Figure 3.3. 22 reports the trend at 20 and 25 °C for PET and PLA: the solubility decreases by increasing the temperature. When compares solubility of different polymers, determined at different temperatures, it has to consider the effect of temperature besides the effect of the different chemical structure.

The solubility value of poly(vinyl chloride) (PVC) is recorded at 25 °C and results to be lower than P(EV-*co*-PDL) copolymers and PPDL solubility values at 20 °C. Clearly, this is function of the different experimental temperature but it can be hypothesized that at 20 °C the solubility of PVC is in the range of PPDL polyester. The solubility values of polyethylene (PE) and polypropylene (PP) at 25 °C are lower than those of P(EV-*co*-PDL) and PPDL samples and it can be hypothesized that at 20 °C their solubility remains lower. These considerations have to be related to the chemical structure of the polymers: P(EV-*co*-PDL) and PPDL are polyesters presenting carboxylic groups on the backbone, which are sites able to bond water molecules, while PVC, PP and PE are polyolefins constitute of -CH_2 sequence without specific sites for water molecules adsorption on the backbone.

3.3.3.5 Diffusivity

Water vapor diffusivity values were estimated for each relative humidity step from individual kinetic gravimetric water vapor uptake measurements.

The analytical solution of water vapor diffusivity is described by Crank *et al.*[167]:

$$\left.\frac{m_t}{m_\infty}\right|_C = 1 - \sum_{n=0}^{\infty} \frac{8}{(2n+1)^2\pi^2} exp\left(-\frac{D\,(2n+1)^2\pi^2 t}{L^2}\right) \qquad (3.3.\ 11)$$

where m_t denotes the water uptake at time t, m_∞ denotes the water uptake after infinite time represented by equilibrium and D ($m^2\ s^{-1}$) is the Fickian diffusion coefficient averaged over the concertation interval. D is an overall mass transport phenomenon that does not represent only Fick’s diffusion but the different water transport mechanisms occurring in the material. D is thus an apparent or effective diffusivity, noted D_{eff} in the following. D_{eff} is considered constant for the RH step considered, therefore D_{eff} values are plotted at the midpoint of the respective RH step intervals.

Individual kinetic sorption/desorption uptake curves for each relative humidity step are provided in Figure 3.3. 23 for P(EV-*co*-PDL) 60/40, in Figure 3.3. 24 for P(EV-*co*-PDL) 40/60 and in Figure 3.3. 25 for PPDL. The red lines labelled as “calculated” represent the Crank model fits from Equation 3.3. 11 while the experimental data are reported in blue. Crank model fits well all the experimental data even if for PPDL sample the water vapor sorption is in the range of instrumental error.

Effective diffusion coefficients (D_{eff}) obtained from the Crank model fit to the kinetic sorption/desorption curves are plotted in Figure 3.3. 26 for all the samples.

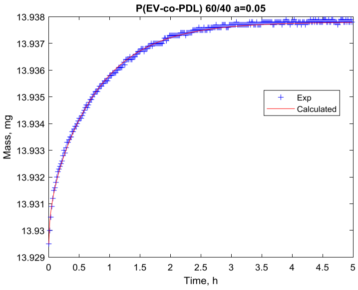
P(EV-co-PDL) 60/40 a=0.05
Mass, mg
13.938
13.937
13.936
13.935
13.934
13.933
13.932
13.931
13.93
13.929
Time, h
0 0.5 1 1.5 2 2.5 3 3.5 4 4.5 5
Exp
Calculated

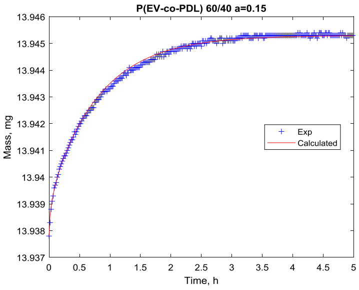
P(EV-co-PDL) 60/40 a=0.15
Mass, mg
13.946
13.945
13.944
13.943
13.942
13.941
13.94
13.939
13.938
13.937
Time, h
0 0.5 1 1.5 2 2.5 3 3.5 4 4.5 5
Exp
Calculated

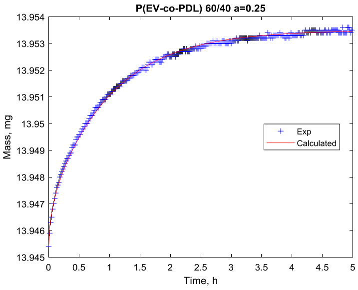
P(EV-co-PDL) 60/40 a=0.25
Mass, mg
13.954
13.953
13.952
13.951
13.95
13.949
13.948
13.947
13.946
13.945
Time, h
0 0.5 1 1.5 2 2.5 3 3.5 4 4.5 5
Exp
Calculated

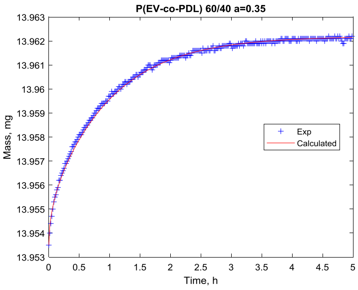
P(EV-co-PDL) 60/40 a=0.35
Mass, mg
13.963
13.962
13.961
13.96
13.959
13.958
13.957
13.956
13.955
13.954
13.953
Time, h
0 0.5 1 1.5 2 2.5 3 3.5 4 4.5 5
Exp
Calculated

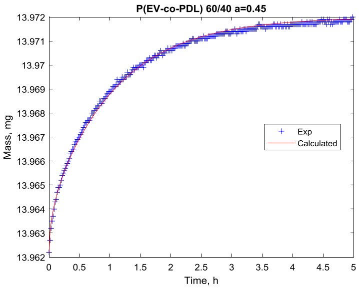
P(EV-co-PDL) 60/40 a=0.45
Mass, mg
13.972
13.971
13.97
13.969
13.968
13.967
13.966
13.965
13.964
13.963
13.962
Time, h
0 0.5 1 1.5 2 2.5 3 3.5 4 4.5 5
Exp
Calculated

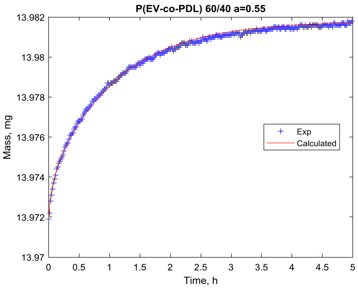
P(EV-co-PDL) 60/40 a=0.55
Mass, mg
13.982
13.98
13.978
13.976
13.974
13.972
13.97
Time, h
0 0.5 1 1.5 2 2.5 3 3.5 4 4.5 5
Exp
Calculated

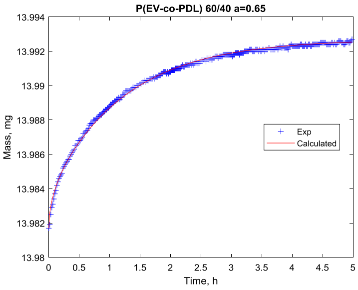
P(EV-co-PDL) 60/40 a=0.65
Mass, mg
13.994
13.992
13.99
13.988
13.986
13.984
13.982
13.98
Time, h
0 0.5 1 1.5 2 2.5 3 3.5 4 4.5 5
Exp
Calculated

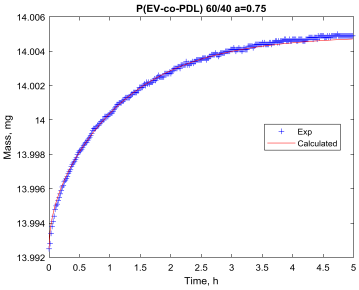
P(EV-co-PDL) 60/40 a=0.75
Mass, mg
14.006
14.004
14.002
14
13.998
13.996
13.994
13.992
Time, h
0 0.5 1 1.5 2 2.5 3 3.5 4 4.5 5
Exp
Calculated

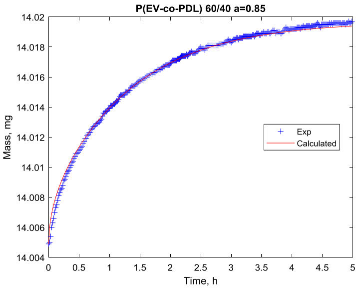
P(EV-co-PDL) 60/40 a=0.85
Mass, mg
14.02
14.018
14.016
14.014
14.012
14.01
14.008
14.006
14.004
Time, h
0 0.5 1 1.5 2 2.5 3 3.5 4 4.5 5
Exp
Calculated

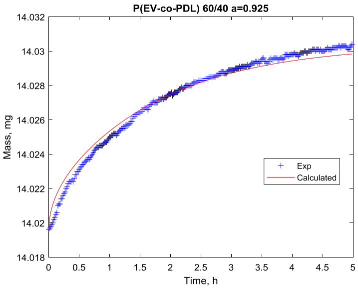
P(EV-co-PDL) 60/40 a=0.925
Mass, mg
14.032
14.03
14.028
14.026
14.024
14.022
14.02
14.018
Time, h
0 0.5 1 1.5 2 2.5 3 3.5 4 4.5 5
Exp
Calculated

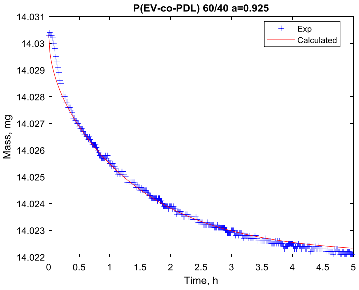
P(EV-co-PDL) 60/40 a=0.925
Mass, mg
14.031
14.03
14.029
14.028
14.027
14.026
14.025
14.024
14.023
14.022
Time, h
0 0.5 1 1.5 2 2.5 3 3.5 4 4.5 5
Exp
Calculated

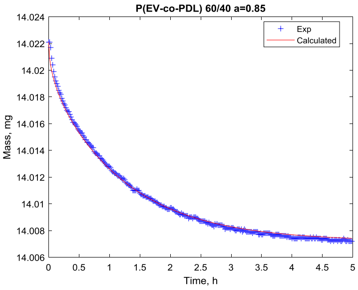
P(EV-co-PDL) 60/40 a=0.85
Mass, mg
14.024
14.022
14.02
14.018
14.016
14.014
14.012
14.01
14.008
14.006
Time, h
0 0.5 1 1.5 2 2.5 3 3.5 4 4.5 5
Exp
Calculated

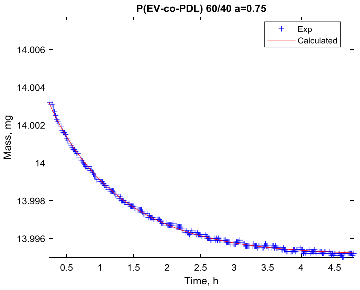
P(EV-co-PDL) 60/40 a=0.75
Mass, mg
14.006
14.004
14.002
14
13.998
13.996
Time, h
0.5 1 1.5 2 2.5 3 3.5 4 4.5
Exp
Calculated

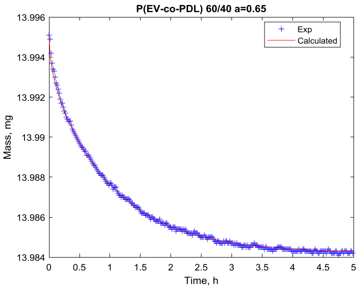
P(EV-co-PDL) 60/40 a=0.65
Mass, mg
13.996
13.994
13.992
13.99
13.988
13.986
13.984
Time, h
0 0.5 1 1.5 2 2.5 3 3.5 4 4.5 5
Exp
Calculated

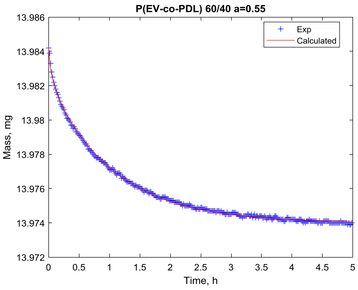
P(EV-co-PDL) 60/40 a=0.55
Mass, mg
13.986
13.984
13.982
13.98
13.978
13.976
13.974
13.972
Time, h
0 0.5 1 1.5 2 2.5 3 3.5 4 4.5 5
Exp
Calculated

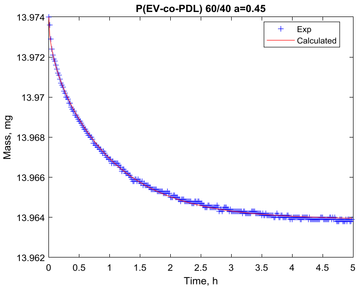
P(EV-co-PDL) 60/40 a=0.45
Mass, mg
13.974
13.972
13.97
13.968
13.966
13.964
13.962
Time, h
0 0.5 1 1.5 2 2.5 3 3.5 4 4.5 5
Exp
Calculated

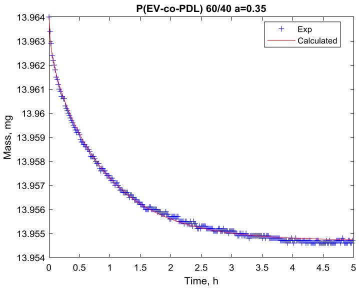
P(EV-co-PDL) 60/40 a=0.35
Mass, mg
13.964
13.963
13.962
13.961
13.96
13.959
13.958
13.957
13.956
13.955
13.954
Time, h
0 0.5 1 1.5 2 2.5 3 3.5 4 4.5 5
Exp
Calculated

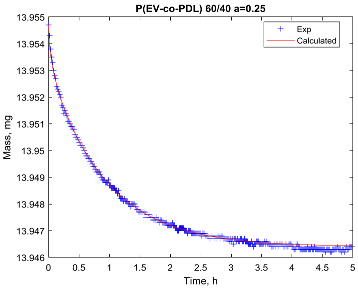
P(EV-co-PDL) 60/40 a=0.25
Mass, mg
13.955
13.954
13.953
13.952
13.951
13.95
13.949
13.948
13.947
13.946
Time, h
0 0.5 1 1.5 2 2.5 3 3.5 4 4.5 5
Exp
Calculated

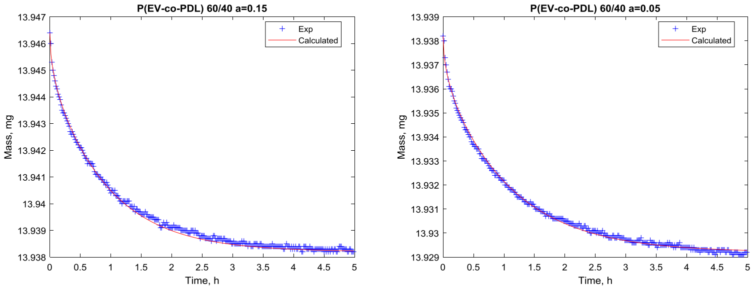

Figure 3.3. 23: Kinetic sorption/desorption data for water vapor on P(EV-*co*-PDL) 60/40 at 20 °C measured by DVS. Red lines represent model fits from Equation 3.3. 11 while experimental data are represented in blue. The sorption intervals are labelled in each respective graph.

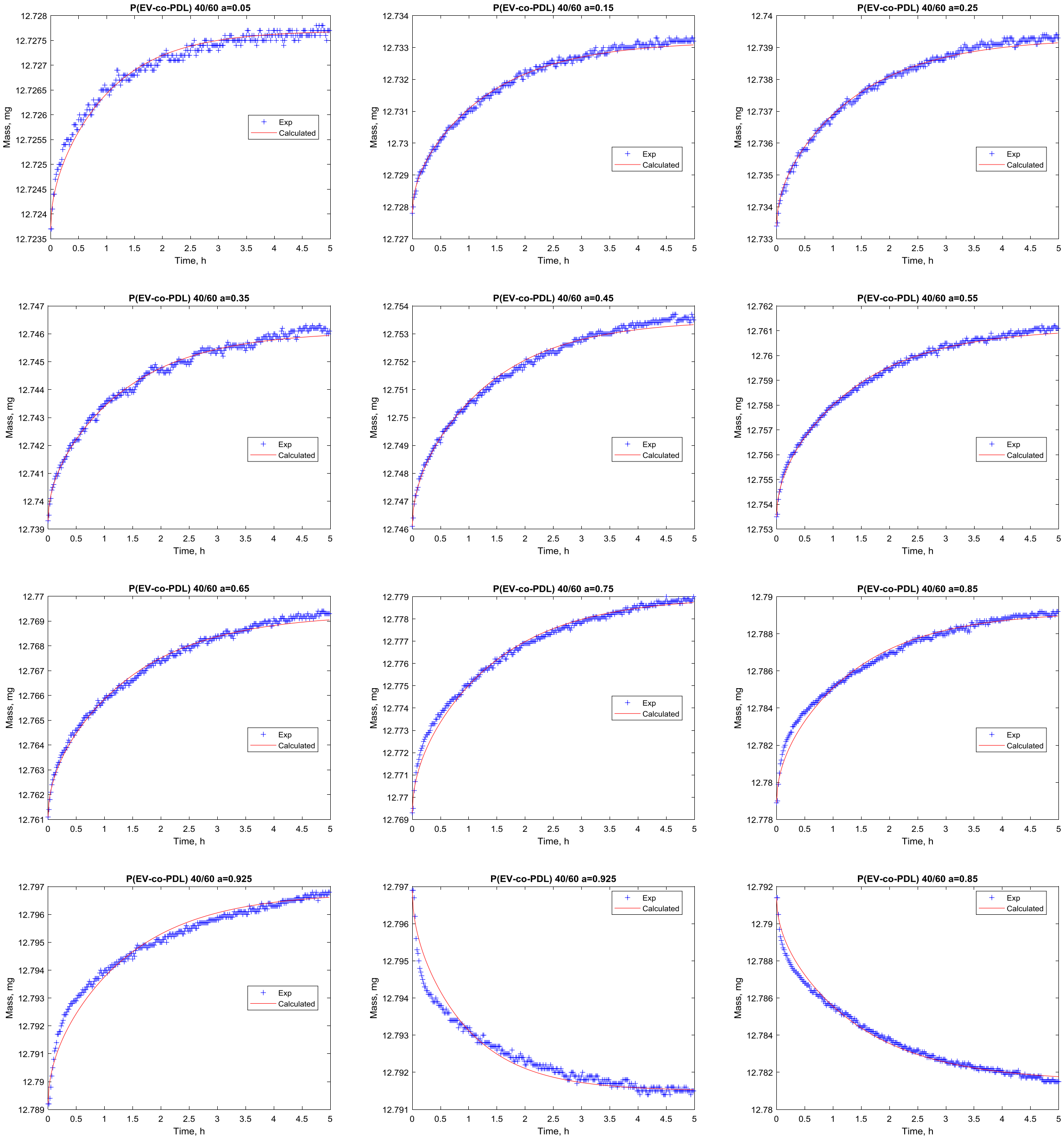

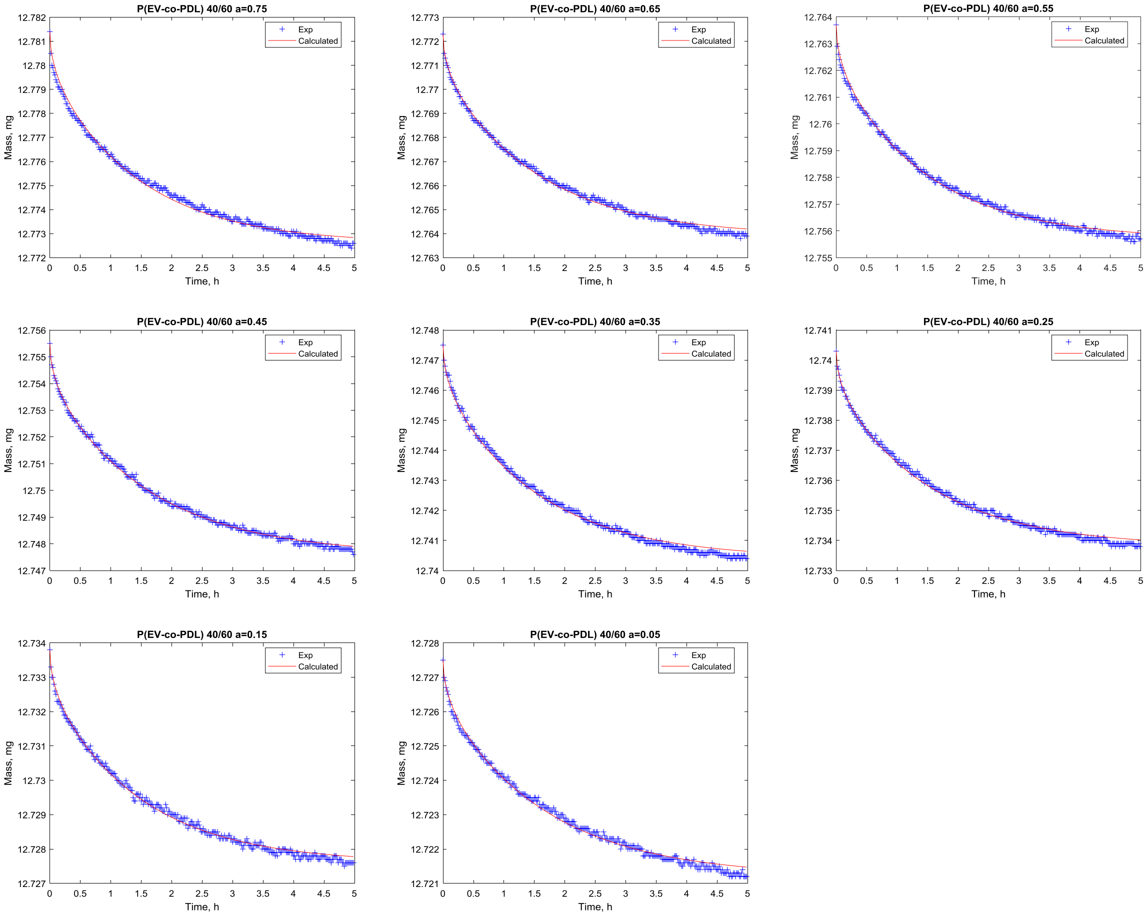

Figure 3.3. 24: Kinetic sorption/desorption data for water vapor on P(EV-*co*-PDL) 40/60 at 20 °C measured by DVS. Red lines represent model fits from Equation 3.3. 11 while experimental data are represented in blue. The sorption intervals are labelled in each respective graph.

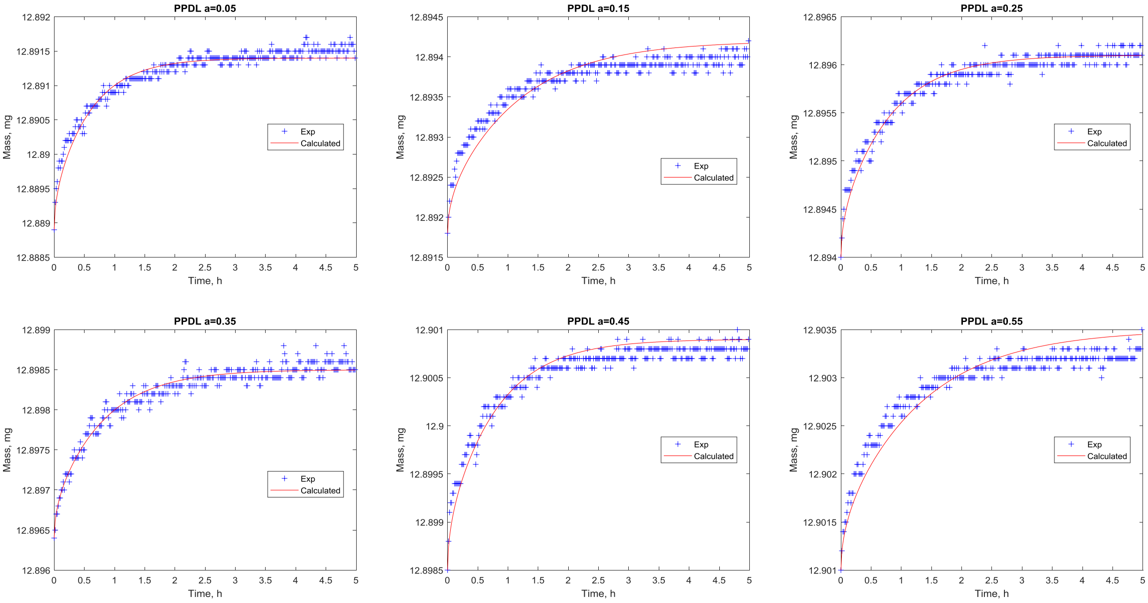

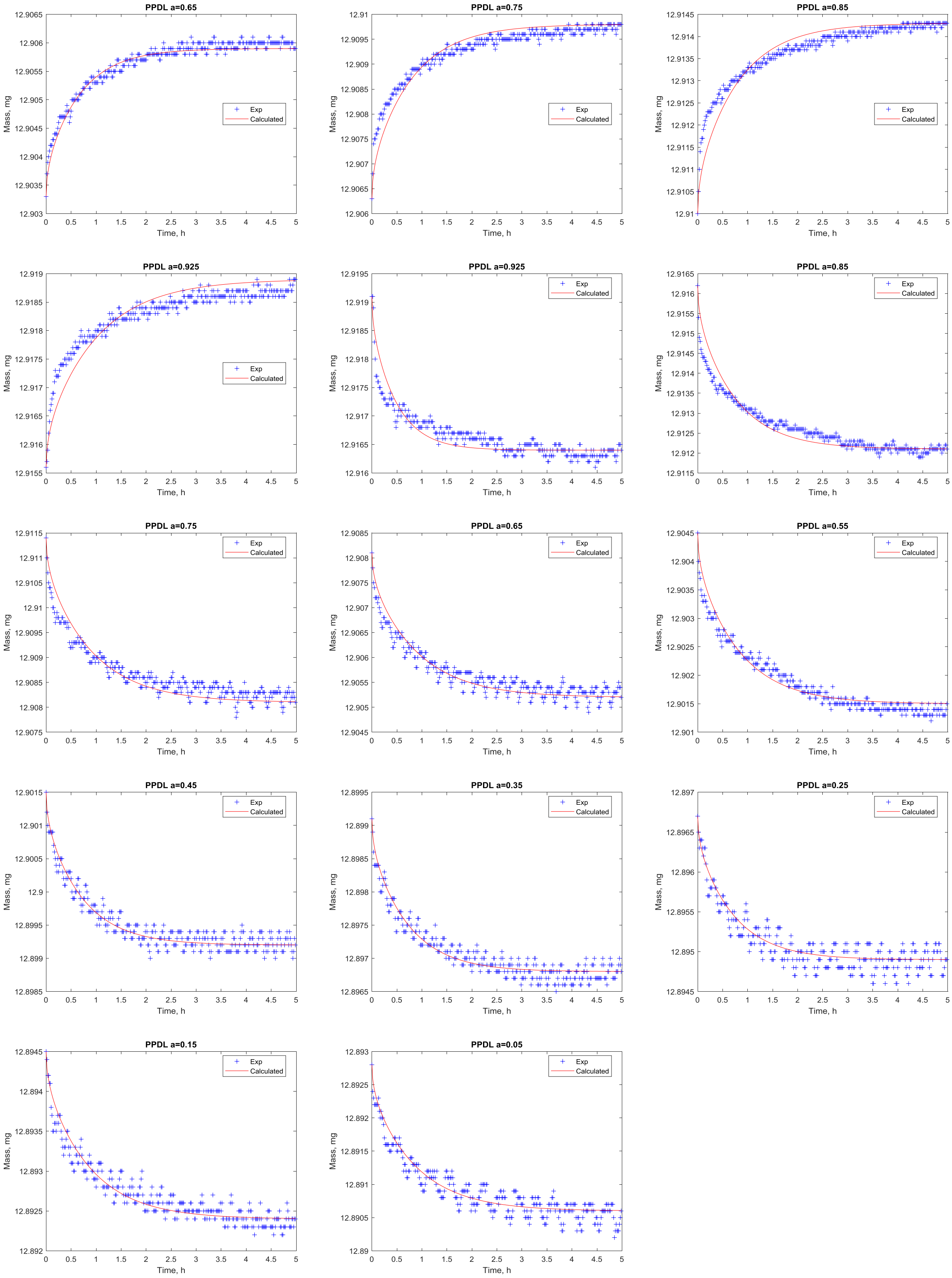

Figure 3.3. 25: Kinetic sorption/desorption data for water vapor on PPDL at 20 °C measured by DVS. Red lines represent model fits from Equation 3.3. 11 while experimental data are represented in blue. The sorption intervals are labelled in each respective graph.

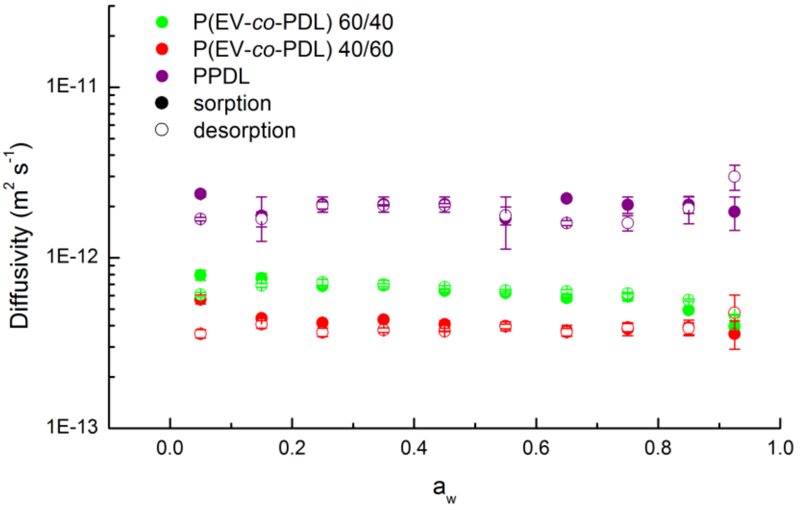

Figure 3.3. 26: Effective water vapor diffusivity D_{eff} for P(EV-*co*-PDL) 60/40, P(EV-*co*-PDL) 40/60 and PPDL semicrystalline films at 20 °C.

According to Figure 3.3. 26, D_{eff} first increases up to a_w of 0.5 and then decreases slightly but significantly for all the materials. D_{eff} increase is related to the enhanced segmental mobility while D_{eff} decrease to the increase of the effective diameter of the diffusing penetrant. As stated before, a positive deviation from Henry's law sorption at high water vapor activity can indicate swelling or clustering. At high water vapor activity, the upturn in solubility coupled with a simultaneous increase in D_{eff}, evidence of the enhanced segmental mobility, indicates swelling. Alternatively, the upturn in solubility accompanied with a simultaneous decrease in D_{eff} indicates clustering, i.e. water molecules clustered together whose size hampers diffusion. The decrease of D_{eff} at high water vapor activity for all the materials confirms that the deviation from Henry's law sorption can be referred to clusters formation.

By comparing the samples, averaged D_{eff} across the entire water vapor activity range follows the order: PPDL (2.02×10^{-12}) > P(EV-*co*-PDL) 60/40 (6.26×10^{-13}) > P(EV-*co*-PDL) 40/60 (4.14×10^{-13}).

In copolymers, the effective diffusivity increases (from 4.14 to 6.26×10^{-13} m^2 s^{-1}) when crystallinity decreases (from 24 to 11%) which is somewhere expected. Indeed in semicrystalline polymers, the crystalline regions act as impermeable barriers analogous of filler particles and thus contribute to increase the tortuosity and the diffusion pathway for the penetrant, resulting normally to a slowed down diffusivity. However, in highly crystalline materials, such as PPDL (62%) the permeable amorphous phase is trapped in between a crystal and the near one and thus, the interface amorphous/crystal constitutes a considerable fraction of the sample. The possibility that water sorption in the amorphous phase stresses the interface amorphous/crystal has to be considered and that this could lead to gaps formation. In that case, the created “microvoids” would enhance diffusivity. The formation of “microvoids” has also been related to cluster size at high water vapor activity for PPDL sample.

Besides crystallinity, diffusivity is also influenced by the chemical structure of the sample. PDL unit is characterized by a sequence of 14 aliphatic -CH_2 while EV by a *p*-substitute aromatic ring bonded to a carboxylic group from one side and to an ether one from the other and presenting a methoxy group. In EV unit, because of the presence of the ether group from one side, the ring-flipping is not restricted to defined angles and the presence of a lateral methoxy group increases the free volume. PDL unit is very flexible but the rotations of -CH_2 units don’t cause a significant free volume. It follows that the inclusion of PDL units in copolymer chemical structure hinders the water transport as proven by the sample P(EV-*co*-PDL) 40/60. This is also confirmed by the D_{eff} value of amorphous PEV (1.0×10^{-11} m^2 s^{-1}) which is the highest of the four.

In desorption mode, D_{eff} value are almost identical to the ones recorded during sorption proving that morphological changes in the polymer matrix don’t occur.

Table 3.3. 6: Effective water vapor diffusivity coefficients of P(EV-*co*-PDL) copolymers and PPDL samples, which were determined from water vapor sorption experiments on semicrystalline films at 20 °C.

sample	$D_{eff} \times 10^{13}$ (m^2 s^{-1})		RMSE × 10^8 (mg)	
	sorption	desorption	sorption	desorption
P(EV-co-PDL) 60/40	6.26 ± 0.04	6.31 ± 0.16	0.12	0.10
P(EV-co-PDL) 40/60	4.14 ± 0.26	4.21 ± 0.07	0.14	0.13
PPDL	20.24 ± 2.56	19.39 ± 2.21	0.13	0.14

3.3.3.6 Permeability

The theoretical water vapor permeability (P) can be determined from solubility (S) and diffusivity (D) values of sorption as follows [190]:

$$P = S \cdot D \qquad (3.3.\ 12)$$

In the current study, S correspond to the solubility coefficient k_D determined by Henry’s law reported in Table 3.3. 5 while D is the effective diffusivity averaged across the entire a_w reported in Table 3.3. 6.

Table 3.3. 7: Theoretical water vapor permeability (WVP) values of P(EV-*co*-PDL) copolymers and PPDL samples which were determined from Equation 3.3. 12.

sample	WVP × 10^{14} (mol STP m m^{-2} s^{-1} Pa^{-1})
P(EV-co-PDL) 60/40	11.02 ± 0.09
P(EV-co-PDL) 40/60	4.85 ± 0.34
PPDL	8.36 ± 1.24

The water vapor permeability has been determined according to Equation 3.3. 12 for P(EV-*co*-PDL) copolymers and PPDL semicrystalline films and the corresponding values (WVP) are reported in Table 3.3. 7 and depicted in Figure 3.3. 27. Water vapor permeability values follow the order: P(EV-*co*-PDL) 60/40 > PPDL > P(EV-*co*-PDL) 40/60. As concern copolymers, by increasing the molar fraction of PDL units, the polyester turns to be more impermeable. On the other hand, despite its low value of solubility, PPDL sample shows a permeability higher that the copolymer P(EV-*co*-PDL) 40/60 because of its high value of D_{eff}.

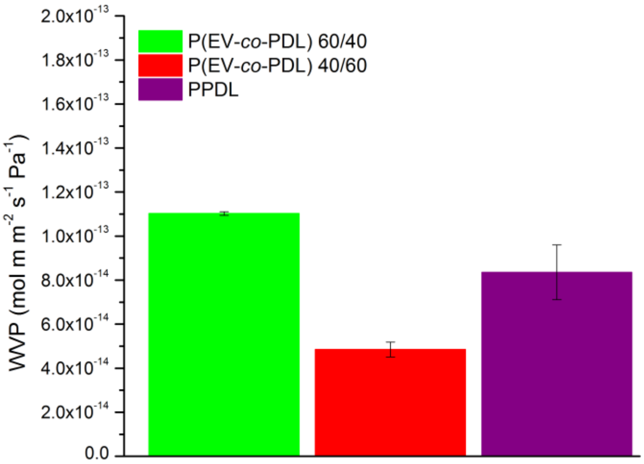

Figure 3.3. 27: Theoretical water vapor permeability (WVP) representation of P(EV-*co*-PDL) copolymers and PPDL samples which were determined from Equation 3.3. 12.

The water vapor permeability of the samples has been compared with that of other polymers as function of temperature in Figure 3.3. 28. As shown, the investigated materials exhibit a water vapor permeability comparable to polyethylene and poly(ethylene terephthalate).

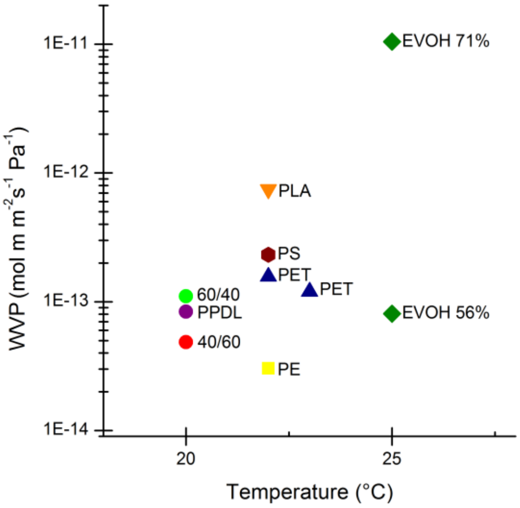

Figure 3.3. 28: Water vapor permeability (WVP) of P(EV-*co*-PDL) 60/40, P(EV-*co*-PDL) 40/60 and PPDL samples of the current study compared with other polymeric samples as function of temperature. PET 22 °C ref. [191], 23 °C ref. [164]; oriented-PLA 22 °C ref. [191], oriented-PS 22 °C ref. [191]; PE 22 °C ref. [188]; EVOH 56%, 71% 25 °C ref. [192].

3.3.4 Conclusions

Water vapor sorption kinetic in glassy PEV and rubbery PPDL and P(EV-*co*-PDL) at 20 °C was investigated using a gravimetric method over the water activity range 0-0.95.

The discussion of the results was split in two parts since glassy and rubbery polymers have completely different behaviour.

I. Water transport mechanism in amorphous and semicrystalline PEV demonstrates to obey Fickian-type sorption at low water vapor activity. On the contrary, at high water vapor activity the water vapor sorption curves exhibit a mass drift due to the presence of non-Fickian relaxations and mass equilibrium is not reached. The sorption isotherms were determined from pseudo-equilibrium mass content and modelled using a new dual mode sorption model. Amorphous PEV exhibits slightly higher water uptake compared to semicrystalline PEV since crystallites act as impermeable filler particles in the polymer matrix. Compared to amorphous PET, amorphous PEV exhibits lower water uptake due to the lower concentration of carboxylic groups on the polyester backbone. The irreversible relaxation of PEV polymer chains results in the incorporation of additional water at high activity, which is recorded as the upturn of the sorption isotherm, and simultaneously in a hysteretic behavior during desorption. The relaxation of polymer chains can be related to swelling-induced plasticization. Because of the presence of non-Fickian relaxations, the determination of water diffusion coefficient from individual kinetic sorption/desorption uptake curves required treatment with the Barens-Hopfenberg model. Semicrystalline PEV exhibits a significantly higher water diffusion coefficient compared to the completely amorphous sample because the stress at the amorphous/crystalline interface produced by water absorption in the amorphous phase induces “microvoids” formation that favours water diffusion. As concerns amorphous PEV, it exhibits higher averaged water diffusion coefficient of ≈ 10× compared to amorphous PET. With respect to PET, PEV aromatic ring is less sterically hindered by the presence of an ether group from one side rather than two carboxylic groups and thus the ring-flipping is not restricted to defined angles of rotation leading to an enhanced segmental flexibility of the chain.

II. Water transport mechanism in rubbery PPDL, P(EV-*co*-PDL) 60/40 and P(EV-*co*-PDL) 40/60 demonstrates to obey Fickian-type sorption over the entire water vapor activity range. The water sorption isotherms are linear relation to the activity axis up to a_w=0.6 and weakly convex at high water vapor activity because of the existence of clustering phenomenon. The clusters formation was evidenced owing to the Park and ENSIC models. The solubility of the polyesters was determined by applying Henry’s law in the a_w 0-0.6 and follows the order: P(EV-*co*-PDL) 60/40 > P(EV-*co*-PDL) 40/60 > PPDL. The trend is consistent with the concentration of carboxylic groups in the polyester backbone that constitute sites of interaction between water and polymer.

Water diffusion coefficient from individual kinetic sorption/desorption uptake curves was determined by means of Crank model. All the samples exhibit a negative correlation between diffusion coefficient and increasing water vapor activity, index of clustering phenomenon. PPDL sample exhibits the highest water diffusion coefficient of the three because of the formation of “microvoids” in high crystalline samples. As concerns as copolymers, P(EV-*co*-PDL) 40/60 shows lower water diffusion coefficient than P(EV-*co*-PDL) 60/40 because the PDL units, sequence of 14 -CH_2 groups, hinder water transport better than the EV units, in which the aromatic ring-flipping increases free volume. The solubility and diffusivity values can be combined using the common relationship P = SD to provide theoretical water vapor permeability of the samples that follows the order: P(EV-*co*-PDL) 60/40 > PPDL > P(EV-*co*-PDL) 40/60. Despite the lower solubility, PPDL sample is more permeable than copolymer P(EV-*co*-PDL) 40/60 because of the supposed “microvoids” formation during sorption that enhances diffusivity.

> The determined water vapor permeability of PPDL and P(EV-*co*-PDL) copolymers interposes between polyethylene and poly(ethylene terephthalate) proving that the polyesters are suitable for packaging applications.

In conclusion, while PEV can’t compete with PET water vapor barrier performances, P(EV-*co*-PDL) copolymers show barrier properties exceeded those of PET, in between PET and PE. This peculiarity demonstrate that P(EV-*co*-PDL) copolymers can be suitable in food packaging applications in the attempt to replace petro-derived polymers.

3.3.5 Experimental

3.3.5.1 Materials

Poly(ethylene vanillate) (PEV), poly(ω-pentadecalactone) (PPDL) and random copolymers P(EV-*co*-PDL) 60/40 and 40/60 were synthesized according to the synthetic procedures presented in chapter 3.2.

The chemical structure of the synthesized polyesters was verified by ^{1}H-NMR.

Molar fraction, molecular weight and glass transition temperature of PEV, P(EV-*co*-PDL) and PPDL are reported in Figure 3.3.5. 1.

Figure 3.3.5. 1: Molar fraction of EV units, molecular weight and glass transition temperature of PEV, P(EV-*co*-PDL) copolymers and PPDL.

sample	F_{EV}[a]	Mn × 10^{-3} (g mol^{-1})[b]	Mw × 10^{-3} (g mol^{-1})[b]	Tg (°C)[c]
PEV	1	11.0	-	75[d]
P(EV-*co*-PDL) 60/40	0.56	7.4	12.7	-2
P(EV-*co*-PDL) 40/60	0.36	7.2	13.9	-2
PPDL	0	37.5	63.7	-27[e]

[a] measured by ^{1}H-NMR analysis. [b] measured by GPC analysis. [c] measured by DSC 2nd heating scan at 10 °C min^{-1} after cooling scan at 10 °C min^{-1}. [d] measured by DSC 2nd heating scan at 10 °C min^{-1} after melt-quenching. [e] measured by DMTA analysis from ref. [145]

3.3.5.2 Film preparation

The synthesized materials were grinded using an Ika M20 Mill, Staufen, Germany. Resulting powders were dried at 60 °C for 24 hours. Semicrystalline PEV and PPDL films were obtained using a hydraulic thermo-press Carver, Wabash, Indiana, USA. Dried powder was thermo-moulded between two Teflon sheets at a temperature above 5 °C the end melting temperature for 2 min at 10 bar and 2 min at 100 bar. Film was quickly cooled to room temperature between the sheets under pressure by using running water.

Amorphous PEV film was obtained after quenching the molten sample in liquid nitrogen hindering crystallization.

P(EV-*co*-PDL) films were obtained using a hydraulic thermo-press Pinette Emidecau Industries, Chalon sur Saône, France. Dried powder was thermo-moulded between two Teflon sheets at a temperature above 5 °C the end melting temperature for 2 min at 10 bar and 2 min at 100 bar. Film was then cooled between the sheets at room temperature under weight. The film was realized using a Teflon template of 300 μm thickness.

The average thickness of the films were determined from 10 measurements randomly taken over the film surface using a precision thickness gauge, Hanatek instruments, East Sussex, UK. PEV films are characterized by 600 μm thickness while PPDL and P(EV-*co*-PDL) by 300 μm thickness.

3.3.5.3 Differential scanning calorimetry

Differential scanning calorimetry measurements were performed using a Q200 modulated DSC, equipped with a refrigerated cooling system TA Instruments, New Castle, USA. For each experiment, the sample (around 5 mg) was placed in hermetic aluminum pan and heated at 10 °C min^{-1} from 20 °C to 285 °C. The measurements were performed under nitrogen atmosphere. Resulting thermograms display the variation of heat flow per grams of sample (W g^{-1}) as function of temperature (°C).

3.3.5.4 Wide angle X-ray scattering analysis

Wide angle X-ray scattering (WAXS) experiments were performed using an in-house setup of the Laboratoire Charles Coulomb, University of Montpellier, France. A high brightness low power X-ray tube, coupled with an aspheric multilayer optic (GeniX3D from Xenocs) was employed. It delivers an ultralow divergent beam (0.5mrad, λ=0.15418nm). Scatterless slits were used to give a clean 0.6mm beam diameter with a flux of 35 Mphotons s^{-1} at the sample. We worked in a transmission configuration and scattered intensity was measured by a 2D “Pilatus” 300K pixel detector by Dectris (490·600 pixels) with pixel size of 172·172μm^2, at a distance of 0.2m from the sample. All intensities were corrected by transmission and the empty cell contribution was subtracted.

3.3.5.5 Dynamic water vapor sorption

Kinetic gravimetric sorption measurements were performed using a controlled atmosphere Dynamic Vapor Sorption (DVS) system, Surface Measurements System Ltd., London, UK at 20 °C. This system provides a humidified air flow by mixing separate wet and dry air flows and the resulting steam passes over a pan containing the sample, which is attached to a Cahn microbalance. In this way, the DVS apparatus allows recording sample mass evolution with time as a function of relative humidity (RH). Mass evolution was carried out on small section of film, around 0.5 cm^2 and 15 mg, deposited directly on the pan. Before performing sorption/desorption kinetics experiments, the sample was dried at 0% RH in DVS chamber at 20 °C for 24 hours to establish the dry mass. The sample was then exposed at 20 °C to the following RH profile: from 0 to 95% in increments of 10% up to 90% and 5% for the last point and from 95 to 0% in same increments. RH step lasted until reaching mass equilibrium. Soption/desorption cycle was replicated twice on each samples to provide reproducibility. Water sorption/desorption isotherms were determined from the equilibrium moisture uptake at each RH step. The equilibrium moisture uptake m_{uptake} was used to determine the equilibrium water concentration at standard temperature and pressure C (cm^3 STP cm^{-3} poly) in the polymer as follow:

$$C = \frac{m_{uptake} \times V_m}{M_w \times V_{poly}} \tag{3.3.5. 1}$$

where V_m is the molar volume of water vapor (22055 cm^3 mol^{-1} at 20 °C), M_w the water molecular weight (18 g mol^{-1}) and V_{poly} is the sample polymer volume (cm^3).

3.3.5.6 Water vapor diffusivity

Water vapor diffusivity values were estimated for each relative humidity step from kinetic gravimetric water vapor uptake experiments. Water vapor sorption data can be easily converted to a non-dimensional form *via* Equation 3.3.5. 2 useful for extracting diffusivity values:

$$\frac{m_t}{m_\infty} = \left(\frac{m_{uptake}(t)}{m_{final} - m_{initial}}\right) \tag{3.3.5. 2}$$

where m_t denotes the water uptake at time t and m_∞ denotes the water uptake after infinite time represented by equilibrium since $m_{initial}$ is the measured mass at the beginning of the sorption step and m_{final} is the measured mass at the end of the sorption step.

Analytical solutions of Equation 3.3.5. 2 can be obtained by assuming simplified sample geometry and boundary and initial conditions. If the sample tested in the DVS apparatus is an infinite plane sheet defined by $x \in \left[-\frac{L}{2}, +\frac{L}{2}\right]$ where L is the film thickness, and the initial and boundary conditions are:

$$C_{(t=0,x)} = C_0 \qquad \forall x \in \left[-\frac{L}{2}, +\frac{L}{2}\right]$$

$C_{(t,x=\pm L/2)} = C_{\infty} \qquad \forall t > 0$

the simplest analytical solution of water vapor diffusivity is described by Crank *et al.*[167]:

$$\left.\frac{m_t}{m_{\infty}}\right|_C = 1 - \sum_{n=0}^{\infty} \frac{8}{(2n+1)^2\pi^2} exp\left(-\frac{D\,(2n+1)^2\pi^2 t}{L^2}\right) \tag{3.3.5. 3}$$

where D ($m^2\ s^{-1}$) is the Fickian diffusion coefficient averaged over the concertation interval.

Equation 3.3.5. 3 applies also for monodirectional diffusion from one side, the flux being null at the other face considering that material thickness is $2L$ instead of L. In the present study the thickness considered in Equation 3.3.5 3 is $2L$ as diffusion occurs only by the upper face.

D is identified from transient data of each RH steps: therefore, one D value is obtained for each RH investigated. D was considered as the average value for full range, so, D values reported in the present work are plotted at the midpoint of the respective sorption intervals. The subscript C denotes the Crank model.

Crank model, however, doesn't estimate accurate analytical solutions when non-Fickian relaxations occur. Barens and Hopfenberg [166] proposed a model which states that both Fickian diffusion (F) and relaxation processes (R) exist independently and can be combined using linear superposition shown in Equations 3.3.5. 4 and 3.3.5. 5.

$$m_t = m_{t,F} + m_{t,R} \tag{3.3.5. 4}$$

$$\left.\frac{m_t}{m_{\infty}}\right|_{BH} = \left[\phi\left(\left.\frac{m_t}{m_{\infty}}\right|_C\right) + (1-\phi)\left(1 - exp\left(-\frac{1}{\tau_R}\right)\right)\right] \tag{3.3.5. 5}$$

In Equation 3.3.5. 4, $m_{t,F}$ represents the mass uptake ascribable to the Fickian diffusion, $m_{t,R}$ represents the mass uptake referable to non-Fickian relaxations and m_t is the total mass uptake at time t as sum of both mechanism.

In Equation 3.3.5. 5, φ is a weighting factor that ranges from 0 to 1 and specifies the relative F (φ =1) and R (φ =0) contributions, τ_R is the time constant for the non-Fickian relaxations. The subscript *BH* denotes the Barens-Hopfenberg model.

3.3.5.7 Identification parameters procedure

Parameters of the water sorption isotherm and water vapor diffusivity were identified from MATLAB® software solving a nonlinear least-squared fitting problem by *lsquonlin* function The Levenberg-Marquardt procedure was used. The *lsquonlin* MATLAB routine allows minimizing the root mean square error between experimental data $data_{exp}$ and the simulated data $data_{sim}$, as follows:

$$RMSE = \sqrt{\frac{\sum_{i=1}^{N}\left((data_{sim}(\mathrm{i}) - data_{exp}(\mathrm{i})\right)^2}{N}} \qquad (3.3.5.\ 6)$$

where N is the number of terms in the predicted or experimental vector ($data_{sim}$ or $data_{exp}$). According to Equation 3.3.5.6, the unit of the RMSE is the same as that of $data_{sim}$ or $data_{exp}$. To identify the parameters of water sorption isotherm Equations 3.3.3 and 3.3.5 were fitted onto experimental sorption curves. To identify water vapor diffusivity, Equations 3.3.4 (= Equation 3.3.5.5) and 3.3.11 (= Equation 3.3.5.3) were fitted onto experimental kinetic sorption data. The fitting of Equation 3.3.4 to $m_{exp}(t)$ provides the identification of D, φ, and τ_R at the same time. Due to the presence of three unknown parameters in Equation 3.3.5.5, caution should be exercised regarding the selection of the initial values required by the nonlinear least-squared fitting problem. To avoid any problem of local minimum, a range of different initial values of physical significance for each parameter (one at a time) was explored. The optimum is the set of values that is obtained each time with different initial values. As a starting point, to D was assigned an initial value previously identified by the Crank model (1×10^{-11} m^2 s^{-1}), to φ was assigned the value of 0.5 which is the average between the extremis 0 and 1, to τ_R an initial value corresponding to the one calculated for amorphous PET in the study of Burgess *et al.*[170] ($1 \times 10^{+4}$ s).

CHAPTER 4: CONCLUSIONS

The research work conducted was focused on the development of new bio-polymers by exploiting some of the most promising natural compounds coming from biomass.

The unique chemical structure of the selected compounds was exploited to provide peculiar properties to the final polymeric structures. Moreover, the architecture of the polymers was shaped by means of copolymerization when necessary, resulting an effective tool to improve suboptimal performances of the homopolymers.

In order to move towards a **sustainable model of development**, the synthetic pathways conducted to obtain bio-polymers and copolymers were designed as eco-friendly: solvent free, no purification step requirement and avoidance of inhibitors, suitable for an industrial upscaling. The synthesized materials were completely characterized from chemical, structural and thermal point of view. Afterwards, peculiar properties as antimicrobial activity and water barrier properties coming from their unique chemical structure were investigated in order to evaluate their suitability as for example in antimicrobial and packaging applications.

The experimental research work can be summarized in two main value chains.

Dimethyl itaconate was functionalized *via* thia-Michael addition reaction obtaining a **thermo-stable building block** that can undergo polycondensation under classical conditions of reaction to yield stable polyesters. The addition of a long lateral chain demonstrates to provide **antimicrobial activity** against *Staphylococcus aureus*. The rigidity of the homopolymer was successfully tuned by varying the diol. Moreover, we demonstrated that the architecture of the homopolymer can be modified by means of copolymerization with **dimethyl 2,5-furandicarboxylate** thus improving the **rigidity** and obtaining thermo-processable materials. Both itaconic acid and 2.5-funrandicarboxylic acid are two of the most promising building blocks coming from biomass and their combination to provide thermostable articles that have biocidal activity could be exploited for example in packaging and targeting antimicrobial applications.

Methyl vanillate was successfully copolymerized with **ω-pentadecalactone** providing **processable** random copolymers. The copolymers present a succession of aromatic and aliphatic units and, as a consequence of the chemical structure, **water vapor permeability** interposes between polyethylene and poly(ethylene terephthalate) proving that the polyesters are suitable for packaging applications.

In conclusion, with the aim to move from a petrol-based to a sustainable model of development, **interesting bio-based building blocks have been successfully exploited to**

design novel bio-polymers presenting peculiar properties creating new scenarios in polymer science. The research work has enriched the portfolio of polymers coming from renewable resources even if additional investigations are needed to realize industrial products suitable to enter the market.

REFERENCES

1. Baekeland, L. H. The synthesis, constitution, and uses of bakelite. *Ind. Eng. Chem.* **1,** 149–161 (1909).
2. PlasticsEurope. European Plastics Industry Market Data. at <https://www.plasticseurope.org/en/resources/market-data>
3. European Commission. *A European Strategy for Plastics in a Circular Economy*. (2018). at <https://eur-lex.europa.eu/legal-content/EN/TXT/PDF/?uri=CELEX:52018DC0028&from=EN>
4. Worm, B., Lotze, H. K., Jubinville, I., Wilcox, C. & Jambeck, J. Plastic as a Persistent Marine Pollutant. *Annu. Rev. Environ. Resour.* **42,** 1–26 (2017).
5. European Commission. *Closing the loop - An EU action plan for the Circular Economy*. (2015). at <https://eur-lex.europa.eu/legal-content/EN/TXT/PDF/?uri=CELEX:52015DC0614&from=EN>
6. *Directive 2019/904/EU of the European Parliament and of the Council of 5 June 2019 on the reduction of the impact of certain plastic products on the environment*. *Official Journal of the European Union* (2019).
7. Rudnik, E. *Compostable Polymer Materials 2nd Edition*. (Elsevier, 2019).
8. Hamad, K., Kaseem, M. & Deri, F. Recycling of waste from polymer materials : an overview of the recent works. *Polym. Degrad. Stab.* **98,** 2801–2812 (2013).
9. EN 13432. *Packaging - Requirements for packaging recoverable through composting and biodegradation - Test scheme and evaluation criteria for the final acceptance of packaging*. (2000).
10. European Bioplastics. What are bioplastics? (2020). at <https://www.european-bioplastics.org/bioplastics/>
11. European Bioplastics. Bioplastics market data. (2020). at <https://www.european-bioplastics.org/news/publications/>
12. Chen, G. Q. A microbial polyhydroxyalkanoates (PHA) based bio- and materials industry. *Chem. Soc. Rev.* **38,** 2434–2446 (2009).
13. Gandini, A., Silvestre, A. J. D., Neto, C. P., Sousa, A. F. & Gomes, M. The Furan Counterpart of Poly(ethylene terephtalate): An Alternative Material Based on Renewable Resources. *J. Polym. Sci. Part A Polym. Chem.* **47,** 295–298 (2008).
14. Nova Institute. Renewable carbon -bio- and CO_2- based economy. at <http://bio-based.eu/>

15. Painter, P. C. & Coleman, M. M. *Essentials of Polymer Science and Engineering*. (DEStech Publications, Inc, 2009).
16. Ralston, B. E. & Osswald, T. A. The History of Tomorrow's Materials: Protein-Based Biopolymers. *Plast. Eng.* **64,** 36–40 (2008).
17. Shen, L., Worrell, E. & Patel, M. Present and future development in plastics from biomass. *Biofuels, Bioprod. Biorefining* **4,** 25–40 (2010).
18. Klass, D. L. *Biomass for renewable energy, fuels and chemicals*. (Academic Press, 1998).
19. Organization of the Petroleum Exporting Coutries. OPEC share of word crude oil reserves. (2018). at <https://www.opec.org/opec_web/en/data_graphs/330.htm>
20. Internetional Energy Agency. Fuels and Technologies: Oil. (2018). at <https://www.iea.org/fuels-and-technologies/oil>
21. Demirbaş, A. Biomass resource facilities and biomass conversion processing for fuels and chemicals. *Energy Convers. Manag.* **42,** 1357–1378 (2001).
22. Potter, C. S. *et al.* Terrestrial ecosystem production: a process model based on global satellite and surface data. *Global Biogeochem. Cycles* **7,** 811–841 (1993).
23. Coma, M. *et al.* Organic waste as a sustainable feedstock for platform chemicals. *Faraday Discuss.* **202,** 175–195 (2017).
24. Abdul Khalil, H. P. S., Bhat, A. H. & Ireana Yusra, A. F. Green composites from sustainable cellulose nanofibrils: A review. *Carbohydr. Polym.* **87,** 963–979 (2012).
25. Sakurada, I., Nukushina, Y. & Ito, T. Experimental Determination of the Elastic Modulus of Crystalline Regions in Oriented Polymers. *J. Polym. Sci.* **57,** 651–660 (1962).
26. Miao, C. & Hamad, W. Y. Cellulose reinforced polymer composites and nanocomposites: a critical review. *Cellulose* **20,** 2221–2262 (2013).
27. Rahmat, A. R., Rahman, W. A. W. A., Sin, L. T. & Yussuf, A. A. Approaches to improve compatibility of starch filled polymer system: A review. *Mater. Sci. Eng. C* **29,** 2370–2377 (2009).
28. Bastioli, C. Properties and applications of Mater-Bi starch-based materials. *Polym. Degrad. Stab.* **59,** 263–272 (1998).
29. Jiménez, A., Fabra, M. J., Talens, P. & Chiralt, A. Edible and Biodegradable starch films: A Review. *Food Bioprocess Technol.* **5,** 2058–2076 (2012).
30. Paes, S. S., Yakimets, I. & Mitchell, J. R. Influence of gelatinization process on functional properties of cassava starch films. *Food Hydrocoll.* **22,** 788–797 (2008).

31. Zhong, Y. *et al.* Comparison of gelatinization method, starch concentration, and plasticizer on physical properties of high-amylose starch films. *J. Food Process Eng.* **41,** 1–8 (2018).
32. Stepto, R. F. T. Understanding the Processing of Thermoplastic Starch. *Macromol. Symp.* **245–246,** 571–577 (2006).
33. Liu, H., Xie, F., Yu, L., Chen, L. & Li, L. Thermal processing of starch-based polymers. *Prog. Polym. Sci.* **34,** 1348–1368 (2009).
34. Norgren, M. & Edlund, H. Lignin: Recent advances and emerging applications. *Curr. Opin. Colloid Interface Sci.* **19,** 409–416 (2014).
35. Thakur, V. K. & Thakur, M. K. Recent advances in green hydrogels from lignin: a review. *Int. J. Biol. Macromol.* **72,** 834–847 (2015).
36. Duval, A. & Lawoko, M. A review on lignin-based polymeric, micro- and nano-structured materials. *React. Funct. Polym.* **85,** 78–96 (2014).
37. Fang, W., Yang, S., Wang, X. L., Yuan, T. Q. & Sun, R. C. Manufacture and application of lignin-based carbon fibers (LCFs) and lignin-based carbon nanofibers (LCNFs). *Green Chem.* **19,** 1794–1827 (2017).
38. Wang, C., Kelley, S. S. & Venditti, R. A. Lignin-Based Thermoplastic Materials. *ChemSusChem* **9,** 770–783 (2016).
39. Rinaudo, M. Chitin and chitosan: Properties and applications. *Prog. Polym. Sci.* **31,** 603–632 (2006).
40. Khor, E. & Lim, L. Y. Implantable applications of chitin and chitosan. *Biomaterials* **24,** 2339–2349 (2003).
41. Khanna, S. & Srivastava, A. K. Recent advances in microbial polyhydroxyalkanoates. *Process Biochem.* **40,** 607–619 (2005).
42. Khosravi-Darani, K. & Bucci, D. Z. Application of Poly(hydroxyalkanoate) in Food Packaging: Improvements by Nanotechnology. *Chem. Biochem. Eng. Q.* **29,** 275–285 (2015).
43. Mendieta, C. M., Vallejos, M. E., Felissia, F. E., Chinga-Carrasco, G. & Area, M. C. Review: Bio-polyethylene from Wood Wastes. *J. Polym. Environ.* **28,** 1–16 (2020).
44. Braskem. *Annual report*. (2018). at <https://www.braskem.com.br/annualreport2018>
45. Indufor North America LLC. *Global Market Analysis and Benchmarking Study. Phase 1: Global Market Analysis*. (2018). at <https://formaine.org/home-page/resources/studies-reports/>
46. Behera, S. *et al.* Scope of algae as third generation biofuels. *Front. Bioeng. Biotechnol.*

2, 1–13 (2015).

47. Harmsen, P. F. H., Hackmann, M. M. & Bos, H. L. Green buildings blocks for bio-based plastics. *Biofuels, Bioprod. Biorefining* **8,** 306–324 (2014).
48. Yenduri, A. & Sumant, O. *Bio Based Polypropylene Market Analysis by Application (Injection, Textile, Films), by Region (North America, Europe, Asia Pacific, Rest of the World), and Segment Forecasts, 2018 - 2025*. (2017).
49. Inovyn. INOVYN launches World's first comercially available grade of bio-attributed PVC. (2019). at <https://www.inovyn.com/news/inovyn-launches-worlds-first-commercially-available-grade-of-bio-attributed-pvc/>
50. Jia, P., Xia, H., Tang, K. & Zhou, Y. Plasticizers Derived from Biomass Resources: A Short Review. *Polymers (Basel).* **10,** 1–27 (2018).
51. van der Waal, J. C. & de Jong, E. in *Producing Fuels and Fine Chemicals from Biomass Using Nanomaterials* (eds. Luque, R. & Balu, A. M.) 223–265 (CRC Press, 2013).
52. Feldman, R. M. R. *et al.* Yeast organism producing isobutanol at a high yield. US 8017375 B2. (2011).
53. Peters, M. W., Taylor, J. D., Jenni, M., Manzer, L. E. & Henton, D. E. Integrated process to selectively convert renewable isobutanol to p-xylene. US 2011/0087000 A1. (2011).
54. Cortright, R. D. & Blommel, P. G. Synthesis of liquid fuels and chemicals from oxygenated hydrocarbons. US 8053615 B2. (2011).
55. Cortright, R. D. & Dumesic, J. A. Catalyst to dehydrogenate paraffin hydrocarbons. US 5736478 A. (1998).
56. Cortright, R. D. & Dumesic, J. A. Method for catalytically reducing carboxylic acid groups to hydroxyl groups in hydroxycarboxylic acids. US 6441241 B1. (2002).
57. Dumesic, J. A., Simonetti, D. A. & Kunkes, E. L. Single-reactor process for producing liquid-phase organic compounds from biomass. US 8075642 B2. (2011).
58. Virent. *Virent BioFormPX ® Paraxylene Used for World ' s First PET Plastic Bottle Made Entirely From Plant-Based Material.* (2015). at <https://www.virent.com/news/virent-bioformpx-paraxylene-used-for-worlds-first-pet-plastic-bottle-made-entirely-from-plant-based-material/>
59. Iglesias, J. *et al.* Advances in catalytic routes for the production of carboxylic acids from biomass: a step forward for sustainable polymers. *Chem. Soc. Rev.* **49,** 5704–5771 (2020).

60. Frost, J. W. *et al.* Biobased polyesters. US 2011/0288263 A1. (2011).
61. Miller, K. K., Zhang, P., Nishizawa-Brennen, Y. & Frost, J. W. Synthesis of biobased terephthalic acid from cycloaddition of isoprene with acrylic acid. *ACS Sustain. Chem. Eng.* **2,** 2053–2056 (2014).
62. Berti, C. *et al.* Bio-based terephthalate polyesters. US 2010/0168371 A1. (2010).
63. Showa Denko Europe. Products. at <https://www.showa-denko.com/>
64. Mitsubishi chemical. Products. at <https://www.m-chemical.co.jp/en/index.html>
65. Bechthold, I., Bretz, K., Kabasci, S., Kopitzky, R. & Springer, A. Succinic Acid: A New Platform Chemical for Biobased Polymers from Renewable Resources. *Chem. Eng. Technol.* **31,** 647–654 (2008).
66. Xu, J. & Guo, B. H. Poly(butylene succinate) and its copolymers: Research, development and industrialization. *Biotechnol. J.* **5,** 1149–1163 (2010).
67. Varadarajan, S. & Miller, D. J. Catalytic upgrading of fermentation-derived organic acids. *Biotechnol. Prog.* **15,** 845–854 (1999).
68. Gigli, M., Lotti, N., Gazzano, M., Finelli, L. & Munari, A. Novel eco-friendly random copolyesters of poly(butylene succinate) containing ether-linkages. *React. Funct. Polym.* **72,** 303–310 (2012).
69. Azim, H., Dekhterman, A., Jiang, Z. & Gross, R. A. Candida antarctica Lipase B-Catalyzed Synthesis of Poly(butylene succinate): Shorter Chain Building Blocks Also Work. *Biomacromolecules* **7,** 3093–3097 (2006).
70. Sugihara, S., Toshima, K. & Matsumura, S. New strategy for enzymatic synthesis of high-molecular-weight poly(butylene succinate) via cyclic oligomers. *Macromol. Rapid Commun.* **27,** 203–207 (2006).
71. Yoo, E. S. & Im, S. S. Melting behavior of poly(butylene succinate) during heating scan by DSC. *J. Polym. Sci. Part B Polym. Phys.* **37,** 1357–1366 (1999).
72. Liu, L., Yu, J., Cheng, L. & Qu, W. Mechanical properties of poly(butylene succinate) (PBS) biocomposites reinforced with surface modified jute fibre. *Compos. Part A Appl. Sci. Manuf.* **40,** 669–674 (2009).
73. Jin, F. L., Pang, Q. Q., Zhang, T. Y. & Park, S. J. Synergistic reinforcing of poly(lactic acid)-based systems by poly(butylene succinate) and nano-calcium carbonate. *J. Ind. Eng. Chem.* **32,** 77–84 (2015).
74. Bhatia, A., Gupta, R. K., Bhattacharya, S. N. & Choi, H. J. Compatibility of biodegradable poly(lactic acid) (PLA) and poly(butylene succinate) (PBS) blens for packaging application. *Korea-Australia Rheol. J.* **19,** 125–131 (2007).

75. Sisti, L., Totaro, G. & Marchese, P. in *Biodegradable and Biobased Polymers for Environmental and Biomedical Applications* (eds. Kalia, S. & Avérous, L.) 225–285 (Scrivener Publishing LLC, 2016).

76. Narayanan, N., Roychoudhury, P. K. & Srivastava, A. L (+) lactic acid fermentation and its product polymerization. *Electron. J. Biotechnol.* **7,** 167–179 (2004).

77. John, R. P., Anisha, G. S., Nampoothiri, K. M. & Pandey, A. Direct lactic acid fermentation: Focus on simultaneous saccharification and lactic acid production. *Biotechnol. Adv.* **27,** 145–152 (2009).

78. Kulkarni, R. K., Moore, E. G., Hegyeli, A. F. & Leonard, F. Biodegradable Poly(lactic acid) Polymers. *J. Biomed. Mater. Res.* **5,** 169–181 (1971).

79. NatureWorks. About NatureWorks. at <https://www.natureworksllc.com/About-NatureWorks>

80. Garlotta, D. A Literature Review of Poly(Lactic Acid). *J. Polym. Environ.* **9,** 63–84 (2002).

81. Anderson, K. S., Schreck, K. M. & Hillmyer, M. A. Toughening Polylactide. *Polym. Rev.* **48,** 85–108 (2008).

82. Jamshidian, M., Tehrany, E. A., Imran, M., Jacquot, M. & Desobry, S. Poly-Lactic Acid: Production, Applications, Nanocomposites, and Release Studies. *Compr. Rev. Food Sci. Food Saf.* **9,** 552–571 (2010).

83. Sousa, A. F. *et al.* Biobased polyesters and other polymers from 2,5-furandicarboxylic acid: a tribute to furan excellency. *Polym. Chem.* **6,** 5961–5983 (2015).

84. Siankevich, S. *et al.* A novel platinum nanocatalyst for the oxidation of 5-Hydroxymethylfurfural into 2,5-Furandicarboxylic acid under mild conditions. *J. Catal.* **315,** 67–74 (2014).

85. Siyo, B. *et al.* Influence of support on the aerobic oxidation of HMF into FDCA over preformed Pd nanoparticle based materials. *Appl. Catal. A Gen.* **478,** 107–116 (2014).

86. Chadderdon, D. J. *et al.* Electrocatalytic oxidation of 5-hydroxymethylfurfural to 2,5-furandicarboxylic acid on supported Au and Pd bimetallic nanoparticles. *Green Chem.* **16,** 3778–3786 (2014).

87. Kang, E. S. *et al.* From Lignocellulosic Biomass to Furans via 5-Acetoxymethylfurfural as an Alternative to 5-Hydroxymethylfurfural. *ChemSusChem* **8,** 1179–1188 (2015).

88. Munoz De Diego, C., Schammel, W., Dam, M. A. & Gruter, G. J. M. Method for the preparation of 2,5-furandicarboxylic acid and esters thereof. WO 2011/043660 A3.

(2011).

89. Papageorgiou, G. Z., Papageorgiou, D. G., Terzopoulou, Z. & Bikiaris, D. N. Production of bio-based 2,5-furan dicarboxylate polyesters: Recent progress and critical aspects in their synthesis and thermal properties. *Eur. Polym. J.* **83,** 202–229 (2016).

90. Knoop, R. J. I., Vogelzang, W., van Haveren, J. & van Es, D. S. High Molecular Weight Poly(ethylene-2,5-furanoate); Critical Aspects in Synthesis and Mechanical Property Determination. *J. Polym. Sci. Part A Polym. Chem.* **51,** 4191–4199 (2013).

91. Jiang, M., Liu, Q., Zhang, Q., Ye, C. & Zhou, G. A Series of Furan-Aromatic Polyesters Synthesized via Direct Esterification Method Based on Renewable Resources. *J. Polym. Sci. Part A Polym. Chem.* **50,** 1026–1036 (2012).

92. De Jong, E., Dam, M. A., Sipos, L. & Gruter, G. J. M. in *Biobased Monomers, Polymers, and Materials* (eds. Smith, P. B. & Gross, R. A.) **1105,** 1–13 (American Chemical Society, 2012).

93. Eerhart, A. J. J. E., Patel, M. K. & Faaij, A. P. C. Fuels and plastics from lignocellulosic biomass via the furan pathway: an economic analysis. *Biofuels, Bioprod. Biorefining* **9,** 307–325 (2015).

94. Doi, Y., Mukai, K., Kasuya, K. & Yamada, K. in *Biodegradable Plastics and Polymers* (eds. Doi, Y. & Fukuda, K.) **12,** 39–51 (Elsevier B.V., 1994).

95. Lee, S. Y. Bacterial Polyhydroxyalkanoates. *Biotechnol. Bioeng.* **49,** 1–14 (1996).

96. Mergaert, J., Anderson, C., Wouters, A., Swings, J. & Kersters, K. Biodegradation of polyhydroxyalkanoates. *FEMS Microbiol. Lett.* **103,** 317–321 (1992).

97. Mergaert, J., Webb, A., Anderson, C., Wouters, A. & Swings, J. Microbial degradation of poly(3-hydroxybutyrate) and poly(3- hydroxybutyrate-co-3-hydroxyvalerate) in soils. *Appl. Environ. Microbiol.* **59,** 3233–3238 (1993).

98. Mergaert, J., Anderson, C., Wouters, A. & Swings, J. Microbial degradation of poly(3-hydroxybutyrate) and poly(3-hydroxybutyrate-co-3-hydroxyvalerate) in compost. *J. Environ. Polym. Degrad.* **2,** 177–183 (1994).

99. Burgess, S. K. *et al.* Chain Mobility, Thermal, and Mechanical Properties of Poly(ethylene furanoate) Compared to Poly(ethylene terephthalate). *Macromolecules* **47,** 1383–1391 (2014).

100. Burgess, S. K., Karvan, O., Johnson, J. R., Kriegel, R. M. & Koros, W. J. Oxygen sorption and transport in amorphous poly(ethylene furanoate). *Polymer (Guildf).* **55,** 4748–4756 (2014).

101. Burgess, S. K., Kriegel, R. M. & Koros, W. J. Carbon dioxide sorption and transport in amorphous poly(ethylene furanoate). *Macromolecules* **48,** 2184–2193 (2015).

102. Totaro, G. *et al.* Synthesis of castor oil-derived polyesters with antimicrobial activity. *Eur. Polym. J.* **56,** 174–184 (2014).

103. Werpy, T. & Peterson, G. *Top value added chemicals from biomass Volume I — Results of screening for potential candidates from sugars and synthesis gas*. *U.S. Department of Energy* **I,** (2004).

104. Holladay, J. E., White, J. F., Bozell, J. J. & Johnson, D. *Top value-added chemicals from biomass Volume II — Results of screening for potential candidates from biorefinery lignin*. *U.S. Department of Energy* **II,** (2007).

105. Gandini, A. Polymers from Renewable Resources: A Challenge for the Future of Macromolecular Materials. *Macromolecules* **41,** 9491–9504 (2008).

106. Gandini, A. & Lacerda, T. M. From monomers to polymers from renewable resources: Recent advances. *Prog. Polym. Sci.* **48,** 1–39 (2015).

107. Zia, K. M., Noreen, A., Zuber, M., Tabasum, S. & Mujahid, M. Recent developments and future prospects on bio-based polyesters derived from renewable resources: A review. *Int. J. Biol. Macromol.* **82,** 1028–1040 (2016).

108. Willke, T. & Vorlop, K. D. Biotechnological production of itaconic acid. *Appl. Microbiol. Biotechnol.* **56,** 289–295 (2001).

109. El-Imam, A. A. & Du, C. Fermentative Itaconic Acid Production. *J. Biodiversity, Bioprospecting Dev.* **1,** 1–8 (2014).

110. Okabe, M., Lies, D., Kanamasa, S. & Park, E. Y. Biotechnological production of itaconic acid and its biosynthesis in Aspergillus terreus. *Appl. Microbiol. Biotechnol.* **84,** 597–606 (2009).

111. Marvel, C. S. & Shepherd, T. H. Polymerization reactions of itaconic acid and some of its derivatives. *J. Org. Chem.* **24,** 599–605 (1959).

112. Corici, L. *et al.* Understanding potentials and restrictions of solvent-free enzymatic polycondensation of itaconic acid: an experimental and computational analysis. *Adv. Synth. Catal.* **357,** 1763–1774 (2015).

113. Barrett, D. G., Merkel, T. J., Luft, J. C. & Yousaf, M. N. One-step syntheses of photocurable polyesters based on a renewable resource. *Macromolecules* **43,** 9660–9667 (2010).

114. Brännström, S., Malmström, E. & Johansson, M. Biobased UV-curable coatings based on itaconic acid. *J. Coatings Technol. Res.* **14,** 851–861 (2017).

115. Guo, B. *et al.* Biobased poly(propylene sebacate) as shape memory polymer with tunable switching temperature for potential biomedical applications. *Biomacromolecules* **12,** 1312–1321 (2011).

116. Wei, T. *et al.* Tough bio-based elastomer nanocomposites with high performance for engineering applications. *Adv. Eng. Mater.* **14,** 112–118 (2012).

117. Dai, J. *et al.* Synthesis of bio-based unsaturated polyester resins and their application in waterborne UV-curable coatings. *Prog. Org. Coatings* **78,** 49–54 (2015).

118. Pellis, A. *et al.* Towards feasible and scalable solvent-free enzymatic polycondensations: integrating robust biocatalysts with thin film reactions. *Green Chem.* **17,** 1756–1766 (2015).

119. Winkler, M., Lacerda, T. M., Mack, F. & Meier, M. A. R. Renewable polymers from itaconic acid by polycondensation and ring-opening-metathesis polymerization. *Macromolecules* **48,** 1398–1403 (2015).

120. Okada, Y., Banno, T., Toshima, K. & Matsumura, S. Synthesis and properties of polycarboxylate-type green surfactants with S- or N-linkages. *J. Oleo Sci.* **58,** 519–528 (2009).

121. Otera, J. Transesterification. *Chem. Rev.* **93,** 1449–1470 (1993).

122. Burfield, D. R. & Lim, K.-L. Differential scanning calorimetry analysis of natural rubber and related polyisoprenes. Measurement of the glass transition temperature. *Macromolecules* **16,** 1170–1175 (1983).

123. Zhang, M., Tu, Y., Zhou, Z. & Wu, G. Balancing the transesterification reactivity of isosorbide with diphenyl carbonate: preferential activation of exo-OH. *Polym. Chem.* **11,** 5512–5525 (2020).

124. Celli, A., Marchese, P., Sullalti, S., Berti, C. & Barbiroli, G. Eco-friendly poly(butylene 1,4-cyclohexanedicarboxylate): Relationships between stereochemistry and crystallization behavior. *Macromol. Chem. Phys.* **212,** 1524–1534 (2011).

125. Dussenne, C. *et al.* Synthesis of isosorbide: an overview of challenging reactions. *Green Chem.* **19,** 5332–5344 (2017).

126. Vannini, M., Marchese, P., Celli, A. & Lorenzetti, C. Fully biobased poly(propylene 2,5-furandicarboxylate) for packaging applications: excellent barrier properties as a function of crystallinity. *Green Chem.* **17,** 4162–4166 (2015).

127. NoAW. at <https://noaw2020.eu/>

128. AgriMax. at <https://agromax.iris.cat/>

129. Tilay, A., Bule, M., Kishenkumar, J. & Annapure, U. Preparation of ferulic acid from

agricultural wastes: its improved extraction and purification. *J. Agric. Food Chem.* **56,** 7644–7648 (2008).

130. Mussatto, S. I., Dragone, G. & Roberto, I. C. Ferulic and p-coumaric acids extraction by alkaline hydrolysis of brewer’s spent grain. *Ind. Crops Prod.* **25,** 231–237 (2007).
131. Topakas, E., Kalogeris, E., Kekos, D., Macris, B. J. & Christakopoulos, P. Bioconversion of ferulic acid into vanillic acid by the thermophilic fungus Sporotrichum thermophile. *Leb. -wiss. und-Technologie* **36,** 561–565 (2003).
132. Barghini, P., Montebove, F., Ruzzi, M. & Schiesser, A. Optimal conditions for bioconversion of ferulic acid into vanillic acid by Pseudomonas fluorescens BF13 cells. *Appl. Microbiol. Biotechnol.* **49,** 309–314 (1998).
133. Ciriminna, R. *et al.* Vanillin: The Case for Greener Production Driven by Sustainability Megatrend. *ChemistryOpen* **8,** 660–667 (2019).
134. Gioia, C. *et al.* Advances in the synthesis of bio-based aromatic polyesters: novel copolymers derived from vanillic acid and ϵ-caprolactone. *Polym. Chem.* **7,** 5396–5406 (2016).
135. Gioia, C. *et al.* Biobased vanillic acid and ricinoleic acid: building blocks for fully renewable copolyesters. *J. Renew. Mater.* **6,** 126–135 (2018).
136. Lotti, N., Colonna, M., Fiorini, M., Finelli, L. & Berti, C. Poly(ethylene terephthalate), modified with bisphenol S units, with increased glass transition temperature. *J. Appl. Polym. Sci.* **128,** 416–423 (2013).
137. Köster, E., Jellinek, J., Verhelst, N., Mojet, J. & Linschoten, M. Odorants related to human body odor. *J. Soc. Cosmet. Chem.* **37,** 409–428 (1986).
138. Liu, J. *et al.* A New Family of Rigid Dienone Musks Challenges the Perceptive Range of the Human Olfactory Receptor OR5AN1. *Synlett* **31,** 972–976 (2020).
139. van der Meulen, I. *et al.* Catalytic ring-opening polymerization of renewable macrolactones to high molecular weight polyethylene-like polymers. *Macromolecules* **44,** 4301–4305 (2011).
140. van der Meulen, I. *et al.* Copolymers from unsaturated macrolactones: toward the design of cross-linked biodegradable polyesters. *Biomacromolecules* **12,** 837–843 (2011).
141. Roesle, P. *et al.* Mechanistic features of isomerizing alkoxycarbonylation of methyl oleate. *J. Am. Chem. Soc.* **134,** 17696–17703 (2012).
142. Schrewe, M., Magnusson, A. O., Willrodt, C., Bühler, B. & Schmid, A. Kinetic analysis of terminal and unactivated C-H bond oxyfunctionalization in fatty acid

methyl esters by monooxygenase-based whole-cell biocatalysis. *Adv. Synth. Catal.* **353,** 3485–3495 (2011).

143. Mialon, L., Vanderhenst, R., Pemba, A. G. & Miller, S. A. Polyalkylenehydroxybenzoates (PAHBs): Biorenewable aromatic/aliphatic polyesters from lignin. *Macromol. Rapid Commun.* **32,** 1386–1392 (2011).

144. Lange, W. & Kordsachia, O. Darstellung und Eigenschaften von aus Vanillin und Syringaaldehyd erhältlichen Polyestern. *Holz als Roh- und Werkst.* **39,** 107–112 (1981).

145. Focarete, M. L., Scandola, M., Kumar, A. & Gross, R. A. Physical characterization of poly(ω-pentadecalactone) synthesized by lipase-catalyzed ring-opening polymerization. *J. Polym. Sci. Part B Polym. Phys.* **39,** 1721–1729 (2001).

146. De Geus, M. *et al.* Performance polymers from renewable monomers: high molecular weight poly(pentadecalactone) for fiber applications. *Polym. Chem.* **1,** 525–533 (2010).

147. Nguyen, H. T. H., Short, G. N., Qi, P. & Miller, S. A. Copolymerization of lactones and bioaromatics: via concurrent ring-opening polymerization/polycondensation. *Green Chem.* **19,** 1877–1888 (2017).

148. Girija, B. G., Sailaja, R. R. N. & Madras, G. Thermal degradation and mechanical properties of PET blends. *Polym. Degrad. Stab.* **90,** 147–153 (2005).

149. Lecomte, H. A. & Liggat, J. J. Degradation mechanism of diethylene glycol units in a terephthalate polymer. *Polym. Degrad. Stab.* **91,** 681–689 (2006).

150. Wang, X., Li, X. & Yan, D. Thermal decomposition kinetics of poly(trimethylene terephthalate). *Polym. Degrad. Stab.* **69,** 361–372 (2000).

151. Sivalingam, G. & Madras, G. Thermal degradation of binary physical mixtures and copolymers of poly(ε-caprolactone), poly(D, L-lactide), poly(glycolide). *Polym. Degrad. Stab.* **84,** 393–398 (2004).

152. Statheropoulos, M., Kyriakou, S. & Tzamtzis, N. Performance evaluation of a TG/MS system. *Thermochim. Acta* **322,** 167–173 (1998).

153. Aggarwal, S. L. & Sweeting, O. J. Polyethylene: preparation, structure, and properties. *Chem. Rev.* **57,** 665–742 (1957).

154. Gazzano, M., Malta, V., Focarete, M. L., Scandola, M. & Gross, R. A. Crystal Structure of Poly(ω-pentadecalactone). *J. Polym. Sci. Part B Polym. Phys.* **41,** 1009–1013 (2003).

155. Hoffman, J. D. & Weeks, J. J. Melting process and the equilibrium melting temperature of polychlorotrifluoroethylene. *J. Res. Natl. Bur. Stand. Phys. Chem.* **66A,** 13–28

(1962).

156. Cai, J., Hsiao, B. S. & Gross, R. A. Polypentadecalactone prepared by lipase catalysis : crystallization kinetics and morphology. *Polym. Int.* **58,** 944–953 (2009).

157. Zamboulis, A. *et al.* Synthesis , Thermal Properties and Decomposition Mechanism of Poly(Ethylene Vanillate) Polyester. *Polymers (Basel).* **11,** 1–27 (2019).

158. Baur, H. Einfluβ der sequenzlängenverteilung auf das schmelz-ende von copolymeren. *Makromol. Chemie* **98,** 297–301 (1966).

159. Chisholm, B. J. & Zimmer, J. C. Isothermal crystallization kinetics of commercially important polyalkylene terephthalates. *J. Appl. Polym. Sci.* **76,** 1296–1307 (2000).

160. Jabarin, S. A. & Lofgren, E. A. Effects of water absorption on physical properties and degree of molecular orientation of poly(ethylene terephthalate). *Polym. Eng. Sci.* **26,** 620–625 (1986).

161. Bastioli, C., Guanella, I. & Romano, G. Effects of water sorption on the physical properties of PET, PBT, and their long fibers composites. *Polym. Compos.* **11,** 1–9 (1990).

162. Popineau, S. & Shanahan, M. E. R. Simple model to estimate adhesion of structural bonding during humid ageing. *Int. J. Adhes. Adhes.* **26,** 363–370 (2006).

163. Immergut, E. H. & Mark, H. F. in *Plasticization and Plasticizer Processes* **48,** 1–26 (American Chemical Society, 1965).

164. Dubelley, F. *et al.* Water Vapor Sorption Properties of Polyethylene Terephthalate over a Wide Range of Humidity and Temperature. *J. Phys. Chem. B* **121,** 1953–1962 (2017).

165. Feng, H. Modeling of vapor sorption in glassy polymers using a new dual mode sorption model based on multilayer sorption theory. *Polymer (Guildf).* **48,** 2988–3002 (2007).

166. Barens, A. R. & Hopfenberg, H. B. Diffusion and relaxation in glassy polymers powders: 2. Separation of diffusion and relaxation parameters. *Polymer (Guildf).* **19,** 489–496 (1978).

167. Crank, J. *The Mathematics of Diffusion, 2nd edition*. *Oxford Science Publications* (Oxford University press, 1975).

168. Torres, N., Robin, J. J. & Boutevin, B. Study of thermal and mechanical properties of virgin and recycled poly(ethylene terephthalate) before and after injection molding. *Eur. Polym. J.* **36,** 2075–2080 (2000).

169. Klung, H. P. & Alexander, L. E. *X-ray diffraction procedures: for polycrystalline and*

amorphous materials, 2nd edition. (J. Wiley and Sons, 1974).

170. Burgess, S. K. *et al.* Water sorption in poly(ethylene furanoate) compared to poly(ethylene terephthalate). Part 2: Kinetic sorption. *Polymer (Guildf).* **55,** 6870–6882 (2014).
171. Semenova, S. I., Ohya, H. & Smirnov, S. I. Physical transitions in polymers plasticized by interacting penetrant. *J. Memb. Sci.* **136,** 1–11 (1997).
172. Kamiya, Y., Mizoguchi, K. & Naito, Y. Plasticization of Poly(ethyl Methacrylate) by Dissolved Argon. *J. Polym. Sci. Part B Polym. Phys.* **30,** 1183 (1992).
173. Koros, W. J. & Paul, D. R. CO_2 Sorption in Poly(ethylene Terephthalate) above and below the Glass Transition. *J. Polym. Sci. Polym. Phisics Ed.* **16,** 1947–1963 (1978).
174. Barbari, T. A., Koros, W. J. & Paul, D. R. Gas Sorption in Polymers Based on Bisphenol-A. *J. Polym. Sci. Part B Polym. Phys.* **26,** 729–744 (1988).
175. Koros, W. J., Chan, A. H. & Paul, D. R. Sorption and transport of various gases in poly-carbonate. *J. Memb. Sci.* **2,** 165–190 (1977).
176. Guo, J. & Barbari, T. A. Unified dual mode description of small molecule sorption and desorption kinetics in a glassy polymer. *Macromolecules* **42,** 5700–5708 (2009).
177. Burgess, S. K. *et al.* Water sorption in poly(ethylene furanoate) compared to poly(ethylene terephthalate). Part 1: Equilibrium sorption. *Polymer (Guildf).* **55,** 6861–6869 (2014).
178. Righetti, M. C., Laus, M. & Di Lorenzo, M. L. Temperature dependence of the rigid amorphous fraction in poly(ethylene terephthalate). *Eur. Polym. J.* **58,** 60–68 (2014).
179. Lin, J., Shenogin, S. & Nazarenko, S. Oxygen solubility and specific volume of rigid amorphous fraction in semicrystalline poly(ethylene terephthalate). *Polymer (Guildf).* **43,** 4733–4743 (2002).
180. Barens, A. R. Effects of sample history, time, and temperature on the sorption of monomer vapor by PVC. *J. Macromol. Sci. Part B Phys.* **14,** 483–498 (1977).
181. Vieth, W., Douglas, A. S. & Block, R. Membrane-Water Structural Interactions in Reverse Osmosis Transport. *J. Macromol. Sci. Part B Phys.* **3,** 737–749 (1969).
182. Langmuir, I. The adsoprtion of gases on plane surfaces of glass, mica and platinum. *Joirnal Am. Chem. Soc.* **40,** 1361–1403 (1918).
183. Favre, E., Nguyen, Q. T., Clément, R. & Néel, J. The engaged species induced clustering (ENSIC) model: a unified mechanistic approach of sorption phenomena in polymers. *J. Memb. Sci.* **117,** 227–236 (1996).
184. Nguyen, Q. T., Favre, E., Ping, Z. H. & Néel, J. Clustering of solvents in membranes

and its influence on membrane transport properties. *J. Memb. Sci.* **113,** 137–150 (1996).

185. Langevin, D., Grenet, J. & Saiter, J. M. Moisture sorption in PET influence on the thermokinetic parameters. *Eur. Polym. J.* **30,** 339–345 (1994).

186. Yasuda, H. & Stannett, V. Permeation, solution, and diffusion of water in some high polymers. *J. Polym. Sci.* **57,** 907–923 (1962).

187. Oliveira, N. S. *et al.* Carbon dioxide, ethylene and water vapor sorption in poly(lactic acid). *Fluid Phase Equilib.* **250,** 116–124 (2006).

188. Tang, M. C., Agarwal, S., Alsewailem, F. D., Choi, H. J. & Gupta, R. K. A model for water vapor permeability reduction in poly(lactic acid) and nanoclay nanocomposites. *J. Appl. Polym. Sci.* **135,** 1–12 (2018).

189. Ulutan, S. & Balköse, D. Diffusivity, solubility and permeability of water vapor in flexible PVC/silica composite membranes. *J. Memb. Sci.* **115,** 217–224 (1996).

190. Hauser, P. M. & McLaren, A. D. Permeation through and Sorption of Water Vapor by High Polymers. *Ind. Eng. Chem.* **40,** 112–117 (1948).

191. Auras, R. A., Singh, S. P. & Singh, J. J. Evaluation of orieneted poly(lactide) polymers vs. existing PET and oriented PS for fresh food service containers. *Packag. Technol. Sci.* **18,** 207–216 (2005).

192. Marais, S. *et al.* Effect of a low-pressure plasma treatment on water vapor diffusivity and permeability of poly(ethylene-co-vinyl alcohol) and polyethylene films. *Surf. Coatings Technol.* **201,** 868–879 (2006).